2017

Shape Memory Behavior of Dense and Porous NiTi Alloys Fabricated by Selective Laser Melting

Soheil Saedi
University of Kentucky, soheil.saedi@uky.edu
Author ORCID Identifier:
http://orcid.org/0000-0001-8665-5259
Digital Object Identifier: https://doi.org/10.13023/ETD.2017.173

STUDENT AGREEMENT:

I represent that my thesis or dissertation and abstract are my original work. Proper attribution has been given to all outside sources. I understand that I am solely responsible for obtaining any needed copyright permissions. I have obtained needed written permission statement(s) from the owner(s) of each third-party copyrighted matter to be included in my work, allowing electronic distribution (if such use is not permitted by the fair use doctrine) which will be submitted to UKnowledge as Additional File.

I hereby grant to The University of Kentucky and its agents the irrevocable, non-exclusive, and royalty-free license to archive and make accessible my work in whole or in part in all forms of media, now or hereafter known. I agree that the document mentioned above may be made available immediately for worldwide access unless an embargo applies.

I retain all other ownership rights to the copyright of my work. I also retain the right to use in future works (such as articles or books) all or part of my work. I understand that I am free to register the copyright to my work.

REVIEW, APPROVAL AND ACCEPTANCE

The document mentioned above has been reviewed and accepted by the student's advisor, on behalf of the advisory committee, and by the Director of Graduate Studies (DGS), on behalf of the program; we verify that this is the final, approved version of the student's thesis including all changes required by the advisory committee. The undersigned agree to abide by the statements above.

Soheil Saedi, Student

Dr. Haluk E. Karaca, Major Professor

Dr. Haluk E. Karaca, Director of Graduate Studies

SHAPE MEMORY BEHAVIOR OF DENSE AND POROUS NITI ALLOYS FABRICATED BY SELECTIVE LASER MELTING

DISSERTATION

A dissertation submitted in partial fulfillment of the
requirements for the degree of Doctor of Philosophy in the
College of Engineering
at the University of Kentucky

By

Soheil Saedi

Lexington, Kentucky

Director: Dr. Haluk E. Karaca, Professor of Mechanical Engineering

Lexington, Kentucky

2017

ABSTRACT OF THE DISSERTATION

SHAPE MEMORY BEHAVIOR OF DENSE AND POROUS NITI ALLOYS FABRICATED BY SELECTIVE LASER MELTING

Selective Laser Melting (SLM) of Additive Manufacturing is an attractive fabrication method that employs CAD data to selectively melt the metal powder layer by layer via a laser beam and produce a 3D part. This method not only opens a new window in overcoming traditional NiTi fabrication problems but also for producing porous or complex shaped structures. The combination of SLM fabrication advantages with the unique properties of NiTi alloys, such as shape memory effect, superelasticity, high ductility, work output, corrosion, biocompatibility, etc. makes SLM NiTi alloys extremely promising for numerous applications.

The SLM process parameters such as laser power, scanning speed, spacing, and strategy used during the fabrication are determinant factors in composition, microstructural features and functional properties of the SLM NiTi alloy. Therefore, a comprehensive and systematic study has been conducted over $Ni_{50.8}$ $Ti_{49.2}$ (at%) alloy to understand the influence of each parameter individually. It was found that a sharp [001] texture is formed as a result of SLM fabrication which leads to improvements in the superelastic response of the alloy. It was perceived that transformation temperatures, microstructure, hardness, the intensity of formed texture and the correlated thermo-mechanical response are changed substantially with alteration of each parameter. The provided knowledge will allow choosing optimized parameters for tailoring the functional features of SLM fabricated NiTi alloys. Without going through any heat treatments, 5.77% superelasticity with more than 95% recovery ratio was obtained in as-fabricated condition only with the selection of right process parameters.

Additionally, thermal treatments can be utilized to form precipitates in Ni-rich SLM NiTi alloys fabricated by low energy density. Precipitation could significantly alter the matrix composition, transformation temperatures and strain, critical stress for transformation, and shape memory response of the alloy. Therefore, a systematic aging study has been performed to reveal the effects of aging time and temperature. It was found

that although SLM fabricated samples show lower strength than the initial ingot, heat treatments can be employed to make significant improvements in shape memory response of SLM NiTi. Up to 5.5% superelastic response and perfect shape memory effect at stress levels up to 500 MPa was observed in solutionized Ni-rich SLM NiTi after 18h aging at 350ºC. For practical application, transformation temperatures were even adjusted without solution annealing and superelastic response of 5.5% was achieved at room temperature for 600C-1.5hr aged Ni-rich SLM NiTi

The effect of porosity on strength and cyclic response of porous SLM $Ni_{50.1}$ $Ti_{49.9}$ (at%) were investigated for potential bone implant applications. It is shown that mechanical properties of samples such as elastic modulus, yield strength, and ductility of samples are highly porosity level and pore structure dependent. It is shown that it is feasible to decrease Young's modulus of SLM NiTi up to 86% by adding porosity to reduce the mismatch with that of a bone and still retain the shape memory response of SLM fabricated NiTi. The shape memory effect, as well as superelastic response of porous SLM $Ni_{50.8}Ti_{49.2,}$ were also investigated at body temperature. 32 and 45% porous samples with similar behaviors, recovered 3.5% of 4% deformation at first cycle. The stabilized superelastic response was obtained after clicking experiments.

KEYWORDS: Additive Manufacturing, Shape Memory Alloys, Mechanical Characterization, Porous Nitinol, Superelasticity.

Soheil Saedi

Student's Signature

04.13.2017

Date 04.13.2017

SHAPE MEMORY BEHAVIOR OF DENSE AND POROUS NITI ALLOYS FABRICATED BY SELECTIVE LASER MELTING

By

Soheil Saedi

Haluk E. Karaca

Director of Dissertation

Haluk E. Karaca

Director of Graduate Studies

07.13.2017

Dedicated

To

My Beloved

Parents

Acknowledgment

First and foremost, I would like to express my special appreciation and thanks to my advisor Prof. Haluk Karaca, who has been a tremendous mentor for me. I would like to thank him for encouraging me and for allowing me to grow as a researcher. His patience and endless support have been invaluable throughout this time. This work could not have been made without his precious guidance.

I would like to thank my committee members Dr. Y.T Cheng, Dr. Christiane Trinkle, Dr. Y. Charles Lu, and Dr. Babak Bazrgari for their help. I would like to express my gratitude to our collaborator at the University of Toledo, Prof. M. Elahinia for his valuable suggestions and support. Also, I should mention his research group in Dynamic and smart systems lab of the University of Toledo for samples fabrications.

I also would like to thank Dr. X. Ren's form Aluminum Center of University of Kentucky (SECAT) for all his help to conduct XRD experiments.

Special thanks to my former and current lab-mates Mohammad Souri, Ali Sadi Turabi, Sayed Mohammad and Ehsan Saghaian, Peizhen Li, Sesha Spandana Pulla, Guher Pelin Toker, and Ethan Vance. I also appreciate the generous help of technicians of the mechanical engineering department.

Words are not enough to express how grateful I am to my amazing family, particularly my parents, brothers Siamak and Sepehr Saedi, and also Reza Kazemi for their love, support, and constant encouragement, I have gotten over the years.

Table of Contents

List of Tables

List of Figures

1 Chapter One: Introduction

1.1 History of shape memory alloys

Shape memory alloys (SMAs) are an important class of smart materials with a wide range of applications. According to Otsuka and Wayman [1], A. Ölander discovered the pseudoelastic behavior of the Au-Cd alloy in 1932. Later in 1938, formation and disappearance of martensite phase by a change in the temperature of a Cu-Zn alloy were observed by Greninger & Mooradian [2]. About a decade later, Kurdjumov & Khandros [3] and Chang & Read [4] reported that basic phenomenon of the memory effect is governed by the thermoelastic behavior of the martensitic phase transformation. In the early 1960s, Buehler and his co-workers at the U.S. Naval Ordnance Laboratory discovered the shape memory effect in an equiatomic NiTi, which can be considered as a breakthrough in the field of shape memory materials (Buehler et al. 1967). The alloy was named as Nitinol after the laboratory in which it was discovered (Nickel-Titanium Naval Ordnance Laboratory). NiTi alloy had by far the most superior properties in comparison to other SMAs including Cu-based SMAs (in particular CuZnAl), NiAl and FeMnSi. After its discovery, many studies were carried out to elucidate the behavior and remarkable properties of SMA. This also promoted several investigations related to their applications in different potential fields such as aerospace, military, automotive, industrial and biomedical. The use of NiTi for medical applications was first reported in the 1970s (Cutright et al. 1973, Iwabuchi et al. 1975, Castleman et al. 1976, Simon et al. 1977). It was in the mid-1990s that the first widespread commercial stent applications made their

breakthrough in medicine. Nowadays, NiTi SMAs are among the largest commercial in the field of bioengineering and medical applications.

1.2 Brief background on SMAs

Shape memory alloys are a unique class of metal alloys that are capable of converting thermal energy into mechanical work. After a mechanical deformation, SMAs can remember their original shape when they are heated to a certain temperature. Or they can recover a large amount of strain if they deform in a certain temperature range. SMAs in fact, undergo a solid to solid diffusionless phase transformation and as consequences can produce very high recoverable shape changes [1]. The phase transformation involves the ordered motion of the atoms in their crystal structure over extremely short distances in a way that the structure transforms from one lattice type to another. These two different phases are called "austenite", the high-temperature phase, and "martensite" which is the low-temperature phase. Indeed, the unique properties of the SMAs rely on the transformation between these phases which is induced either thermally or mechanically. Based on this transformation, two main mechanisms of SMAs namely Shape Memory Effect (SME) and Superelasticity (SE) will be discussed in the following sections.

1.2.1 Thermodynamics of Martensitic Transformations in SMAs

Martensitic transformation is a solid-state transformation and an example of a displacive (diffusionless shear transformation) transition, in which there is the cooperative motion of a relatively large number of atoms, each being displaced by only a small distance and atoms move in an organized manner relative to their neighbors. The homogeneous shearing of the parent phase creates a new crystal structure without any compositional change (no diffusion).

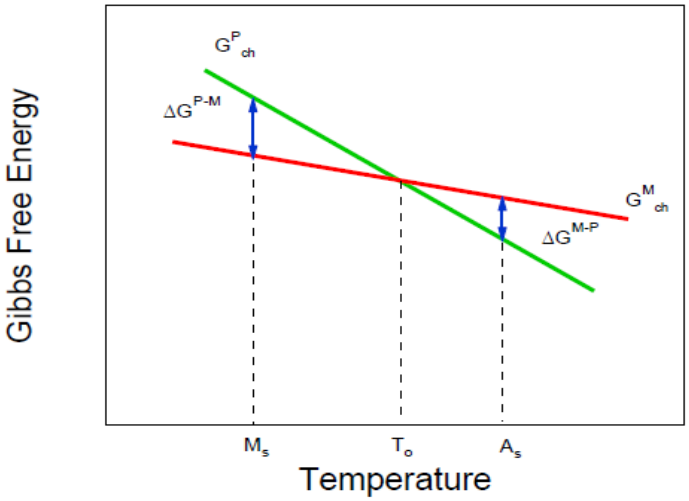

Figure 1-1 Schematics of free-energy curves of martensite and austenite during phase transformation

The chemical free energies of transforming phases are assumed to be decreasing linearly with temperature as shown in Figure 1-1. The transforming phases have the same free energy and are in equilibrium at the intersection of the lines. The temperature at which this occurs is the equilibrium temperature (T_0). For example, in SMAs, two different free energy curves represent the austenite and martensite phases. Below T_0, the martensite phase has lower free energy and therefore it is favored thermodynamically. Above T_0, austenite has lower free energy and therefore it is more stable. G^{P}_{ch} and G^{M}_{ch} are the chemical energies for austenite and martensite, respectively, while M_s is martensite start temperature and A_s is austenite start temperature.

ΔG_{ch}^{p-m} is the chemical driving force for phase transformation from parent phase (austenite) to martensite and ΔG_{ch}^{m-p} is vice versa. Parent phase transforms to martensite and martensite transforms to parent phase when there is a sufficient driving force in the system. When the G_{ch}^{M} and G_{ch}^{A} are equal to each other, no transformation is expected since

there is no difference (driving force) between the chemical energies of transforming phases. The general thermodynamical equilibrium equation for the forward transformation can be written as [5].

$$\Delta G_{total}^{p-m} = \Delta G_{ch}^{p-m} + \Delta G_{nc}^{p-m} = \Delta G_{ch}^{p-m} + \Delta G_{el}^{p-m} + \Delta G_{irr}^{p-m} \qquad 1\text{-}1$$

where ΔG_{total}^{p-m} is the total Gibbs free energy difference for the martensitic transformation, ΔG_{ch}^{p-m} is the change in chemical energy, ΔG_{nc}^{p-m} is the change in non-chemical energy. ΔG_{nc}^{p-m} can be expressed as a combination of ΔG_{el}^{p-m}, the change in elastic energy, and ΔG_{irr}^{p-m}, the irreversible energy, during the phase transformation from austenite to martensite [6]. The term ΔG_{total}^{p-m} should be zero in order to initiate the martensitic transformation. At T_0, since there is no driving force to trigger the martensitic transformation, an additional energy should be supplied (by cooling or heating) to initiate the transformation. Cooling below T_0 is necessary for parent phase to martensite transformation and heating beyond T_0 is required for martensite to parent phase transformation assuming negligible elastic energy storage. T_0 can be estimated by using the transformation temperature;

$$T_0 = \frac{1}{2}(M_s + A_s) \qquad \text{or} \qquad T_0 = \frac{1}{2}(M_f + A_f) \qquad 1\text{-}2$$

ΔG_{el}^{p-m} is the stored elastic energy during the forward transformation and it is released completely upon back transformation from martensite to austenite. Hence, the elastic energy storage is a mechanically reversible process[5]. The amount of the stored elastic energy should be equal to the released energy upon back transformation if there is

no plastic relaxation due to dislocation generation/plastic deformation after a full transformation cycle [7, 8].

The irreversible energy ΔG_{irr}^{p-m} can be assumed to stem from two main mechanisms: i) plastic relaxation energy due to dislocations and defects generation and ii) the friction energy during phase transformation due to the movement of phase transformation front, the interaction of martensite variants and internal twins. Both of the abovementioned mechanisms result in the dissipation of energy and consequently, hysteresis in SMAs [9].

1.2.2 Thermal Induced Martensitic Transformation

There are four important temperature points associated with Martensite and Austenite phases. The martensite start (M_s) temperature is one at which the martensite phase starts to form when cooling down from austenite phase and martensite finish (M_f) temperature is that at which the transformation from austenite to martensite finishes upon cooling. Similarly, upon heating when the austenite start temperature (A_s) is the one at which austenite starts to form from martensite and austenite finish (A_f) temperature is the one at which the transformation from martensite to austenite finishes upon heating.

These Transformation Temperatures (TTs) are some of the most important shape memory properties. In SMAs, the martensite to austenite transformation (backward transformation) is an endothermic reaction (heat absorbing), while the austenite to martensite transformation (forward transformation) is an exothermic reaction (heat emitting) [10]. Since the transformations occur without any external stress applied, they are also called zero-stress or stress-free transformation temperatures. The Differential Scanning Calorimeter (DSC) is the most well-known equipment to determine the latent

heat, enthalpy and transformation temperatures [11]. The basic principle behind the operation of the DSC is the measurement of the rate at which heat energy is supplied to the specimen in comparison to a reference material to maintain a constant temperature rate [12].

Figure 1-2 illustrates a typical DSC response. On the calorimetric graph, phase transformations are depicted as peaks and the areas under those peaks indicate the energies of transformations. Using these peaks, the critical transition temperatures can be determined using the tangent method. The enthalpy change (ΔH) of the phase transition can be found by integrating the area between to selected temperatures.

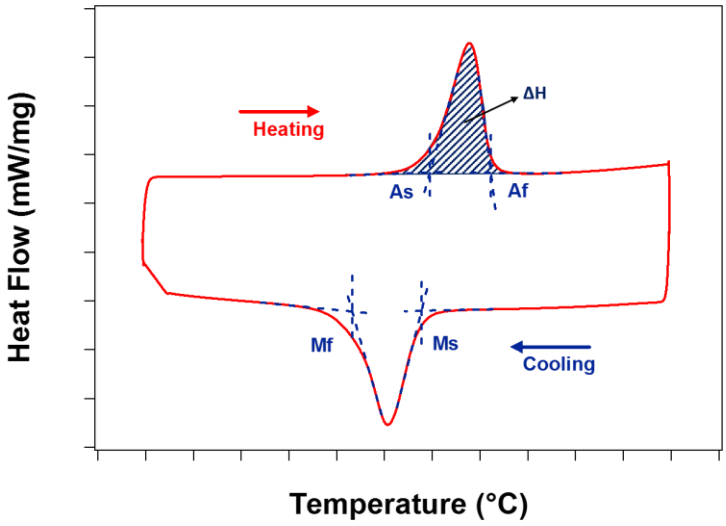

Figure 1-2 Typical DSC response

The thermally induced martensitic transformation is also feasible when a SMA component is under stress. If the stress is isothermally applied in austenitic phase and then the material is cooled, the phase transformation will result in detwinned martensite and a microscopic shape change will be observed. Complete shape recovery can be achieved by heating the material to a temperature well above the A_f. It should be noted that if the applied

stress was enough to trigger the plastic deformation in the material the full recovery may not be obtained. The TTs are also strongly applied stress dependent and they shift to a higher temperature with applied stress.

Figure 1-3 illustrates the thermal cycling under stress schematically. The total strain, ε_{total}, is determined by measuring the distance between the cooling and heating portions at M_s and TTs were determined by the tangent method. Thermal hysteresis, ΔT, was calculated as a temperature difference at the middle point of total cooling and heating curves. Irrecoverable strain, ε_{ir}, is the amount deformation that is not recovering at the end of the thermal cycle and it is the key parameter to determine the dimensional stability of the material for actuation application. In some cases, it is possible to train the SMA component by thermal cycling under stress to show a two-way effect under no applied stress in which they remember two shapes, one below and one above the transformation temperatures (TWSME).

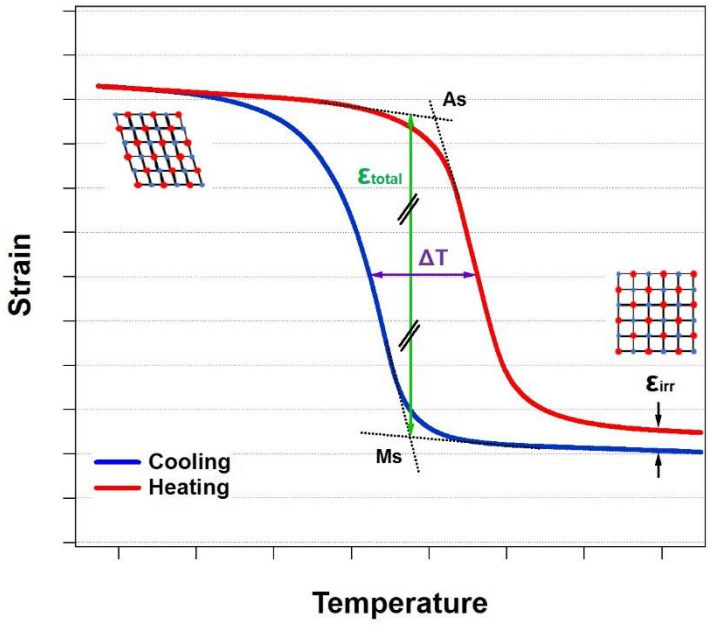

Figure 1-3 Schematic of thermal cycling under stress

1.2.3 Shape Memory Effect (SME)

Figure 1-4 is a schematic of SME. Martensite re-orientation is stress induced and the corresponding recoverable strain is associated with the conversion between the martensite variants. If external stress is applied to a SMA specimen that consists of self-accommodated martensite, it is possible to reorient and detwin the martensite variants which results in a macroscopic shape change. After the load is released, the new configuration is retained. With subsequent heating to a temperature above A_f, reverse phase transformation can be observed (from detwinned martensite to austenite) and leads to shape recovery. This is called shape memory effect (SME). It should be mentioned, that the remaining strain is not fully recovered all the time by heating up above Af. When the stress is sufficient to introduce plastic deformation and irrecoverable strain (ε_{ir}) would present after the heating cycle. The total recoverable strain is the combination of elastic (ε_{el}) and shape memory effect (ε_{sme}) strains. Cooling back to a temperature below M_f leads to the formation of twinned martensite again.

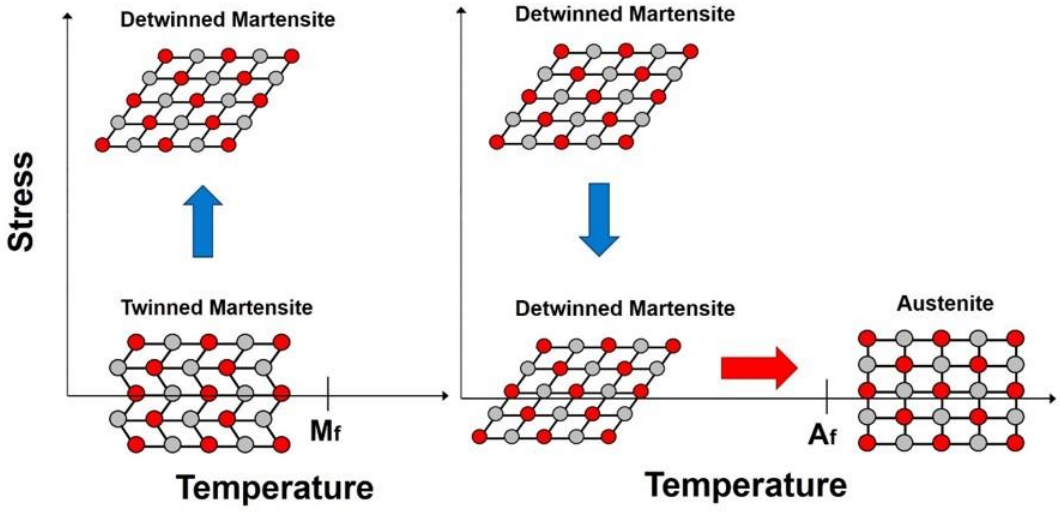

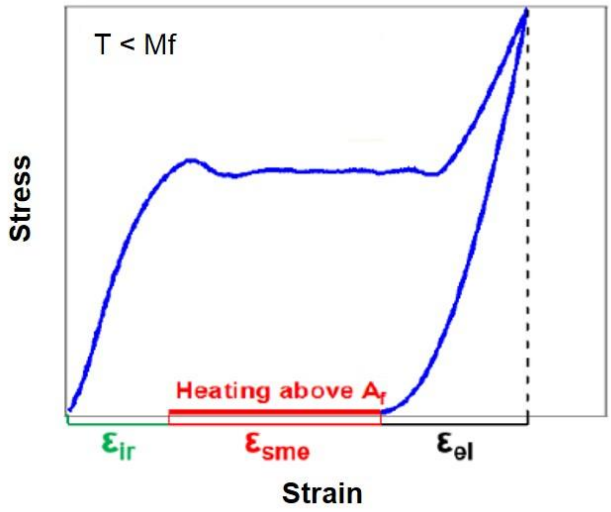

Figure 1-4 Schematic of shape memory effect of SMAs

1.2.4 Superelasticity (SE)

Superelasticity or Pseudoelasticity is a phenomenon which takes place at a temperature higher than A_f, as a result of stress-induced martensitic transformation during loading and subsequent reverse transformation upon unload. Figure 1-5 depicts superelasticity behavior of SMAs. The stress-induced austenite to martensite transformation occurs where a plateau is observed at this stage. Further, loading results in elastic deformation of martensite and detwinning of martensite. The slope of this transformation depends on the number of CVPs (correspondent variant pairs) activated for the single crystal or the texture of the material for polycrystals [13]. A CVP, correspondent variant pair, is a formal term for two twin related martensite variants. The effects of orientation in single crystals or texture in polycrystalline NiTi SMA on the recoverable strain, critical stress, etc will be discussed thoroughly in section 1.3.3. With unloading at this point, shape recovery starts with elastic deformation recovery of the martensite, followed by the martensite to austenite transformation and elastic deformation recovery of

austenite. If there is no plastic deformation, the fully reversible shape recovery will be expected. Further loading after phase transformation could result in exceeding the critical stress for slip deformation where another plateau-like behavior can be observed. Upon unloading after this stage, a full recovery is not obtained due to plastic deformation. This plastic strain is due to the generation and propagation of dislocations and results in martensite stabilization. Young moduli of austenite (E_A) and martensite (E_M), critical stresses of forward ($\sigma_{cr,ft}$) and back ($\sigma_{cr,bt}$) transformations, critical stress for plastic deformation ($\sigma_{cr,pd}$), mechanical hysteresis (Δ_σ), elastic strain (ε_{el}), superelastic strain (ε_{SE}) and irrecoverable strain (ε_{irr}) can be determined from the superelasticity curves.

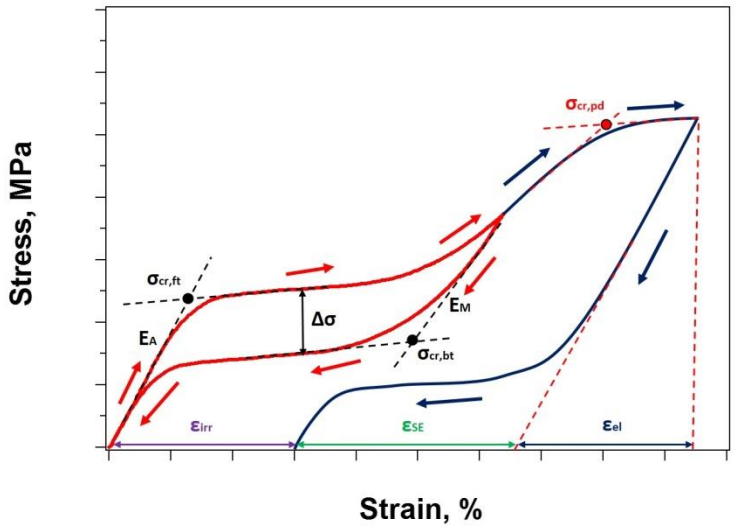

Figure 1-5 A schematic of the superelasticity behavior of shape memory alloys

It is observed that the SME occurs as a result of thermal cycling between A_f and M_f temperatures while SE is due to stress induced martensitic transformation at temperatures above A_f. Since the martensitic transformation in SMAs is temperature dependent as it is shown in Figure 1-6 a, the stress-temperature relationship in SMAs needs to be described.

The Clausius-Clapeyron relationship (CC) is the best equation to explain this relationship [14]:

$$\frac{d\sigma}{dT} = -\frac{\Delta S}{\varepsilon_{tr}} = -\frac{\Delta H}{\varepsilon_{tr} T_0} \qquad 1\text{-}3$$

where σ is the uniaxial stress, ε_{tr} is the transformation strain, ΔS is the entropy of transformation per unit volume, ΔH is the enthalpy of transformation per unit volume, and T_0 is the equilibrium temperature of transformation which was given in equation1-2. The enthalpy changes of the forward and reverse martensitic transformation can be obtained by measuring the area of cooling and heating curves of thermal induced transformation in the absence of stress results. The entropy of martensitic transformation can be express as follows:

$$\Delta S = \frac{\Delta H_{avg}}{T_0} \qquad 1\text{-}4$$

Since ΔS, ΔH and T_0 are constant for a given system, hence the relation between stress and strain is linear. Not just the critical stresses for martensitic transformation, but the martensite reorientation and slip are strongly testing temperature dependent. If the material is in martensite and deformed below A_s, critical stress for the martensite reorientation decreases with temperature due to increased mobility of internal twins and martensite plates boundaries. If the material is in austenite and deformed between M_s and A_f (M_s<T<A_f), stress-induced martensite is formed during loading where critical stress for martensitic transformation increases with temperature and shape recovery cannot be observed upon unloading. Shape recovery occurs when the temperature is increased above A_f temperature. Superelasticity is observed when the sample deformed between A_f and M_d (A_f<T<M_d). Stress-induced martensite cannot be observed above M_d (martensite desist

temperature) and alloys deform like conventional materials [15]. M_d can be considered as the intersection of critical stresses of martensitic transformation and slip, as shown in Figure 1-6 b. If the material is not strong enough or the temperature is close to M_d, partial recovery can be observed since martensitic transformation and plastic deformation occur simultaneously. If the sample is deformed above M_d, plastic deformation takes place before martensitic transformation where shape recovery cannot be observed during unloading. Thus, superelasticity can only be observed between A_f and M_d where the difference between these temperatures is called superelastic window (Figure 1-6 b).

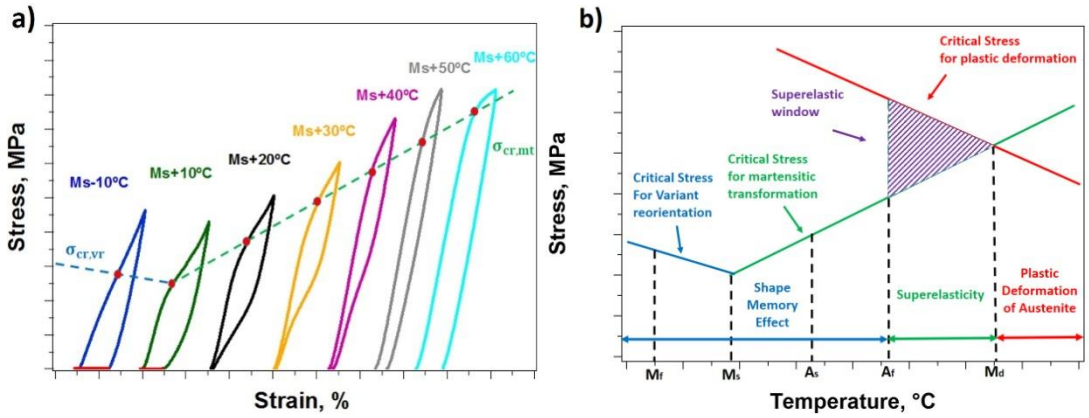

Figure 1-6 Schematic of a. stress-strain curves, b. the critical stress of SMAs as a function of temperature [16]

1.3 NiTi SMAs

The three commercially important SMAs are NiTi, CuZnAl, and CuAlNi. In NiTi, austenite crystal structure it is Body Centered Cubic (BCC) lattice, which has a B2 structure while martensite is monoclinic and has B19' structure (Figure 1-7). In some cases of NiTi alloys, the intermediate R-phase also appears during the transformation. R-phase has rhombohedral structure, low transformation strain, and temperature hysteresis (1-10°C)

[17, 18]. The formation of R-Phase in NiTi alloys can be due to several reasons such as cold working, aging of Ni-rich alloys, and alloying with the third element like Fe [19].

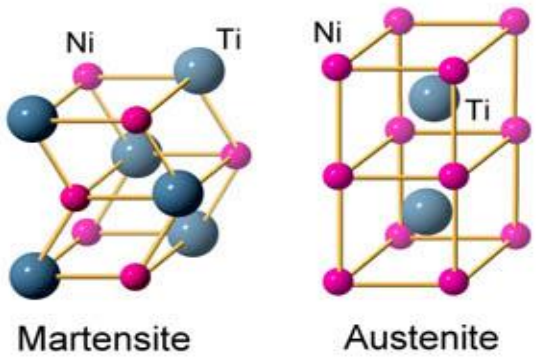

Figure 1-7 Crystal structures of martensite and austenite of NiTi

NiTi alloys also known by their brand name Nitinol with their widespread applications in aviation, automotive and industry, are the most common and commercially available SMAs. Particularly, a very large number of biomedical application of NiTi has been reported in orthodontics, cardiovascular, and surgical instruments so far. In addition to the described shape memory effect and superelasticity, high damping property, excellent erosion [20], corrosion [21], wear resistance [22, 23], good dimensional stability, ductility, workability and biocompatibility [24, 25] has made NiTi alloys fabulous materials for biomedical applications. NiTi alloys are capable of recovering large strains (up to 8%) while for a conventional material like stainless steel the recoverable strain is less than 0.5%. As an intermetallic, this alloy has good ductility (which is related to the martensitic transformation with different deformation modes), low anisotropy and relatively small grain size [26].

1.3.1 Effect of Ni Content in Composition

Nitinol is typically composed of approximately 50 to 51 at% nickel (55 to 56% weight percent). NiTi alloys that contain more than 50.6 at.% nickel are more sensitive to aging and have superior cyclic stability compared to equiatomic NiTi SMAs and are known as Ni-rich NiTi [27]. Near equiatomic NiTi alloys have limitations such as low strength and, poor cyclic stability [28]. They also have relatively high TTs for biomedical applications. Transformation temperatures of NiTi alloys are very sensitive to the Ni content. Binary NiTi alloys have TTs typically between -40˚C and 100 ˚C and show a temperature hysteresis of 20–40 ˚C [29-31]. Making small changes in the composition can change the TTs of the alloy significantly. With having slightly higher Ni content in NiTi alloys it is possible to decrease TTs of the alloys considerably (about 93 °C/at% with Ni content) [32, 33].

Figure 1-8 displays M_s variation with Ni content of the alloy. TTs are decreased drastically with enriching the alloy with Ni, whereas they are almost composition independent on the Ti-rich side. Altering of TTs in NiTi is also possible with alloying. Among the many elements investigated alloying additions to NiTi, Hf, Zr, Pd, Au, and Pt are known to increase the TTs [34]. An alternative way to increase the strength and control the TTs in NiTi alloys is thermo-mechanical treatments (e.g., cold working and post-annealing) [17] that will be discussed in next section.

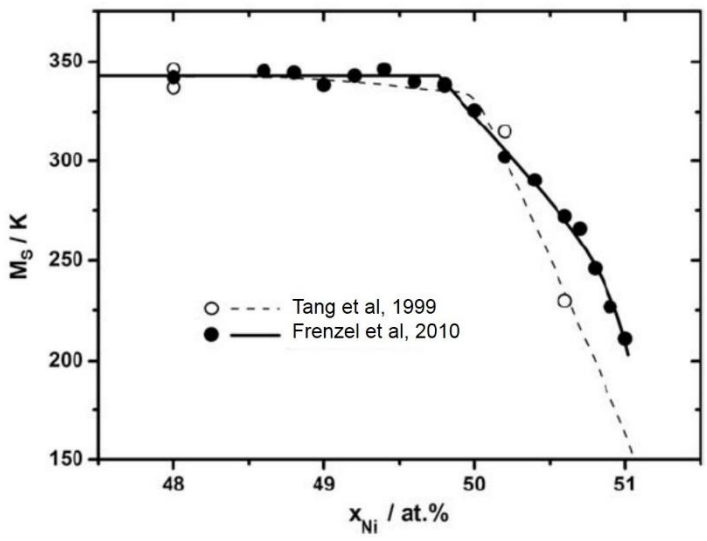

Figure 1-8 Influence of the Ni content on the M_s temperature [33]

Increasing the Ni content offers some other advantages aside from TTs controlling. Ni-rich alloys inherently have higher strength of material and are very responsive to aging [1]. It has been reported that Ti-50Ni and Ti-50.5Ni (at. %) do not show superelasticity in the solutionized conditions due to low strength [31]. Figure 1-9 depicts the effects of Ni content in superelastic response of NiTi wires annealed at 400 ºC and tensile tested at 37 ºC. The improvement in superelastic response can be clearly seen. The critical stress required for martensitic transformation and the strain recovery are both increasing with increasing Ni content.

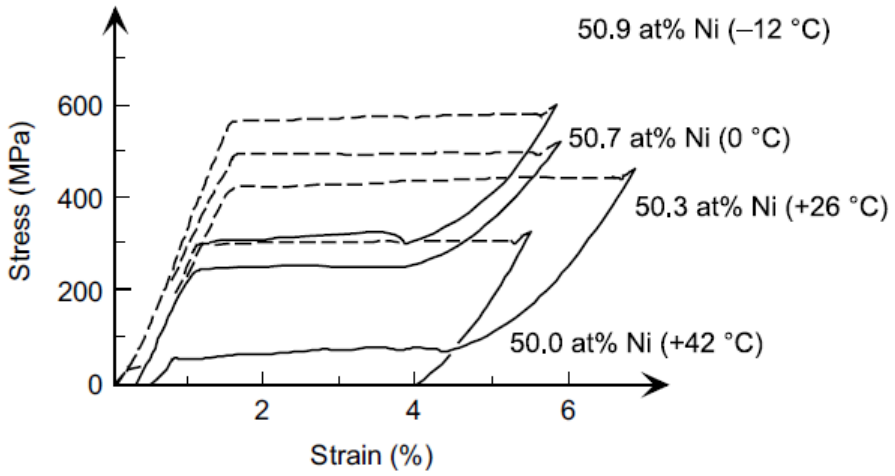

Figure 1-9 The effect of Ni-content on the superelastic deformation [35]

1.3.2 Effects of Aging on NiTi alloys

As it was shown in the previous section, near equiatomic NiTi alloys do not show promising superelasticity due to their low strength [28] while Ni-rich NiTi alloys are more likely to show superelasticity since they have a higher intrinsic strength [9]. The heat treatment can be utilized as one of the most effective and practical methods in order to increase the strength of NiTi alloys and also adjust the TTs. Even in equiatomic NiTi alloys, although the matrix is not strong enough to observe perfect superelasticity in the homogenized condition, it is possible to obtain full recovery after proper thermo-mechanical processing [17]. The NiTi phase diagram is crucial for heat-treatments of the alloys, thus the binary NiTi phase diagram is given in Figure 1-10 [36].

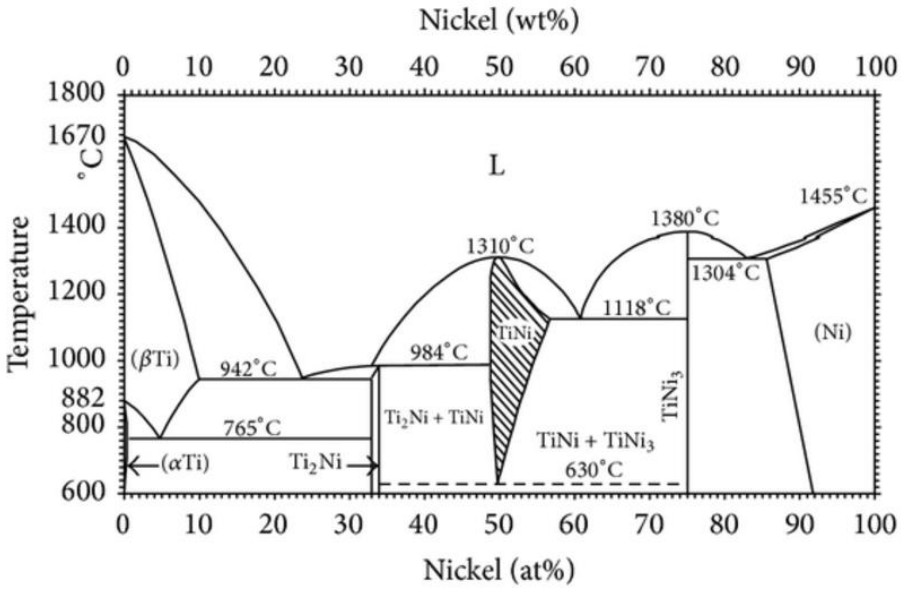

Figure 1-10 Equilibrium Ni-Ti phase diagram [36]

Ni-rich alloys are even more sensitive to aging. Figure 1-11 displays a variation of TTs of a $Ni_{50.8}Ti_{49.2}$ SMA wire as a function of time and temperature. When the Ni content is lower than 50.5 at. %, the nucleation rate is slow and precipitation process is affected by the grain boundaries because the precipitate nucleation rate is higher at grain boundaries rather than in the grain interiors. Therefore, the formation of precipitation is inhomogeneous. However, for high Ni content alloys, nucleation rates at grain boundaries and grain interiors are similar, and the precipitation happens homogenously throughout microstructure [17, 37]. In Ni-rich alloys Ni-rich metastable to stable secondary phases respectively: Ni_4Ti_3, Ni_3Ti_2, and Ni_3Ti precipitates can be formed [27, 38] where they improve the strength of material with acting as obstacles for dislocation motion [39]. Formation of such Ni-rich precipitates also deplete the Ni-content of the matrix and thus, increases the TTs.

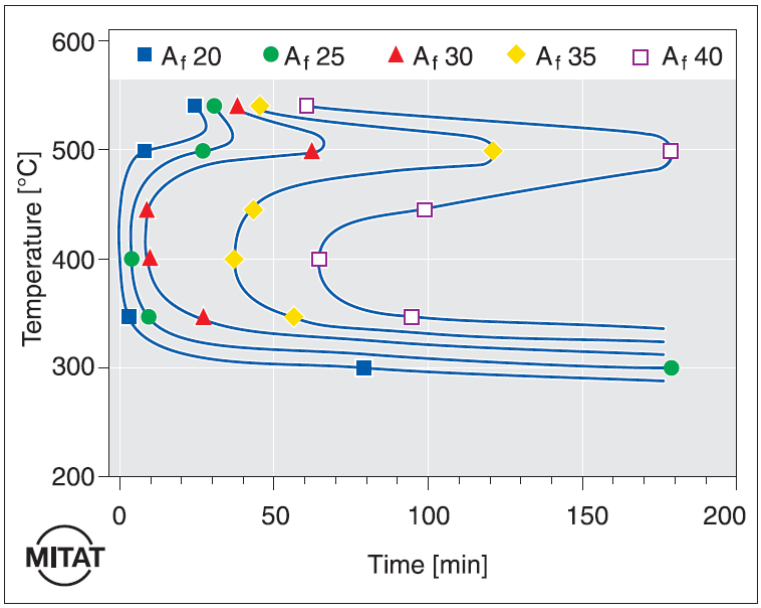

Figure 1-11 Effect of ageing temperature and time on the transformation temperature of $Ni_{50.8}Ti_{49.2}$ Nitinol wire with a starting A_f temperature of 11°C [40]

It is noteworthy, the precipitation characteristics and the corresponding shape memory properties are highly dependent on aging temperature, aging time, and cooling rate [27, 41-43]. The aging time and temperature control the composition, quality, and quantity of precipitates in NiTi matrix. For instance, with low temperatures or short time aging, metastable Ni4Ti3 precipitates are formed while the stable Ni3Ti phase is introduced into matrix after high temperature or long duration aging. Figure 1-12 the TEM micrograph of annealed and 4h-500°C aged $Ni_{51}Ti_{49}$ Showing the homogenous distribution of Ni_4Ti_3 lens-shaped precipitates [44]. The strength and TTs are also highly dependent on the precipitation properties, i.e. size, volume fraction, and the distance between particles. Another effective mechanism is the created local stress fields around the precipitates. TTs are increased with correctly oriented stress fields that help to nucleate the martensite. However, whenever the stress fields are around the fine precipitates with the small interparticle distance they generate obstacles and resists the martensitic transformation and

TTs are decreased [45]. Eventually, all these competing mechanisms causing from heat treatment determine the strength, shape memory properties, and TTs of the NiTi part.

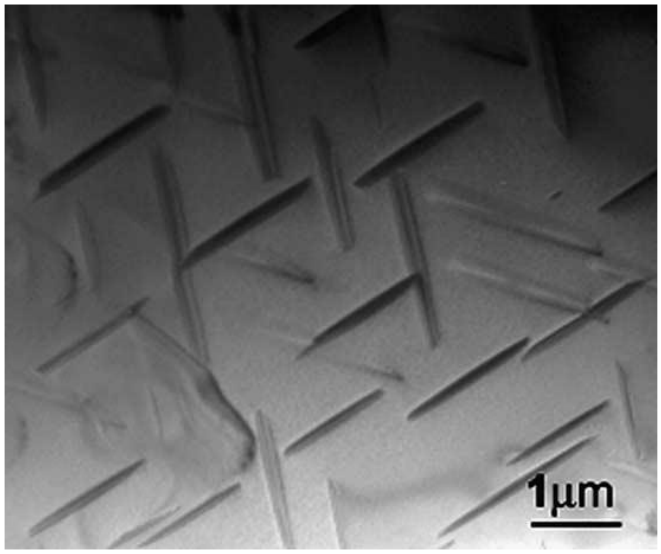

Figure 1-12 TEM image showing homogenous distribution of Ni_4Ti_3 lens-shaped [44]

1.3.3 Effect of Crystallographic Orientation

Other than heat treatment, the crystallographic orientation of the alloy is a determining factor in shape memory response of SMAs. The theoretical recoverable strains for a single crystal NiTi with different orientations can be estimated from the phenomenological, lattice dependence and energy minimization theories of martensitic transformations. The transformation of austenite to martensite might happen in several ways that are called martensite lattice correspondence variants. A total of 12 lattice correspondent variants are available in the cubic to monoclinic transformation of NiTi and each martensite CVP is described by a unique habit plane normal and transformation shear. The Resolved Shear Stress Factor (RSSF) of each variant can be calculated based on the orientation relationship between the applied stress direction and the particular habit plane variant [34]. When the resolved shear stress on the most favorably oriented martensite CVP

reaches a critical resolved shear stress, the transformation proceeds on that CVP [13]. The resolved shear stress must be in the specific direction in order to trigger the transformation because the martensitic transformation is active only along certain directions on certain planes. Thus, the variants with greater RSSF are more likely to be activated. Figure 1-13 depicts the crystal orientation dependence of superelasticity of single crystalline $Ni_{50.8}Ti_{49.2}$ SMA samples all aged at 1.5h-500ºC under compression. It can be clearly seen functional properties of single crystal NiTi such as critical stress for martensitic transformation $\boldsymbol{\sigma_{SIM}}$ and recoverable strain $\boldsymbol{\varepsilon_{rec}}$ are highly dependent on the relation between crystallographic orientation and applied stress direction. The [148] and [001] orientations show remarkable superelasticity with Luders type behavior and more than 8% strain recovery while the [111] and [112] orientations show only 4.8 and 3% superelasticity respectively. The $\boldsymbol{\sigma_{SIM}}$ and stress-strain slope is significantly lower in [148] and [001] directions in comparison with [111] and [112] orientations. The high stress-strain slope in such orientations leads to quick approach to the critical stress without acquiring a significant strain change and plastic deformation. This phenomenon that is also called stress hardening also results in smaller superelastic window. Therefore, CC slope has been reported to be different for crystallographic orientations in NiTi alloys. For instance the CC slope for aged [111] oriented $Ni_{51.5}Ti_{48.5}$ has been reported to be 9.3 but 7.5 MPa/ ºC in [110] orientation [46]. Figure 1-14 shows the maximum achievable transformation strain of different crystallographic orientations based on energy minimization theory under tension and compression for $Ni_{50.8}Ti_{49.2}$. The higher RSSF has an orientation, the lower critical stress but greater recoverable strain is observed. The estimation of maximum strain recovery, RSSF for some orientations based on energy minimization and phenomenological theories

are given in Table 1-1. Additionally, the theoretical numbers can be compared to the experimental results of aged $Ni_{50.8}Ti_{49.2}$.

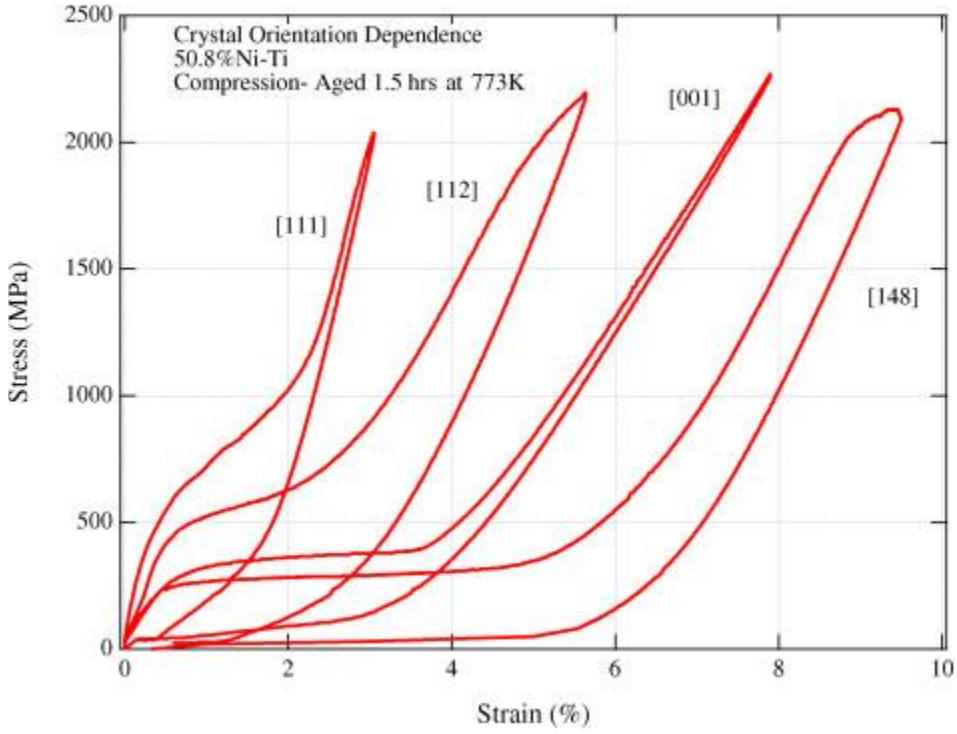

Figure 1-13 Crystal orientation dependence of superelastic response of single crystalline $Ni_{50.8}Ti_{49.2}$ under compression [33]

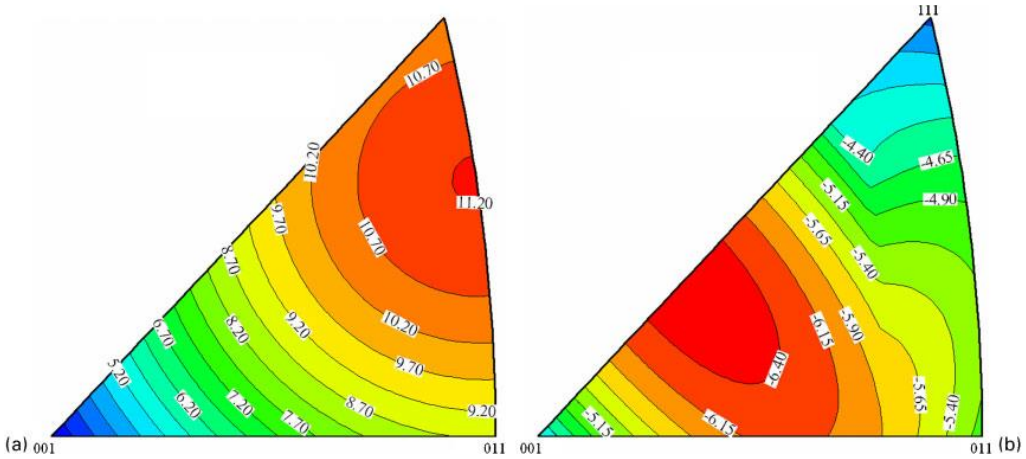

Figure 1-14 Maximum transformation strains as a function of the crystallographic direction of uniaxially applied stress in a $Ni_{50.8}Ti_{49.2}$ under a. tension and b. compression [34, 47].

Table 1-1 The Orientation dependence theoretical prediction and experimental results comparison for single crystal $Ni_{50.8}Ti_{49.2}$ [13].

$Ni_{50.8}Ti_{49.2}$	**Theory**				**Experimental**	
Theory / **Orientation**	Energy Minimization		Phenomenological		1 h-450 ºC	1 h-550 ºC
	ε_{rec}	RSSF	ε_{rec}	RSSF	ε_{rec}	ε_{rec}
[001]	4.4%	0.39	5.2%	0.4	3.6%	4.2 %
[111]	3.6%	0.25	3.5%	0.27	1.8%	2.5%
[112]	5.1%	0.44	5.0%	0.39	3.3%	3.5%
[148]	6.2%	0.51	6.0%	0.49	6.5%	5.6%

In polycrystalline alloys, grains are distributed in different orientations which are known as a texture. If a polycrystalline has a strong texture in a certain orientation, then similar shape memory behavior of the single crystal oriented in the same direction can be expected. In most cases, the texture of a polycrystalline is random where the behavior can

be assessed with an average of a single crystal of all available orientations in the sample. Nevertheless, an exact estimation of a randomly textured polycrystalline is hard and complicated due to several independent deformation systems [34]. However, is possible to create a texture in polycrystalline in order to achieve similar behavior of the desired single crystals with a specific orientation. Such texture can be introduced by thermo-mechanical treatments like cold rolling, extrusion or cutting the specimen in certain directions. Controlling the texture in such traditional techniques is very challenging due to the severe plastic deformation during the procedure.

1.4 Fabrication of NiTi Components

Fabrication of NiTi alloys is exceedingly difficult, due to the compositional control requirements during the process. The structural, and functional properties of NiTi are highly fabrication and process parameter dependent since these properties are very sensitive to nickel-titanium ratio, picked up impurities and formed secondary phases. In addition, poor thermal conductivity and enormous elasticity of the alloy which leads to increase die or roll contact and eventually results in frictional resistance, make machining of the NiTi extremely challenging. Figure 1-15 shows major problems of NiTi machining. Therefore, each step in the fabrication of NiTi parts requires a deep understanding of its effects on performance and quality of final Product. The most common fabrication routes for NiTi alloys will be discussed briefly in following sections.

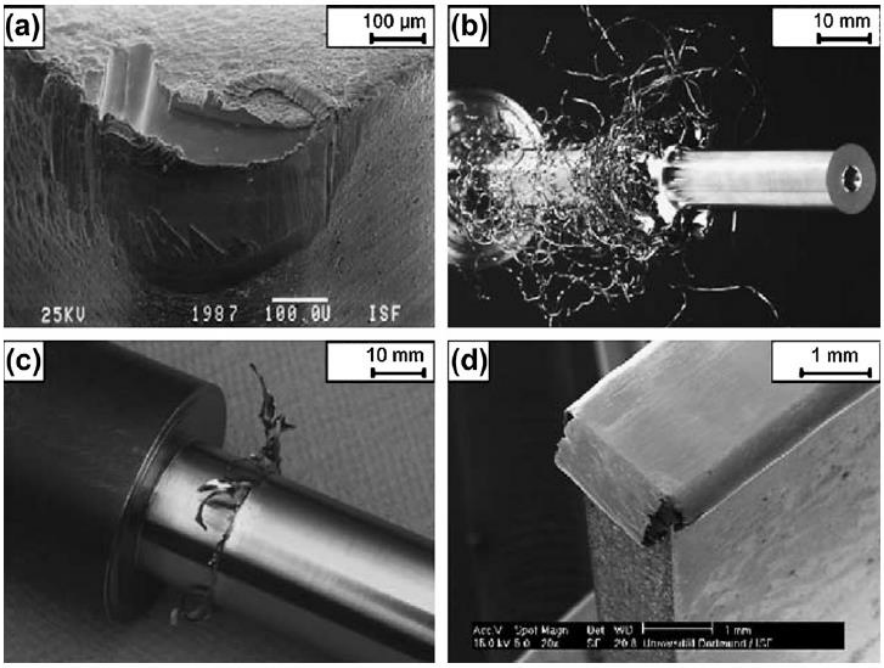

Figure 1-15 Major drawbacks in machining NiTi shape memory alloys: (a) high tool wear; (b undesirable chip formation; (c) formation of burrs after turning (d) and grinding [48]

1.4.1 Melting and Casting

Although there is no single recipe for the production of NiTi ingots, conventionally Vacuum Arc Melting (VAM) or Vacuum Induction Melting (VIM) followed by a hot working process and machining to the final shape. To minimize the possibility of contamination during melting, an inert gas working atmosphere is used [26]. However, titanium is highly reactive, therefore, high-temperature processing such as melting and alloying is always accompanied by formation Ti-rich phases and consequently higher impurity level. Figure 1-16 illustrates a laboratory setup for VIM processing of binary NiTi ingot metallurgy in a graphite crucible and starting with pure elemental Ni pellets and Ti rods. Additionally, as it was mentioned, machining of NiTi is very challenging [26] and the significant heat generation throughout a machining process can affect the functional

properties of fabricated parts [49, 50], in addition, conventional processing routes do not allow for the production of porous NiTi [51]. Powder metallurgy methods are generally used to fabricate porous NiTi components.

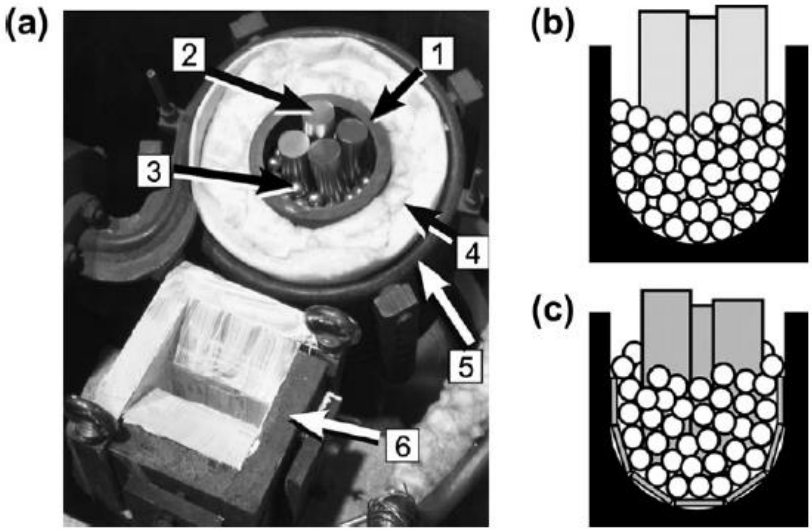

Figure 1-16 (a) Laboratory setup for VIM processing of binary NiTi (1 – graphite crucible; 2 – Ti rods; 3 – Ni pellets; 4 – isolation; 5 --water cooled copper coil; 6 – mold); (b) schematic illustration of the crucible filling with Ni pellets in contact with the graphite [26, 52]

1.4.2 Powder Metallurgy (PM)

Powder metallurgical (PM) processing routes are highly attractive since they lead to near net shape component and therefore may overcome challenges of the traditional routes. Some of the PM technologies also have great potential for manufacturing open cell porous NiTi [53]. Several powder metallurgy methods have been used to produce porous NiTi alloys, such as conventional sintering (CS), spark plasma sintering (SPS), self-propagating high-temperature synthesis (SHS) and metal injection molding (MIM). Summary of NiTi manufacturing methods is illustrated in Figure 1-17.

However, NiTi components produced by PM usually contain high contaminant levels [50] due to several reasons like the large specific surface area of the powder, and at least two additional high-temperature processing steps (Powder production and PM process) [43] which may degrade the structural and functional properties of NiTi considerably. For PM processing the pre-alloyed NiTi, the powder is desired since in the case of using the elemental Nickel and Titanium powders, the formation of secondary phases or areas consist of pure Nickel or Titanium is unavoidable [54]. As mentioned powder production is one of the most important steps in PM manufacturing. The particle shape, size, and distribution determines the physical properties of powder such as bulk and compacted density, and flowability [55]. The powder preparation methods include Mechanical attrition or ball milling, atomization in water or gas, hydrating, and creating powder by laser ablation. The gas atomization method seems to be most applicable for NiTi alloys due to either difficulty or drawbacks of other methods [43]. Recently, Additive Manufacturing (AM) methods with tremendous advantages over both conventional routes and other powder metallurgy techniques, have been introduced for manufacturing NiTi parts. The method makes fabrication of porous, complex, engineered and application specific parts feasible with low impurity level. Furthermore, it is possible to control the level of porosity, pore size, and shape of fabricated porous parts. Next section will be allocated to the description of the additive manufacturing types and processes.

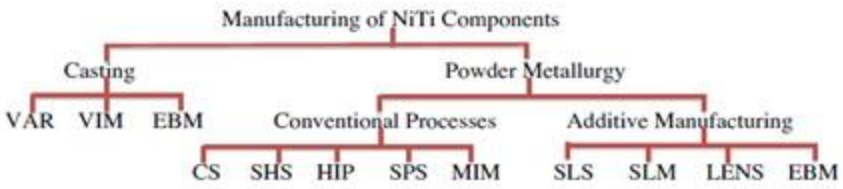

Method	Description	Method	Description
VAR	Vacuum Arc Remelting	SHS	Self-propagating High Temperature Synthesis
VIM	Vacuum Induction Melting	HIP	Hot Isostatic Pressing
EBM	Electron Beam Melting	SPS	Spark Plasma Sintering
CS	Conventional Sintering	MIM	Metal Injection Molding
SLS	Selective Laser Sintering	LENS	Laser Engineered Net Shaping
SLM	Selective Laser Melting		

Figure 1-17 Summary of the NiTi manufacturing methods [26]

1.5 Additive Manufacturing (AM)

Most of the PM methods lack homogeneous control of porosity (e.g. amount of porosity, pore size, the arrangement of pores, and interconnection of pores), chemistry (impurity content, homogeneity, intermetallic), geometric flexibility and freeform design. Formation of secondary phases in the case of elemental powder usage is unavoidable since their formation is much more favorable thermodynamically compared to the formation of NiTi [54]. Undesirable secondary phases and contamination do not only affect mechanical properties, but they also make the foam brittle and additionally change phase transformation temperatures, which are important for practical applications [54]. Another major limitation of these processes (except MIM) is that they cannot produce complex geometries. Therefore, most of NiTi devices are made in the form of simple geometries, such as wire, sheet, tube, and bar. Additive Manufacturing (AM) is a very attractive method for overcoming mentioned problems in the fabrication of porous NiTi alloys.

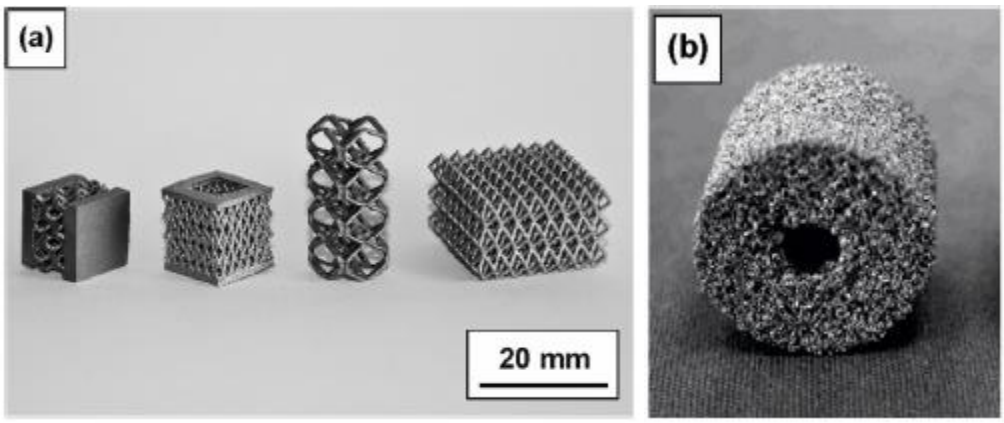

Figure 1-18 Complex NiTi implants and scaffolds produced by AM [56] b. Porous NiTi inter body fusion device Actipore™ produced by SHS methods, photography [57]

The typical, ASTM-recognized AM methods are material extrusion, material jetting, sheet lamination, vat photopolymerization, binder jetting, directed laser deposition (DLD) and powder bed fusion (PBF) [58]. When it comes to the AM of metallic parts, the DLD and PBF processes are the most proven and feasible methods. DLD method consists of blown powder and in situ laser melting whereas, most common PBF systems use either laser or electron beam as a thermal source to induce fusion between metal powder particles. Powder Bed Fusion-Laser (PBF-L), also referred to as Selective Laser Melting (SLM) while Powder Bed Fusion-Electron beam is named as Electron Beam Melting (EBM). Other than thermal source there are other differences in terms of atmosphere, powder pre-heating scanning, etc between these two methods. SLM process is typically done in the inert-gas atmosphere to reduce the oxidization rate of the part during the build whereas EBM is done under vacuum. While EBM can only be used for metal fabrication SLM can be employed for metals, ceramics, and even polymers. The SLM fabricated parts also have higher quality in terms of surface finish and resolution [59].

Since Nitinol powder is not commercially available so far, one has to begin from ingot and powder preparation. Particle size, shape distribution flowability, and packing density are general requirements for any powders used for AM [60]. The used powder particles should be as small as possible for the deposition of thin powder layers and the powder fraction has to have a multimodal particle size distribution for increasing the packing density. Having a powder bed with high packing density supports the production of parts with higher density compared to loose powder bed [55]. Gas atomization technique is usually employed for powder processing of AM. The method allows for the production of spherical particles that displays better flowability compared to sharply shaped particles. It is noteworthy that although small powder particles are preferred for AM, but very fine particles lose their flowability due to higher surface-volume–ratio. For Nitinol particles in fractions smaller than 20-63 μm have insufficient flowability and only 56% packing density while Particle fractions of 25-75 μm and 45-100 μm show a packing density of about 60 % and goof flowability [61]. Preparation of Nitinol powder is also challenging in terms of preventing from impurity pick up (particularly oxides and carbides) than regular metals such as steel. Electrode Inert Melting Gas Atomization (EIGA) seems to be most efficient to avoid impurity pick up so far [62]. However, even for this method significant amount of oxygen pick up has been reported [63]. The amount of impurity level is also relevant with particle size and it is higher when the particle size is decreased due to higher exposed surface area. Table 1-2 compares the suitability of powder fractions for AM in terms of size, shape, flowability, packing density, impurity contents, transformation ability and mass fraction after atomization. It is observed that medium-sized fractions between 25-75 μm seem to be most proper for Nitinol fabrication through AM.

Table 1-2 Qualitative classification of different powder fractions of their suitability for AM [60].

	<25µm	<45µm	20-63µm	25-75µm	45-100µm
particle size	●	◕	◑	◑	◕
spherical shape	●	●	●	●	●
flowability	○	○	◕	◕	◕
packing density	◕	◑	◑	◑	◑
impurity content	◕	◕	◑	◑	◕
transformation ability	●	●	●	●	●
mass fraction	◔	◕	◑	◑	◑

● = fulfilled requirement ○ = unfilled requirement

After powder preparation, a uniform ‘bed’ of powder is first deposited and then specific regions of the bed are melted by the laser beam according to a previously imported CAD design in order to build a single layer of the part. Upon the completion of a single layer, the powder bed is lowered by the height of the deposited layer, a new bed of powder is deposited on a roller, and the process is repeated. The part is built upon a base plate (i.e. build plate, substrate, platen), and the finished part must be sheared off from the base plate after the AM process. This is typically accomplished by electrical discharge machining (EDM). Figure 1-19 shows a schematic of PBF process.

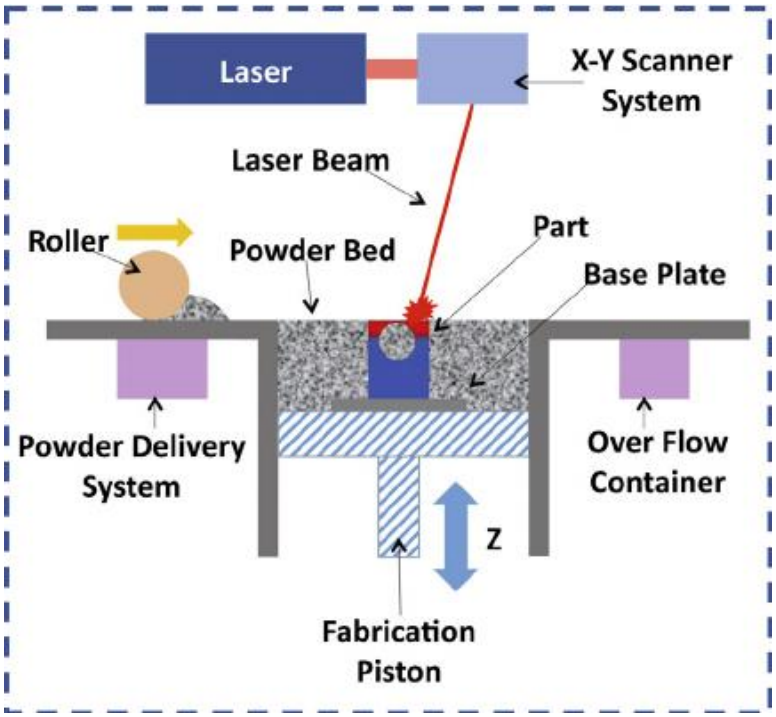

Figure 1-19 The Schematic of Powder Bed Fusion-Laser process [58]

Generally, the term additive manufacturing describes processes which are used to create physical parts directly from CAD data by adding material in successive layers [51]. The layers are provided in powder and melted. The procedure is repeated until the 3-D part is produced. Figure 1-20 schematically describes the AM process for fabrication porous NiTi.

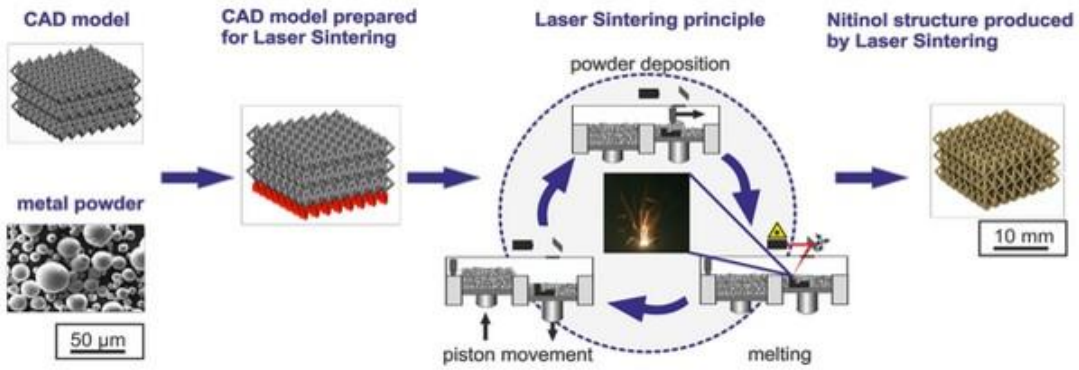

Figure 1-20 Schematic of the principle of powder bed-based AM of a complex NiTi [51]

1.6 SLM Fabricated NiTi alloys

The initial laser fabricated NiTi compounds were introduced in early 2000's using SLS method [64-66]. The early research was more focused on the feasibility of such fabrication and structural properties. The shape memory effect and microstructure of SLS fabricated NiTi were studied by Shishkovsky, [67, 68]. Shape memory effect in SLM NiTi cantilever beams for potential MEMS applications was reported by Clare, et al [69]. The method started to gain a significant attraction from the late 2000s. Functional properties and cyclic response of near equiatomic SLM NiTi was studied and compared to conventionally fabricated NiTi alloys by Meier et al [70-72]. Superelasticity and cyclic stability of Ni-rich SLM NiTi was subjected to later studies and exhibited distinct shape recovery which compares favorably with the response of conventionally processed NiTi [73-75]. Later, effects of SLM process parameters on phase transformation behavior and temperatures, microstructural features and mechanical response studied in more details. Dadbakhsh, at al, showed SLM parameters greatly influence TTs and mechanical response of dense and porous NiTi [76, 77]. Bormann et al focused on microstructure and texture of SLM NiTi with considering different fabrication parameter as well as scanning strategies and documented the tailorable microstructure via SLM process parameters [78-80]. Effects of process parameters also studied on geometrical characteristics of porous SLM NiTi [81]. Wild et al [82] showed there is no significant difference between damping properties of SLM NiTi and conventional NiTi and the biocompatibility of SLM NiTi was verified by Habijan [83].

1.7 Motivation

NiTi alloys are the most well-known and widely used SMA due to their exceptional shape memory effect, superelastic properties, excellent corrosion, wear resistance, high ductility, and work output. The combination of these unique features with biocompatibility makes NiTi a very promising candidate for biomedical applications as well. In this regard, near equiatomic NiTi alloys have been subjected to many studies. However, it has been reported that Ti-50Ni and Ti-50.5Ni (at. %) do not show superelasticity in the solutionized conditions due to low strength [31]. The leading and practical method to improve the shape memory properties is the use of aged Ni-rich NiTi alloys and precipitation formation [27, 42, 84]. The strengthening ability of such precipitates depends on their size, volume fraction and inter-particle space [85, 86] and their characteristics are highly dependent on aging temperature, aging time, and cooling rate [27, 41-43].

Composition, impurities, texture and precipitation characteristics of NiTi alloys all are also affected by manufacturing methods and parameters [43, 87]. The structural, and functional properties of NiTi of fabricated through various routes can be distinct since these characteristics are highly fabrication and process parameter dependent. Therefore, each step in the fabrication of NiTi parts requires a deep understanding of its effects on quality and performance of the final Product. The traditional routes of NiTi fabrication methods are exceedingly challenging due to the sensitivity of NiTi compositional control, picked up impurities, and machining difficulties. Recently introduced Selective Laser Melting (SLM) is an attractive Additive Manufacturing (AM) approach that employs CAD data to selectively melt the metal powder via a laser beam. During the SLM process, parameters such as laser power, powder layer thickness, scanning speed, spacing, and strategy are all

involved. The energy density of fabricated parts is calculated combining all these parameters which are a determining factor in the microstructure, grain formation, and texture. The flexibility of these process parameters in SLM can be employed in order to control and alter substantial features of NiTi compounds such as transformation temperatures, the microstructure, texture, and consequently the mechanical response. In addition influence of post processing heat treatments on NiTi alloys fabricated through SLM process can be entirely different from conventional NiTi alloys due to effects of SLM process on composition of fabricated parts.

The method also opens a new window in overcoming traditional fabrication problems besides allows for the production of complex shaped dense or porous parts based on applications requirements with low impurity levels. Porous NiTi alloys can be engineered and fabricated to optimize their mechanical and material properties based on the specific application requirements. However, the thermo-mechanical response of porous NiTi can be different and more complex than that of a dense NiTi. So far only a few studies have been conducted on the shape memory properties of SLM fabricated NiTi parts. Systematic studies are needed to better understand the relationship between the fabrication parameters and the shape memory behavior in order to be able to engineer the shape memory properties of laser manufactured NiTi components.

1.8 Objectives, and Technical Approach

In the present study, first a wide range of fabrication parameters such as laser power, scanning speed and space have been investigated individually and the influence of each parameter on transformation temperatures, hardness, microstructure, texture, and the mechanical response has studied. To understand the thermomechanical behavior of SLM

$Ni_{50.1}Ti_{49.9}$, $Ni_{50.8}Ti_{49.2}$ (atomic %) alloys fabricated with selected process parameters were characterized in as-fabricated and solutionized forms and compared with the reference ingot. Additionally, effects of subsequent aging on SLM fabricated $Ni_{50.8}Ti_{49.2}$ in both as-fabricated and solutionized conditions were investigated and time and temperature dependent phase transformation charts are presented. Microhardness tests were utilized to estimate the strength of the alloys as a function of aging time and temperature prior to the mechanical tests. Five types of thermomechanical experiments were performed; i) Failure tests: to examine ductility, yield strength and critical stresses of the samples, ii) Cyclic shape memory effect tests: to observe the cyclic stability of samples, iii) Thermal cycling under stress tests: to determine the thermal hysteresis, transformation strain, strength and work output of material, which are the main factors for actuator applications, as a function of applied stress, iv) Isothermal cyclic loading/unloading: to observed stabilized superelastic response, and v) Isothermal stress-strain experiment: to investigate the critical stress for phase transformation (or variant reorientation), strain recovery or superelasticity, stress hysteresis, Young's modulus of transforming phases as functions of temperature. The results from thermal and stress cycling were used to determine the phase diagram with Clausius- Clapeyron (CC) slope. To tune the stiffness of NiTi parts for potential implant applications porosity introduced to SLM NiTi parts and influence of porosity level and geometry on mechanical response was studies. Considering such applications, special attention was given to superelastic response of the parts at room or body temperatures. Therefore, adjustment of TTs was also targeted and shape memory responses of the dense and porous fabricated parts evaluated exclusively at these temperatures. In this work, the microstructure and texture of SLM fabricated NiTi alloys were analyzed and their

correlation to the mechanical results was addressed. To develop, process and characterize shape memory and material properties of SLM NiTi alloys, the following objectives are proposed:

- Investigate the effect of SLM process parameters such as laser power, scanning speed, and hatch spacing on TTs, microstructure, and mechanical response of Ni-rich NiTi.
- Reveal the functional and structural differences between conventionally fabricated Ni-rich NiTi and SLM NiTi
- Study effects of aging on shape memory response of as-fabricated Ni-rich SLM NiTi.
- Study effects of aging on shape memory response of solutionized Ni-rich SLM NiTi.
- Investigate the texture formation in Ni-rich NiTi as a result of SLM fabrication and its correlation with mechanical response.
- Explore the right heat treatments to adjust TTs and enhance superelasticity of Ni-rich SLM NiTi alloys at room and body temperatures for potential biomedical applications.
- Study the effects of porosity levels on the failure, shape memory behavior of equiatomic and Ni-rich SLM NiTi SMA.
- Study the effects of porosity levels on superelasticity and cyclic response of Ni-rich SLM NiTi SMA.
- Prediction of the superelastic response of SLM NiTi as a function of porosity level.

2 Chapter Two: Experimental Procedure

This chapter is to describe details on the fabrication, technical equipment and experimental methods employed for characterization of the SLM fabricated NiTi alloys throughout this study. The details of material preparation, calorimetric measurements, mechanical testing and microstructural analysis will be presented. This work has been conducted with the collaboration of University of Toledo and University of Kentucky. Fabrication of NiTi specimens was conducted at Dynamic and Smart Systems Laboratory at the department of Mechanical Industrial and Manufacturing Engineering of the University of Toledo. All of the presented results of the current work including mechanical experiments and microstructural evaluation of this research have been performed at the Smart Material's Laboratory at the Mechanical Engineering Department of the University of Kentucky.

2.1 Material Fabrication

$Ni_{50.1}Ti_{49.9}$ and $Ni_{50.8}Ti_{49.2}$ (atomic %) ingots produced by casting obtained from (Nitinol Devices & Components, Inc. Fremont, CA). The ingots were atomized to powder by TLS Technik GmbH (Bitterfeld Germany) using an electrode induction melting gas atomization (EIGA) technique. The scanning electron microscopy (SEM) image of the powder is shown in Figure 2-1 a. and the particle size fraction was found to be ranging from 25 to 75 μm as it can be seen in Figure 2-1 b.

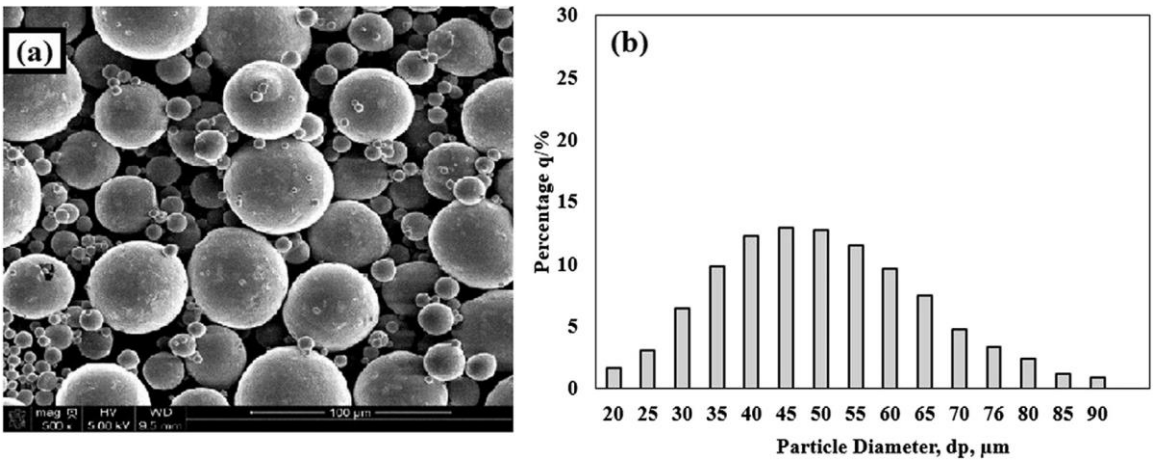

Figure 2-1 a. SEM micrograph of Nitinol powder, b. Particle distribution of the used powders

SLM NiTi samples were fabricated using Phenix system PXM model which is a powder bed fusion (PBF), selective laser melting (SLM) machine (Figure 2-2). Prior to fabrication a 3D CAD model is drawn and imported into the Phenix system specialist software where the CAD design is sliced into the requisite layers. Next process parameters such as laser power, scanning speed, scanning space, etc. are defined. The system which is equipped with a 300 W Ytterbium fiber laser was employed for the selective laser melting. The beam quality of the laser is M2 <1:2, the beam profile is Gaussian (TEM00), and the beam diameter is approximately 80 mm. The machine uses a metal scraper and roller to create the powder layer. The process starts when the feeding piston moves upward and provides the powder. Then, the scraper collects the powder from the feeding piston and the roller deposits it on the building platform. Next, the laser selectively scans and melts the powder according to the geometry requirements of the part provided by the machine control software. A bidirectional scanning strategy was implemented for fabrication of current study. Figure 2-3 is the schematic representation of layer by layer SLM process and scanning strategy.

Figure 2-2 Phenix PXM Selective Laser Melting system

After solidification, dense material remains surrounded by the loose powder. Finally, the building piston drops down to allow for the deposition of the next powder layer. This procedure is repeated until the designed part is fabricated. Impurities of Powder and SLM fabricated Nitinol parts were measured and are given in Table 2-1.

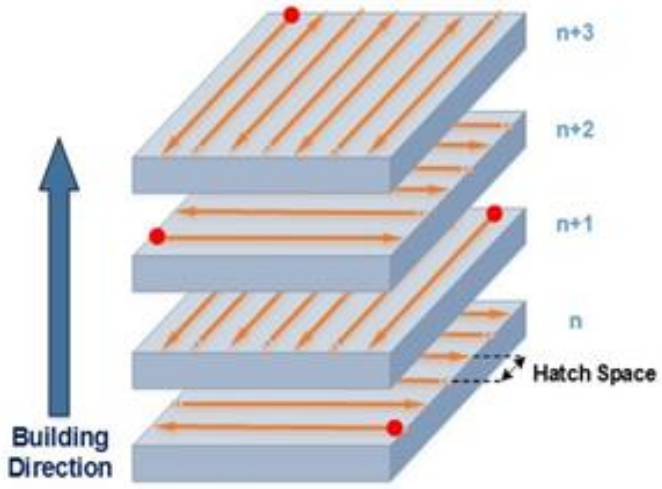

Figure 2-3 A schematic representation of the employed scanning strategy

Table 2-1 Powder and SLM fabricated Nitinol impurities

Nitinol	Carbon(%wt) ASTM E1941	Oxygen(%wt) ASTM E1409	Nitrogen(%wt) ASTM E1477
Powder	**0.0030**	**0.0409**	**0.0031**
SLM	**0.0035**	**0.0502**	**0.0070**

2.2 Material Preparation

The SLM fabricated parts were separated from the base plate using electrical discharge machining (EDM). In addition, the ingot test samples, small pieces for DSC, microstructure analysis, and hardness measurements were by using EDM for each alloy. Figure 2-4 shows the employed KNUTH smart EDM.

Figure 2-4 KNUTH smart EDM

2.3 Heat Treatments

Lindberg/Blue M BF514541 Box furnace used to carry out homogenization of the alloys which is shown in Figure 2-5 a. The maximum temperature that furnace can reach is 1200 ºC. The sized of the chamber is 38.1×38.1×38.1 cm. Homogenization refers to the

process of dissolving precipitate phases created during the casting and/or hot-rolling process without melting the matrix. The heat treatment temperatures were selected based on the binary NiTi phase diagram. For this purpose, two set of SLM NiTi samples were studied. The first set kept in a furnace at 950˚C for 5.5 hours and followed by water quenching at room temperature. In order to avoid oxidization, samples were contained in argon filled quartz ampoules, separated by ceramics and pure titanium. These samples will be referred to as "solutionized" from now on. Following solutionization, samples were aged at temperatures of 350˚C and 450˚C for different time durations from 5 minutes up to 18 hrs. Aged samples were quenched in water at room temperature right after aging. The influence of solutinizing and subsequent aging will be covered in Chapters 4 and 5. Another set of samples were directly aged after fabrication without solutionizing. These samples were aged at temperatures of 350˚C and 600˚C for different time durations from 15 minutes up to 18 hrs at Influence of such aging will be covered in Chapter 5. Aging process was conducted using Whip Mix Pro Press 200 dental furnace (Figure 2-5 b). The furnace has been equipped with a Vacuum Pump.

Figure 2-5 a. Lindberg/Blue M Box furnace (BF514841) b. Whip Mix Pro 200 dental furnace

2.4 Calorimetry Measurements

A Perkin-Elmer DSC Pyris 1 (Figure 2-6) was used to determine the TTs. Typical temperature range is from -150 ºC to 600 ºC and the heating/cooling rate was 10 ºC/min in a nitrogen atmosphere. A small quantity of the material (10-40 mg) was used for DSC. The sample polished to establish good thermal contact. Its weight measured and encapsulated in a sample pan before placing in the holding pan of the furnaces. Another pan was kept empty as a reference. The sample was thermally cycled and the difference of the supplied heat power was recorded. On the calorimetric graph, phase transformations are depicted as peaks and the areas under those peaks indicate the energies of transformations. TTs measured as the intersection of the baseline and the maximum gradient line of a transformation peak as it was shown in Figure 1-2.

Figure 2-6 Perkin-Elmer DSC Pyris 1

2.5 Microstructural Analysis

For polishing, first samples mounted using Epoxy Resin and hardener. BUEHLER EcoMet/AutoMet 250 Grinder-Polisher was used which is shown in Figure 2-7. The grinding procedure involves several stages, using a finer paper for each successive

stage. For polishing, diamond suspensions of 9µm, 6µm and 3µm are used. Finally, alumina suspensions of 1µm and 0.5µm were used to produce a smooth surface.

Figure 2-7 BUEHLER EcoMet/AutoMet250 Grinder-Polisher

Keyence VH_Z250R Optical Microscopy (Figure 2-8) was used to reveal the microstructure. Samples were mounted on epoxy resin and hardeners. For polishing, diamond suspensions of 9µm, 6µm and 3µm are used. Finally, alumina suspensions of 1µm and 0.05µm are used to produce a smooth surface. Samples were etched by H_2O(82.7%)+HNO_3(14.1%)+HF(3.2%) solution for 90 sec.

Figure 2-8 Keyence VH_Z250R Optical Microscopy

Crystal structures of the sample were determined using a Rigaku D/Max Diffraction Unit (XRD). X-ray source was Cu k-alpha and measurements were made at room temperature (RT) with wavelength of 1.5418 $\dot{A}$, step intervals of 0.2º in 2Θ between 35 to 110º and speed of 2º/min. Pole figures were measured at RT using a pole figure goniometer.

Figure 2-9 Rigaku D/Max Diffraction Unit

2.6 Hardness Measurement

Metal-tester Vicker microhardness tester model 900-391D (Figure 2-10) was employed for hardness measurements. Samples mounted in epoxy were polished to a mirror finish prior to measurements. 100 g loads were applied for 15 seconds and removed. As depicted in Figure 2-11 the two diagonals of the indentation left in the surface of the material are measured using a microscope and the area of the sloping surface of the indentation is calculated. 10 indentation were done on each sample and the average was reported.

Figure 2-10 Metal-tester micro Vickers Hardness Tester 900-391D

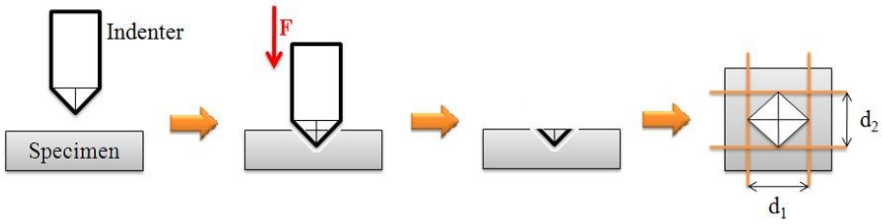

Figure 2-11 Schematic of Vicker hardness measurement

2.7 Thermos-mechanical Testing

Compression tests were conducted by the 100 kN MTS Landmark servo-hydraulic test platform which is shown in Figure 2-12. A strain rate of 10^{-4} sec^{-1} was employed during loading while unloading was performed under force control at a rate of 100 N/sec. The strain was measured by an MTS high-temperature extensometer which was attached to the grips. Heating of the specimens occurred by means of mica band heaters retrofitted to the compression grips with the rate of 5 ºC/min and cooling was achieved through internal liquid nitrogen flow in the compression grips with 2 ºC/min rate.

Figure 2-12 MTS Landmark servo-hydraulic test platform

3 Chapter Three: Effects of SLM Fabrication Parameters

As explained SLM belongs to the family of the additive manufacturing technique that allows production of parts with a wide geometrical freedom. SLM process is operated by a computer aided design (CAD), in which a focused laser beam melts the deposited powder layer locally. The melting is followed by rapid solidification and a subsequent layer is melted likewise and merged to the former layer. The process continues until the CAD-defined design 3-D part is created. The process leads to a different microstructure on fabricated parts in comparison with conventionally fabricated parts because of the epitaxial grain growth. Since during the process a multitude of molten tracks are combined, heat transfer and grain growth are often complex and the repeated energy input causes effects that can play a dominant role for the evolving microstructure [88]. The heat transfer and thermal gradients are greatly affected by fabrication parameter like laser power (p), scan speed (v), scanning space or hatch spacing (h) and powder layer thickness (t). In order to simplify the approach, these parameters are linked and supplied energy via laser beam to a volumetric unite of powder is calculated by:

$$E = p/vht \qquad 3\text{-}1$$

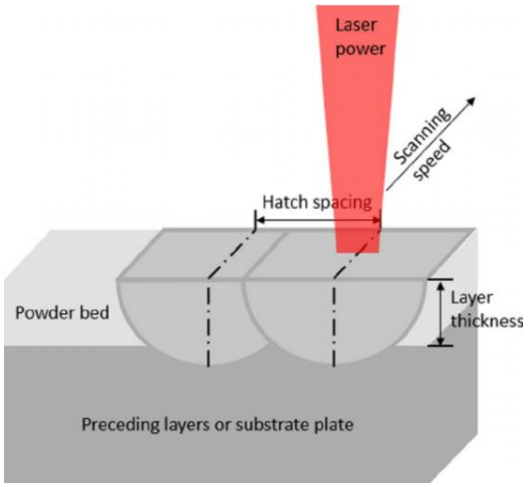

Figure 3-1 SLM process parameters: laser power, scanning speed, hatch spacing, and layer thickness [89].

One of the challenges in SLM is to find the right process window and the related interaction mechanism between mentioned parameters. Therefore, many studies have focused on optimizing mentioned process parameters as well as scanning strategy and building direction on a variety of materials including steels, copper components, and superalloys [90-95]. Distinct process parameters have been reported for different materials. For instance, processing energy density window of 44.4 to 50.8 J/mm^3 have been reported for SLM AlSi10Mg [96, 97]. Li et al. reported increasing of scanning speed leads to higher porosity a smaller molten pool size and eventually lowers the tensile strength of 316 stainless steel [98]. Yadroitsev et al used parametric analysis to introduce optimal SLM parameters to fabricated Inox 904L [99]. It was documented that with more than 400 J.mm^3 energy input dense SLM Co–29Cr–6Mo alloy can be obtained whereas porous builds were formed when the input energy was lower than 150 J/mm^3 [100]. 162-293 J/mm^3 energy density has been reported by Vanderbroucke et al. to produce more than 99% dense Ti6Al4V SLM parts [101]. All in all, the energy density seems to play a crucial role in grain formation and size and according to the Hall-Petch formula [9]. Grain size as one of

the most important parameters of microstructure leads the mechanical properties but the effect of the energy level of SLM fabricated parts does not limit to grain size. Other features of the microstructure such as porosity, melt pool, secondary phases, texture, composition, hardness, etc. are all altered with employed parameters during the fabrication of SLM components. For NiTi alloys, transformation temperatures are also changed due to their sensitivity to the composition. SLM NiTi based superalloys have been also subjected to some studies. The attention to SLM NiTi has been due to a combination of unique features of these materials such as superelasticity and shape memory effect with the capability of SLM fabrication to produce parts with complex geometries which make them very promising for a tremendous number of applications. For medical applications, well-defined guidelines concerning the microstructure of implant material exist, as the structural properties determine the static and dynamic mechanical behavior [78]. It is well-known that the microstructure features such as grain size and average diameter are crucial for toughness, strength, and resistance to crack initiation [78, 102]. It was reported that SLM parameters greatly influence TTs and mechanical response of dense and porous NiTi [76, 77]. Bormann et al. has focused on grain size, shape and texture of SLM NiTi with considering different fabrication parameter as well as scanning strategies and documented the tailorable microstructure via SLM process parameters [78-80]. Effects of process parameters also studied on geometrical characteristics of porous SLM NiTi [81]. For NiTi, it has been reported that 100-200 J/mm3 energy input is required to have dense SLN NiTi fabricated and 195 J/mm3 has been recommended for SLM NiTi [74, 75]. It has been shown that the higher energy samples show higher strength, however the impurity level of SLM NiTi samples is also increased with energy level [74, 75, 77]. Furthermore, it is

displayed that scanning speed and laser power should increase or decrease along with each other to retain the density of the NiTi parts [76].

This section is a very comprehensive and systematic study to improve the understanding of the microstructures formed as the result of the different SLM fabrication parameters. Determining fabrication parameters such as laser power and scanning speed have been investigated individually and the influence of each parameter on transformation temperatures, hardness and texture have studied. Furthermore, the correlation of the thermo-mechanical response and features of the microstructure are discussed. The provided knowledge will allow selection of the right parameters to obtain the best functional features of NiTi alloys fabricated by SLM.

3.1 Fabrication

Dense cylinder samples with 10 mm length and 4.5 mm diameter were fabricated for the mechanical tests with bidirectional scanning strategy. To study the effect of laser power 4 samples were fabricated with 100 up to 250 W power. 1000 mm/s scanning speed, 120 and 30µm hatch spacing and powder layer thickness were used for all samples. Table 3-1 summarizes the parameters and associated energy level of the first batch (A1-4).

Table 3-1 List of SLM fabrication parameters concerning effect of laser power

Number	Laser Power (W)	Scanning Speed (mm/s)	Energy Density (J/mm^3)
A1	100	1000	27.77
A2	150	1000	41.66
A3	200	1000	55.55
A4	250	1000	69.44

The effect of scanning speed was experimentally studied over both low laser power (LLP) of 100 W and high laser power (HLP) of 250 W. The first set of samples was fabricated using LLP and scanning speed altering from 125 to 500 mm/s as given in Table 3-2. This batch will be named B1-4 throughout the text. The second set of samples fabricated by HLP and 875 to 1500 mm/s scanning speed, as shown in Table 3-3, named as C1-4. The hatch spacing and powder layer thickness were kept constant respectively 120 and 30µm for all of the samples. Energy input of the parts was calculated according to equation 1.

Table 3-2 List of SLM fabrication parameters concerning effect of scanning speed

Number	Laser Power (W)	Scanning Speed (mm/s)	Energy Density (J/mm^3)
B1	100	125	222.22
B2	100	175	158.73
B3	100	225	123.45
B4	100	500	55.55
C1	250	875	79.36
C2	250	1000	69.44
C3	250	1250	55.55
C4	250	1500	46.29

Lastly, the influence of hatch spacing was considered and SLM NiTi samples were fabricated with constant 250 W laser power, 1250 mm/s scanning speed, and 30µm powder layer thickness but different hatch spacing varying from 80 up to 180 µm. The energy density was also varied by varying the hatch spacing. This batch of samples will be named **D1-6** throughout the chapter. List of these samples are given in Table 3-3.

Table 3-3 List of SLM fabrication parameters concerning effect of hatch spacing

Number	Laser Power (W)	Scanning Speed (mm/s)	Hatch Spacing (µm)	Energy Density (J/mm^3)
D1	250	1250	80	83.33
D2	250	1250	100	66.66
D3	250	1250	120	55.55
D4	250	1250	140	47.61
D5	250	1250	160	41.66
D6	250	1250	180	37.03

3.2 Microstructure

Figure 3-2 shows optical micrographs of A1-4 fabricate with 100 to 250 W laser power (Table 1). As it can be seen morphology of sample A1 shows a significant number of porosities. The porosity is one of the common defects of SLM samples since the external pressure is not involved and powder solidification is only driven by temperatures changes [103]. Two types of porosity can be observed that are either spherical or irregular. The spherical pores are caused by trapped gas or Ni evaporation. The irregular pores are basically due unstable molten pool or lack of melting [103, 104]. Thus it seems that the energy level as low as 27.77 does not result in a completely dense part. The reduction in porosity of A2 sample is considerable in spite of available irregular shaped porosities. It is evident that as both laser power and energy level were increased the density of samples increases as the A4 sample showed the highest density with the most uniform microstructure.

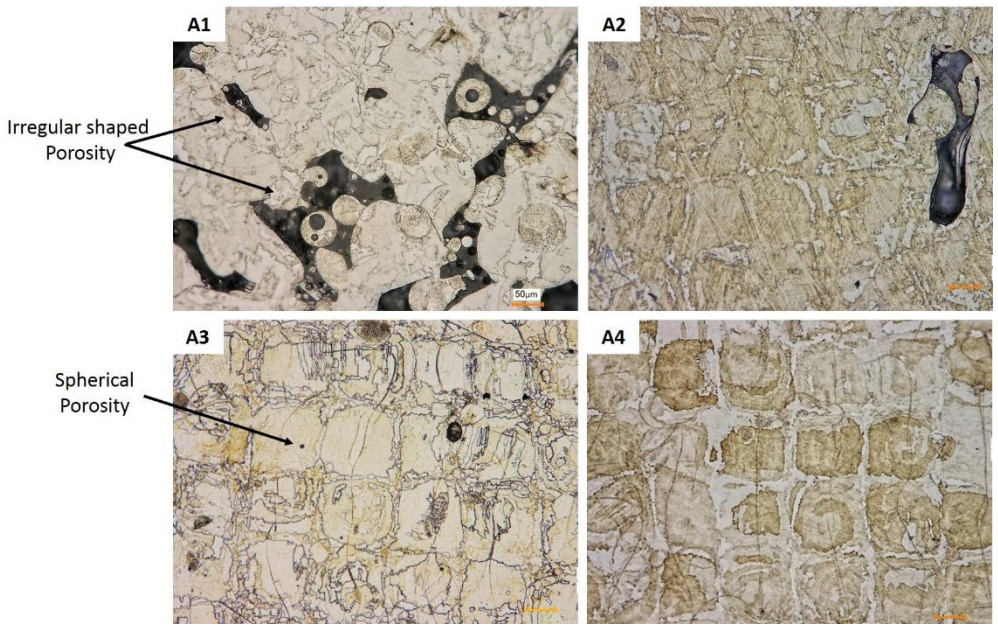

Figure 3-2 Building Direction Optical micrographs of SLM fabricated NiTi with different laser powers, (A1) 100, (A2) 150, (A3) 200, and (A4) 250 W

Optical images of B1-4 samples with LLP but variable scanning speeds of 125, 175, 225, and 500 mm/s can be seen in Figure 3-3. Figure 3-4 is an optical image of C1-4 samples with HLP and variable scanning speeds of 875, 1000, 1250, and 1500 mm/s. Since the physical phenomena occurring during SLM process is similar to welding procedures [78, 90, 105], circular arch-shaped boundaries are seen in microstructure which is melt pools. Formation of these melt pools can be attributed to the Gaussian energy distribution of the laser beam [104]. SLM leads to rapid heating and melting of the powder which is followed by rapid cooling and solidification. The resultant heat transfer affects the size and shape of the melt pool as well as the cooling rate [103]. The geometry of melt pool has a great influence on the grain growth and the microstructure of the part [106]. It has been reported that molten pool structure is not similar to all materials. For instance overlapped molten pool boundaries has been reported as a typical microstructure in a SLM steel [98,

107, 108] or SLM CoCrMo [90] but not in Ti-6Al-7Nb [109], Ti-6Al-4V [110-112], and Fe [91].

Additionally, some small cracks can be found in the microstructure of all samples. The residual and micro thermal stresses due to the high-temperature gradient between the melt pool and surrounding solids and/or compositional segregations are known as responsible for triggering the cracks in SLM metal microstructure. These cracks are very tiny in the higher energy level samples and extended as the scanning speed increases. The extension of cracks is prevented from extension in higher energies due to the rapid cooling [104].

Transformation of grain size and shape is another noticeable fact. From both Figure 3-3 and Figure 3-4, it can be observed that grain sizes are smaller but more anisotropic for batch B (LLP) than batch C (HLP). The similar result has been reported by Bormann et al, regarding the effect of laser power on grain size [78]. The grain size became smaller, more diverse, and more non-uniform in extreme cases of both batches (B4 and C4). This is because, in high laser scanning speed, the lower cooling rate could be obtained. As well known, the lower cooling rate in the solidification process will increase the nucleation rate then leads to small grains [91]. In such cases, irregular pores also started to appear in the microstructure.

Grain shapes also change with alteration of a combination of scanning speed and laser power. The square shaped grain forming a checker microstructure is observed in moderate energy levels of 46.29 to 79.36.J/mm^3 through HLP than 200 W (visible in A3, A4, C1, C2 and C3 samples). Pulled S-shaped grains were formed high energy samples (B1, B2, and B3) samples that had been fabricated with LLP.

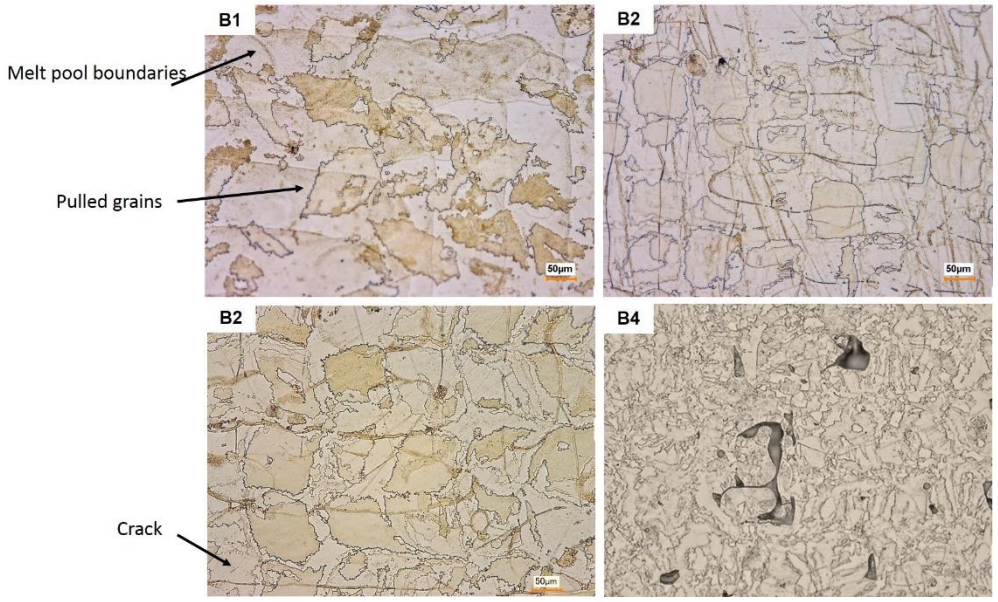

Figure 3-3 Building Direction Optical micrographs of` SLM NiTi fabricated with LLP and different scanning speeds, (B1) 125, (B3) 175, (B4) 225, and (B5) 500 mm/s

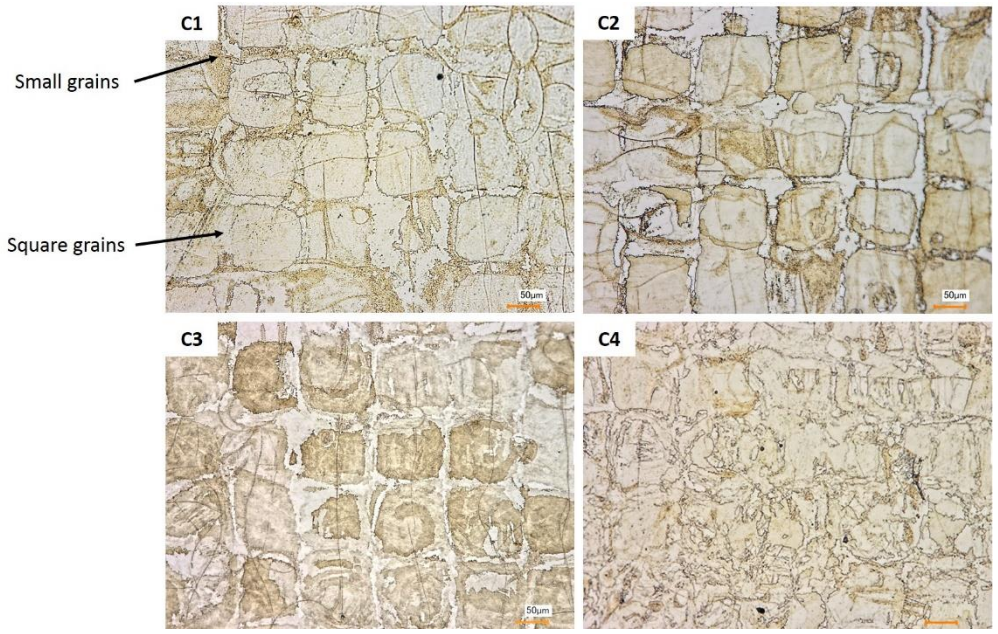

Figure 3-4 Building Direction Optical micrographs of SLM NiTi fabricated with HLP and different scanning speeds, (C1) 875, (C2) 1000, (C3) 1250, (C4) 1500 and mm/s

Figure 3-5 shows the effects of hatch spacing alteration on microstructure. Smaller grains are formed in lower hatch spacing and are enlarge with increasing the hatch spacing. The width of the scan tracks in the building direction is relevant with used hatch spacing

during the fabrication as it is shown in the figure. The fact is true for all D samples except D1. On this particular micrograph, the scanning tack is not visible while more intense melt pool boundaries is seen. The intense melt pool boundaries are influence of the overlapping between two neighboring scan vectors. While these neighboring scanning vectors hardly touch each other when a hatch spacing of 100 µm is used. Therefore, the melt pool width is not influenced significantly by lowering the hatch spacing below 80 µm. As the hatch spacing is increased, a more uniform microstructure is formed but meanwhile number of pores are also increased. Thus, a lower density is expected with higher hatch due to creation of more and larger pores.

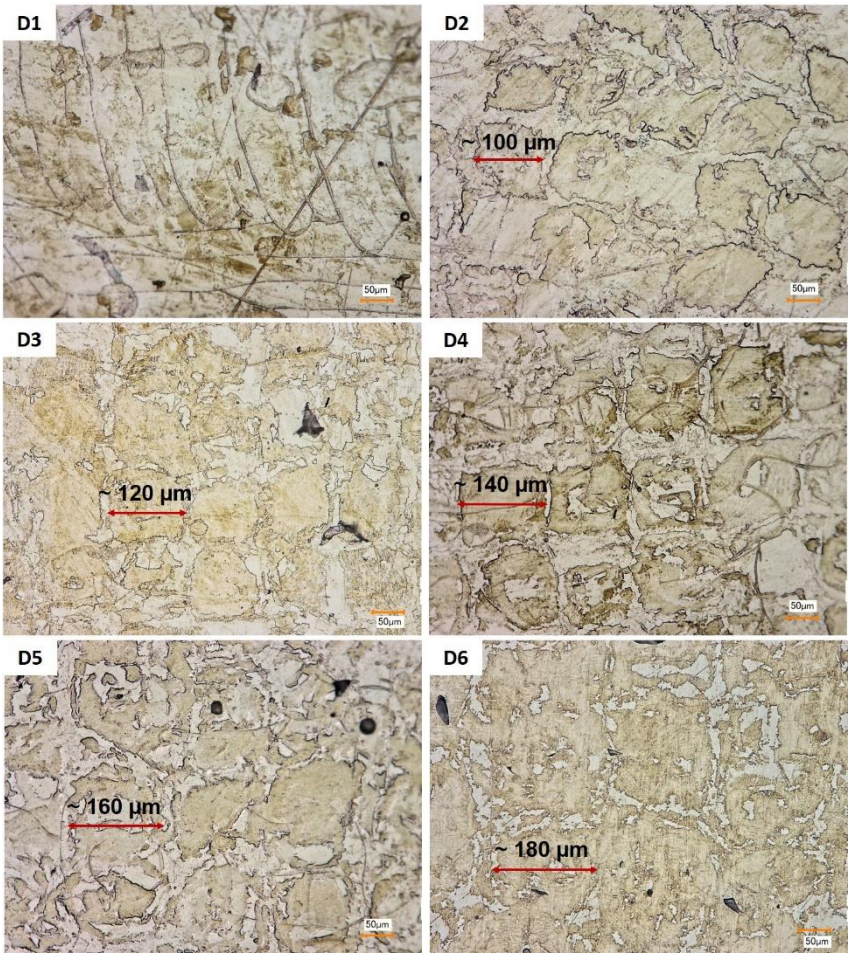

Figure 3-5 Building Direction Optical micrographs of SLM NiTi fabricated with HLP and different hatch spacing of, (D1) 80, (D2) 100, (D3) 120, (D4) 140, (D5) 160, and (D6) 180 µm

3.3 Texture

Figure 3-6 shows the XRD spectra of the two selected samples B3 and C4. Five main peaks were observed in both samples which belong to (110), (200), (211), (220), and (310) orientations. Despite the similar peaks, the intensity ratios of the samples were found to be quite different. The B3 sample showed significantly higher peaks suggesting the formation of a stronger texture in the sample.

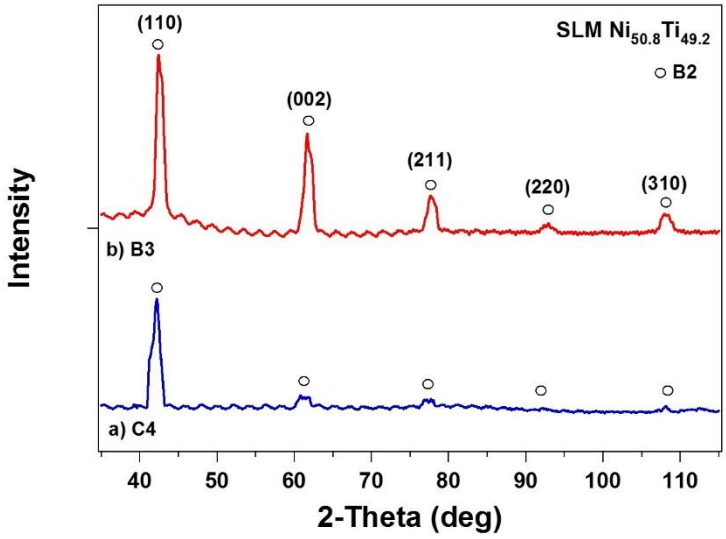

Figure 3-6 XRD spectra for SLM fabricated $Ni_{50.8}Ti_{49.2}$ obtained at RT (a) LE (C5) and (b) HE (B2)

For further detail understanding of the texture pole figures of the sample were studied. Figure 3-7 (a) and (b) are related pole figures of B3 and C4 samples extracted from XRD. A stronger texture can be identified for both samples at [002] direction. The intensity of other directions was almost similar in both cases. As mentioned SLM process and formed melt pool has similarities to welding, therefore grain growth mechanism also shows similarities to welding and grains also tend to grow along the highest temperature gradient within the melt pool. The thermal gradient is generated from the top to lower layers and tends to grow along the direction of the heat flow. In welding technology, the direction of the maximum temperature gradient is always perpendicular to a melt pool boundary [105]. This preferential growth direction for cubic metal and superalloys is [001] [90, 113]. Therefore, after directional solidification at each layer, with epitaxial grain growth, the [001] direction becomes the major direction of the grains after several layers. It should be noted that maximum thermal gradients are commonly oriented along the building direction, however, scanning strategy seems to have a significant influence on these orientations. The

bidirectional (used for current study) or island scanning strategy in which scanning is conducted with a 90° rotation between layers, typically results in [100] texture [103].

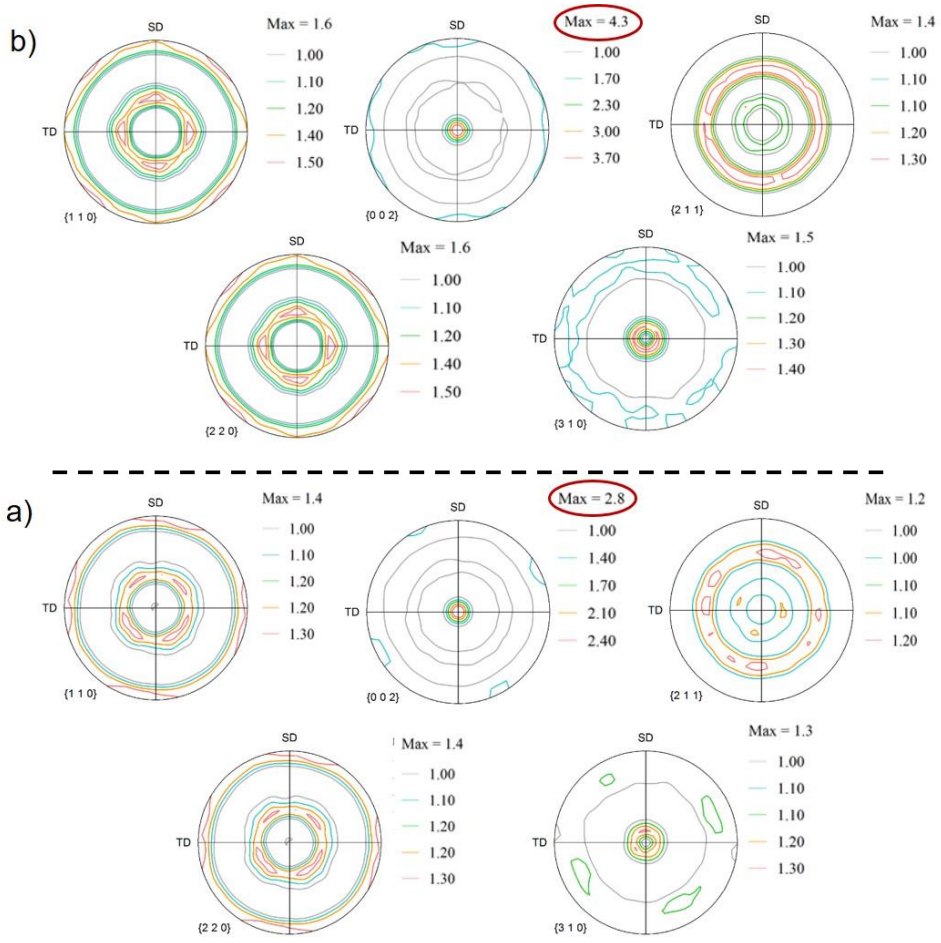

Figure 3-7 Pole figures of SLM $Ni_{50.8}Ti_{49.2}$ in 002, 110, 211, 220 and 310 orientations (a) LE (C5), (b) HE (B2)

Another important observation of Figure 3-7 is the significant difference in intensity of [002] orientation. The intensity of [002] orientation was 2.8 for C4 which was it was increased to 4.3 in B3. The amount of partial re-melting of neighboring tracks is known to be responsible for the extent of the crystallographic texture in SLM fabricated metals [114]. This is in good agreement with presenting results so that with increasing the supplied energy level, the temperature rises, re-melting of previous solid NiTi occurs in

higher amount while existing solid crystals acts as nuclei, and accumulation of oriented grains are increased.

3.4 Transformation Temperatures and Hardness

Figure 3-8 (a) and (b) are demonstrations of A_f and M_s changes as a function of energy level/scanning speed for both LLP (B1-4) and HLP (C1-4) samples. It is clearly observed that TTs are increased as a function of energy level regardless of used laser power. The alteration of TTs of SLM fabricated NiTi correlated to the phenomenon of impurities, created secondary phases, and particularly Ni evaporation [102]. The same scenario seems to be true for energy level alteration in SLM process. The higher supplied energy during SLM fabrication causes the material to be exposed to higher temperatures, which results in greater Ni evaporation and eventually leads to higher TTs despite picked up impurities. Figure 3-8 (a) presents that the rate of TTs alteration is considerably higher in extreme energy levels (more than 120) while it is slow and gradual in lower energy levels can be seen from both Figure 3-8 (a) and (b). These results are in perfect agreement with previous studies [78, 79]. The figure also includes a variation of Vicker hardness as a function of energy level/scanning speed. For B set of samples (LLP fabricated), Vicker hardness was increased with energy level. A similar trend as a function of energy level has been reported for Ti-6Al-4V [101]. As oppose to Figure 3-8 (b), hardness showed a descending trend with energy level. A drastic drop was observed as the energy level of samples were risen to higher than 55.55 J/mm^3. However, the higher energy samples were a mixed phase at room temperature (RT) according to the given TTs curves while lower energy samples were in the austenite phase. Therefore, since all of the hardness measurements were done

in RT such compression might not be genuinely correct.as the hardness of NiTi is complicated and phase dependent [16].

Figure 3-9 shows variation of TTs as a function of hatch spacing. As the hatch spacing is increased the energy level is decreased. Therefore TTs are decreased with increasing the hatch spacing. The similar explanation of scanning speed can be given again that as a higher energy is supplied, the material is exposed to a higher temperatures, which results in greater Ni evaporation and eventually leads to higher TTs. In addition, there is an increasing trend in Vicker hardness of samples as hatch spacing is decreased. The higher microhardness of low hatch spacing samples can be correlated to their higher density and smaller grains. Furthermore, the volume of precipitates is increase if more energy is applied to the material by lowering the hatch spacing or the scanning velocity which could increase the hardness.

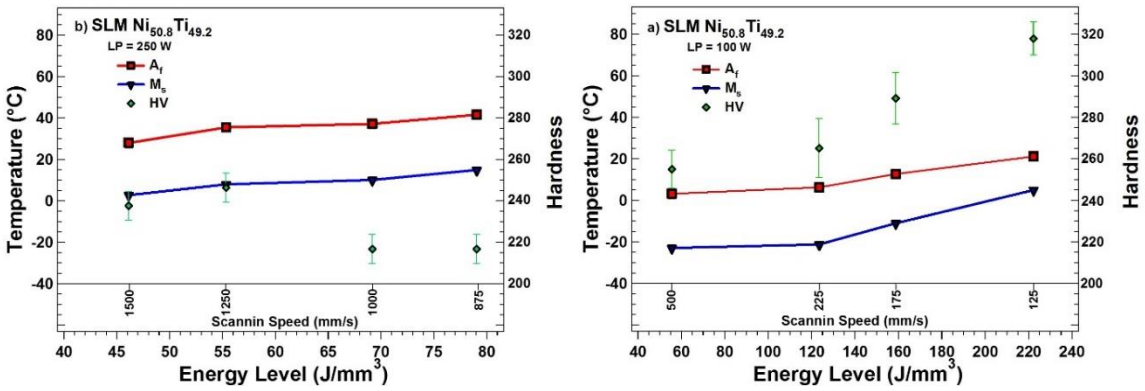

Figure 3-8 The alteration of Vicker hardness, M_s, and A_f temperature as a function of energy level and scanning speed for (a) B1-4, (b) C1-4 samples

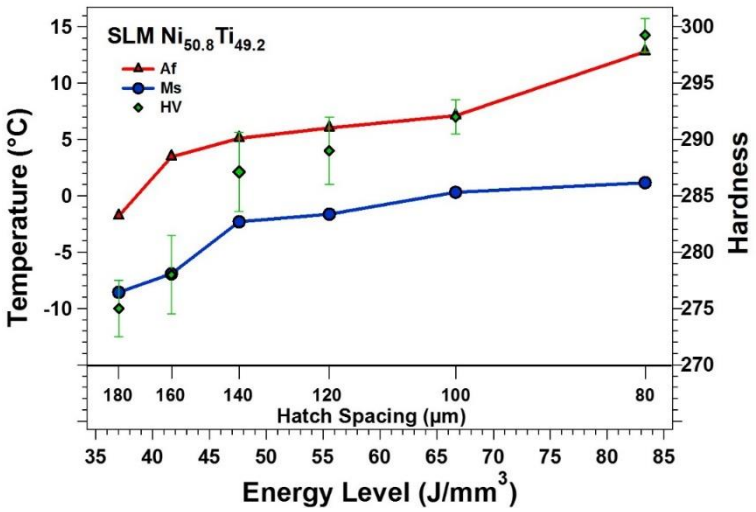

Figure 3-9 The alteration of Vicker hardness, M_s, and A_f temperature as a function of energy level and hatch spacing for D1-6 samples

3.5 Mechanical Response

Figure 3-10 (a) and (b) are mechanical responses of B and C batch at room temperatures. Comparing two batches, it can be seen that the critical stress for transformation in LLP samples is considerably higher than HLP set at room temperature. The recovery ratio also showed a drastic change. The Figure 3-10 (a) indicates that the lowest scanning speed in B batch that results in highest energy level displays the best superelastic response. For batch B a traceable trend was observed that as the energy level of samples was dropped the recovery ratio and critical stress both were decreased. For batch C a certain trend was not observed and the sample C3 with 55.55 J/mm3 showed the highest critical stress and the best strain recovery at room temperature. However, since according to C-C relation the critical stress is temperatures dependent in SMAs and samples have different TTs, one would better to consider the mechanical response at A_f+10 ºC. Figure 3-10 (c) and (d) are the superelastic samples of the same samples at A_f+10ºC temperature. For this experiment, A_f of samples was found after thermal cycling under 25

MPa and then sample's temperature was set to their A_f+10 ºC. As it can be seen, there was no considerable difference in terms of critical stress at this temperature in both B and C batches. The strain recovery, however, was significantly different. In batch B, the highest energy level sample B1 showed the best superelastic response and as the scanning speed increased/energy level decreased, the strain recovery was decreased as well. For batch C, the C1 sample showed better recovery while the C2 showed the least.

The difference in stress hysteresis of two batches was notable as a higher stress hysteresis is evident in batch C. Stress hysteresis is a determinant factor for damping applications. The increased in energy dissipation which is due to lower strength of the material or high interaction between martensite plates leased to higher stress hysteresis in shape memory alloys [16]. Both lower recoverable strain and high mechanical hysteresis indicate the lower strength of batch C samples.

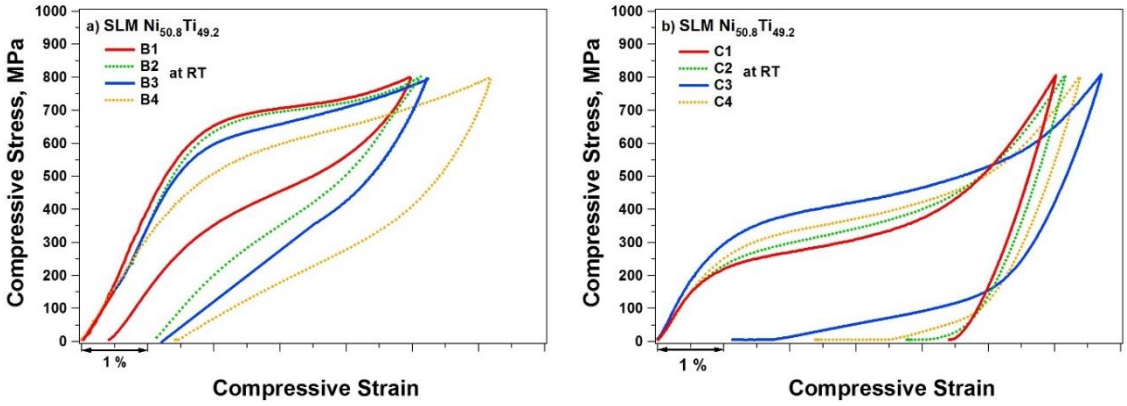

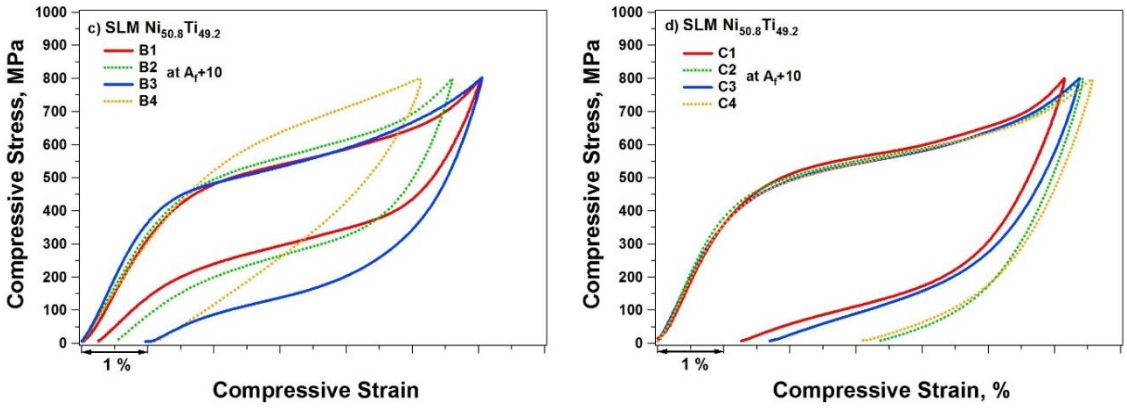

Figure 3-10 Superelastic response of SLM $Ni_{50.8}Ti_{49.2}$ fabricated with different fabrication parameters at (a), (b) room and (c), (d) A_f+10 ºC temperatures

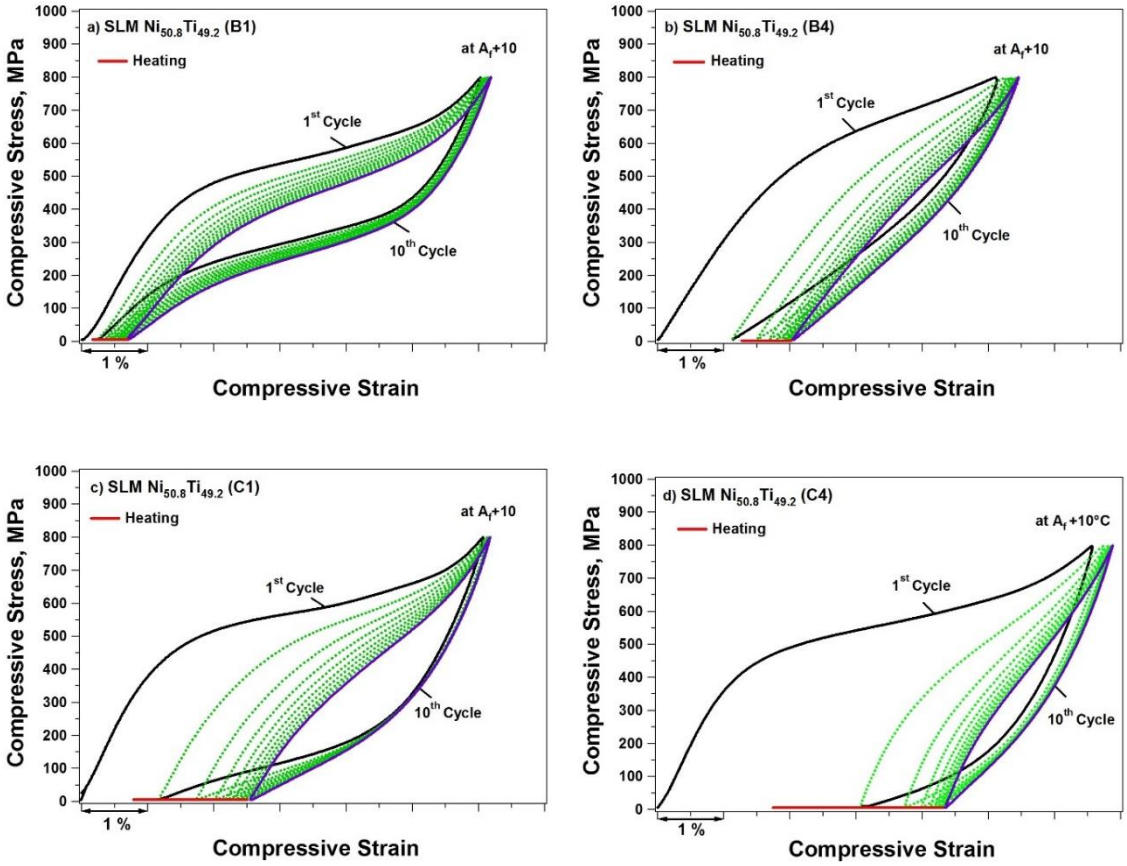

Figure 3-11 Cycling response of selected conditions from Table 3-2 at A_f+10ºC

Figure 3-11 (a)-(d) are cyclic responses of B1, B4, C1, and C4 samples at A_f+10 ºC. For the sake of briefly, only the highest and lowest energy level of batch B and C are

shown, however, the irrecoverable (ε_{irrec}), recoverable (ε_{rec}), and total (ε_{tot}) strain of the first and last cycles were summarized in Table 3-4. Since all the samples were loaded up to the fixed 800 MPa stress, the sample A1 was failed due to highly porous microstructure. The B1 samples showed the highest stabilized superelastic response with 5.5 % strain recovery among all samples. The recovery ratio ($\varepsilon_{rec}/\varepsilon_{tot}$) of the sample at first cycle was calculated to be almost 96%. The poorest response was belonged to sample C2 or A4 with only 48% recovery. The stabilized response was only 2.3 % strain recovery after 10 cycles. All in all samples of the batch B showed higher strength, recoverable strain and better stability.

Table 3-4 Summary of cyclic response of A, B, and C samples at first and last cycle

SLM $Ni_{50.8}Ti_{49.2}$	Max Applied Stress MPa	1st Cycle				10th Cycle	
		ε_{tot} (%)	ε_{Irrec} (%)	ε_{rec} (%)	Recovery Ratio (%)	Total ε_{Irrec} (%)	Stabilized ε_{rec} (%)
A1	800	-	-	-	-	-	-
A2	800	6.12	1.33	4.79	78.26	2.68	3.75
A3	800	6.44	1.22	5.22	81.05	3.57	3.55
A4/C2	800	6.42	3.34	3.08	47.97	4.29	2.29
B1	800	6.02	0.25	**5.77**	**95.84**	0.68	**5.50**
B2	800	5.60	0.54	5.06	90.35	1.40	4.50
B3	800	6.05	0.90	5.15	85.12	3.55	3.06
B4	800	5.11	1.14	3.97	77.69	2.05	3.39
C1	800	6.22	1.34	4.88	78.46	2.71	3.62
C2	800	6.42	3.34	3.08	47.97	4.29	2.29
C3	800	6.37	1.69	4.68	73.46	3.06	3.60
C4	800	6.60	3.12	3.48	52.72	4.34	2.53

Figure 3-12 (a) and (b) are mechanical responses of D batch at room and A_f+10ºC temperatures. The same method was employed during the mechanical testing of D batch except 600 MPa was chosen as the stress limit for minimum the plastic deformation of samples. The Figure 3-12 (a) indicates that the lowest scanning space results in the best superelastic response at room temperature. However, to be able to compare the all features of mechanical response, the superelastic tests conducted at A_f+10 ºC. As it can be seen, there was no considerable difference in terms of critical stresses of D1 to D5, however, a drastic drop was observed in D6 sample. The strain recovery was decreased as the hatch spacing increased. In batch D, the highest energy level sample D1 with lowest hatch spacing showed the best superelastic response at A_f+10 ºC as well.

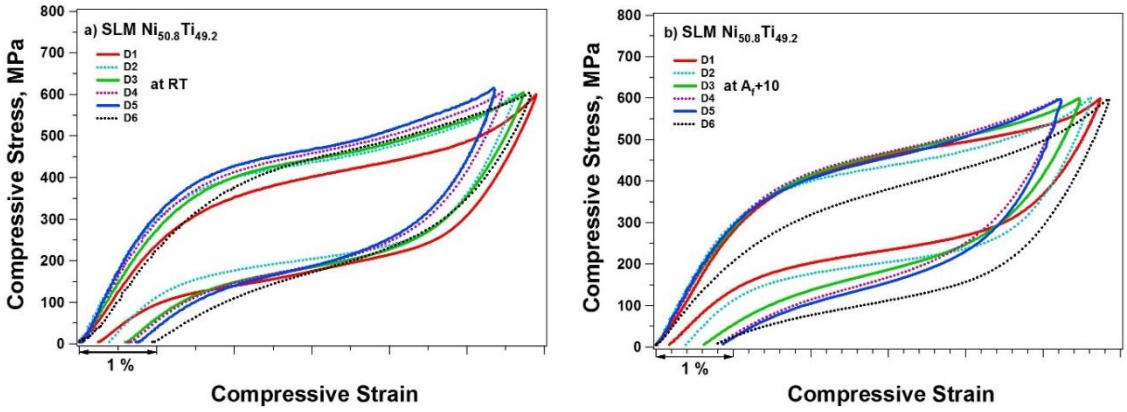

Figure 3-12 Superelastic response of SLM $Ni_{50.8}Ti_{49.2}$ fabricated with different fabrication parameters at (a) room and (b) A_f+10 ºC temperatures

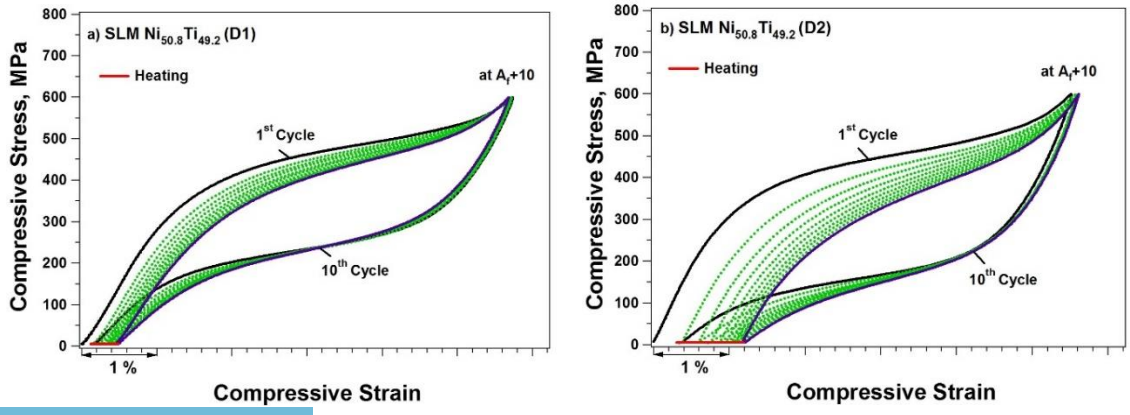

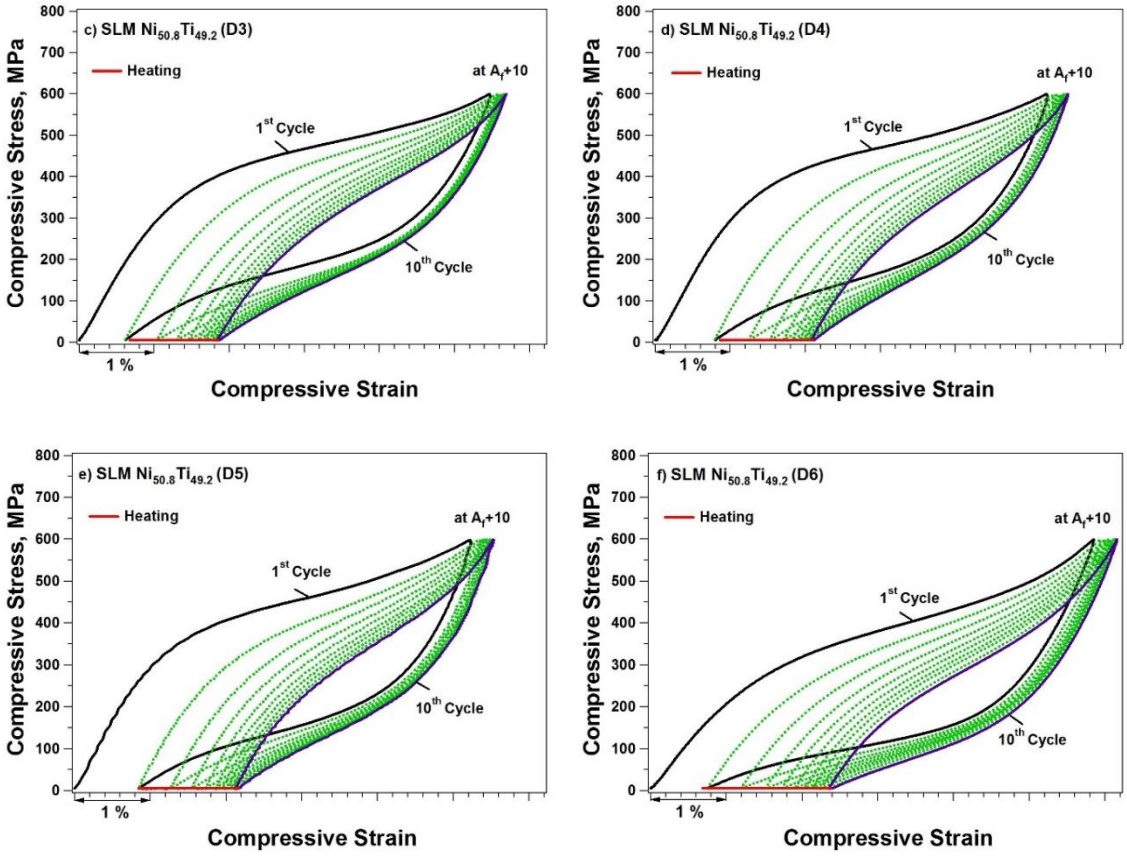

Figure 3-13 Cycling response of selected conditions from Table 3-3 at A_f+10ºC

Figure 3-13 (a)-(f) are cyclic responses of batch D samples at A_f+10 ºC. The ε_{irrec}, ε_{rec}, and ε_{tot} strain of the first and last cycles were summarized in Table 3-5. As expected from previous experiments, D1 showed the highest stabilized superelastic response with 5.2 % strain recovery among all D batch samples. The recovery ratio ($\varepsilon_{rec}/\varepsilon_{tot}$) of the sample at first cycle was calculated to be almost 98%. The poorest response was belonged to sample D5, with 83 % recovery. The stabilized response was only 3.4 % strain recovery after 10 cycles.

Table 3-5 Summary of cyclic response of D samples at first and last cycle

SLM $Ni_{50.8}Ti_{49.2}$	Max Applied Stress MPa	1st Cycle				10th Cycle	
		ε_{tot} (%)	ε_{Irrec} (%)	ε_{rec} (%)	Recovery Ratio (%)	Total ε_{Irrec} (%)	Stabilized ε_{rec} (%)
D1	600	5.72	0.1	5.62	**98**	0.47	5.2
D2	600	5.51	0.38	5.13	93	1.21	4.44
D3	600	5.47	0.62	4.85	88	1.86	3.84
D4	600	5.12	0.8	4.32	84	2.09	3.41
D5	600	5.22	0.87	4.35	83	2.15	3.4
D6	600	5.85	0.77	5.08	86	2.37	379

3.6 Discussion

The Figure 3-14 compares the mechanical response of three samples fabricated with same energy level. However, according to Table 3-1, 3-2 and 3-3, the 55.55 J/mm^3 energy level of these samples have been obtained by employing different laser power and scanning speed. Evidently, each sample demonstrates a distinct shape memory behavior in terms of critical stress, hardening, and hysteresis although the recovered strains were almost equal for all of the three cases. Even, A3 and C3 samples fabricated with very close parameters presented different microstructure features. It is important to note that according to Figure 3-3 and Figure 3-4 while C3 and A3 with 55.55 J/mm^3 energy level showed a dense microstructure B4 with same energy level displayed numerous irregular porosities which mean the energy, in this case, has not been enough to create the stable melt pool. This is also reflected in the B4 sample's poor superelastic response.

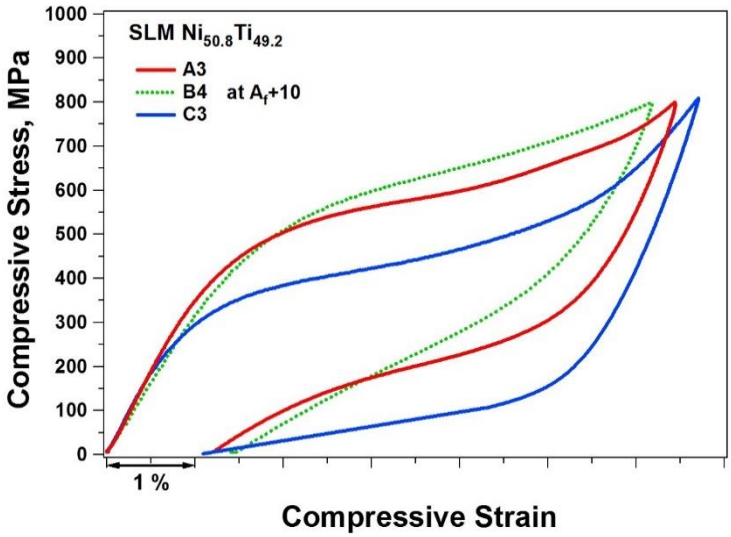

Figure 3-14 Comparison of three different samples fabricated with same energy level obtained through different parameters.

Increasing the laser power was found to have an important role on the densification of the fabricated components. To successfully fabricate fully dense parts either high laser power should be combined with high scanning speed or low laser power with a low scanning speed. This is in good agreement with previously published works [76]. Generally, although using higher scanning speed is advantageous for fast production, but it results in fabrication of lower quality parts [81]. A similar conclusion can be drawn from mechanical results. Lowering the scanning speed for the LLP batch resulted in higher energy density, smaller grain size, higher hardness and eventually better superelastic response. On contrary, increasing the scanning power for HLP samples did not improve the superelastic response. For HLP Hatch spacing turned out to have a substantial impact of mechanical response. Lowering the hatch spacing resulted in higher density, hardness and superelastic recovery ratio. This can be also related to the fact that mechanical response of samples cannot be attributed solely to the density and several other microstructural features such as the geometry of melt pool, size, and shape of formed grain or other defects

like cracks or picked up impurities that are formed during the fabrication, are all involved. Therefore, selection of a set of proper parameters should be in a way that tailors the desired microstructure and prevent the defects. Furthermore, preventing concentration of impurities such as C, O, and Si around the melt pool boundaries that form non-metallic inclusions [7], can greatly improve the mechanical response.

High energy level driven through low laser power and low scanning speed can be suggested for SLM NiTi however, the picked up impurities should be controlled strictly to retain the quality of parts as well as meeting the application requirements. The best mechanical results were obtained in higher energy densities which can be linked to their higher density, hardness, and stronger texture. Yet, excessively high energies may lead to high-temperature gradients, leading to internal stresses or part distortion which consequently increase the risk of balling and dross formation in the melt pool.

It is worth mentioning that samples having the same energy level necessarily do not lead to fabrication of identical parts. Comparing such conditions in terms of microstructure and mechanical response clarified that in SLM fabrication, solely energy level is not sufficient to be considered since fabricated parts with the same energy level that has been obtained through different parameters displayed unalike density level, grain size, shape and consequently mechanical behavior.

The huge difference in superelastic response of samples (about 50 %) clearly shows, how using different SLM process parameters can lead to a different mechanical response. Therefore, to find an optimum process window combination of all involving parameters are required to investigate as the right selection can improve the performance of SLM fabricate NiTi substantially. It should be highlighted that achieved 5.77% strain

recovery in this study has been obtained without going through any thermal treatments, which is a remarkable number for as fabricated $Ni_{50.8}Ti_{49.2}$ alloy and is even higher than the theoretical estimation of recoverable strain in conventionally fabricated [100] single crystal $Ni_{50.8}Ti_{49.2}$.

3.7 Conclusion

Three different batches of $Ni_{50.8}Ti_{49.2}$ alloy fabricated by SLM to study effects of Laser power and scanning speed individually on the superelastic response. The microstructure of fabricated samples was characterized and mechanical response of them experimentally evaluated. The conclusions are as follow:

- The energy level plays an important role on the densification of the SLM fabricated components. To fabricate fully dense parts either high laser power should be combined with high scanning speed or low laser power with a low scanning speed.
- Two types of porosities were observed in the microstructure, i) spherical pores related to trapped gas or Ni evaporation ii) irregular porosities to unmolten or unstable melt pool.
- The employment of different process parameters leads to the formation of different microstructural features, texture, TTs alteration and finally the mechanical response.
- TTs were increased as a function of energy level regardless of the used laser power.
- Higher energy density resulted in re-melting of neighboring tracks and previous solid layer and consequently stronger texture.
- 5.77% superelasticity with more than 95% recovery ratio was obtained in as-fabricated condition for SLM NiTi fabricated by 100 W laser power and 125 mm/s

scanning speed. The same sample showed 5.5 % stabilized strain recovery after 10 cycles. The sample with 250 W laser power and 1500 mm/s scanning speed displayed a poor mechanical response with only 48 % recovery ratio, proving the importance of selecting right process parameters for SLM.

- Decreasing the hatch spacing improved the hardness and superelastic response of HLP samples substantially. When 80 µm hatch spacing employed, 98 % strain recovery was obtained after 600 MPa loading at first cycle which was stabilized after 10^{th} cycle with 5.2 % superelasticity.
- High energy level driven through low laser power and low scanning speed seems the most favorable for SLM fabrication of NiTi in terms of mechanical response.
- The samples with same energy levels but fabricated by different parameters did not show similar behavior which indicates a combination of all involving parameters should be investigated to find the optimum process window for NiTi SLM fabrication.

4 Chapter Four: Comparison of Ni-rich SLM NiTi and the Initial Ingot

The aim of this section is to characterize the thermomechanical behavior of SLM fabricated $Ni_{50.8}Ti_{49.2}$ (atomic %) alloys in as-fabricated and solutionized forms and compare them with the reference ingot. In addition, TTs, the SME, the temperature dependent mechanical response, the critical stress for transformation versus temperature diagram, and the microstructure of the fabricated alloys are presented. All SLM NiTi samples were fabricated with selected process parameters of 250W laser power, 1250 mm/s scanning speed, 120 µm hatch spacing and 30 µm powder layer thickness. Therefore, the supplied energy from laser beam to volumetric of powder was calculated as 55.5 J/mm^3 using the given equation.

4.1 Phase Transformation

Figure 4-1 illustrates the DSC graphs of the initial ingot, and the powder, as-fabricated and solutionized $Ni_{50.8}Ti_{49.2}$ alloys and Table 4-1 shows the TTs extracted from Figure 4-1. The TTs of the ingots are below room temperature, which is in good agreement with the previous results of Ni-rich NiTi [33]. Powder NiTi shows multiple peaks that can be attributed to the compositional inhomogeneity of powders. Phase transformation of the SLM fabricated sample occurs in a broad single step and the TTs increased after the SLM process when compared to the initial ingot.

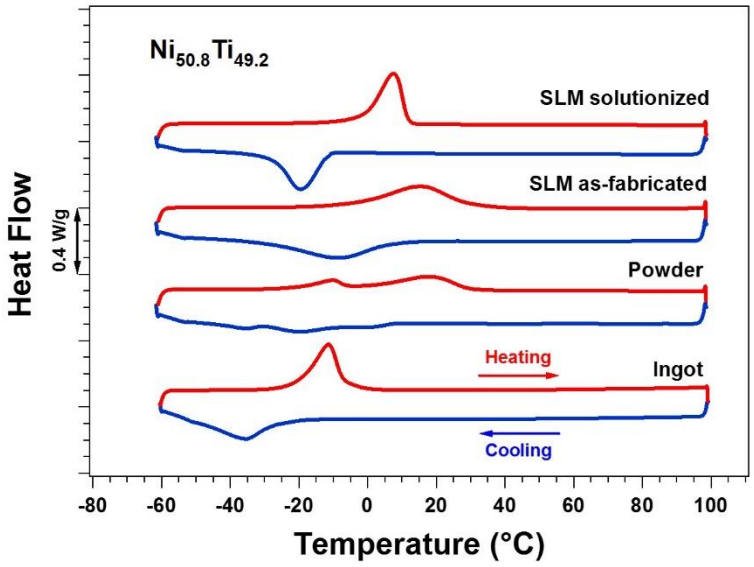

Figure 4-1 DSC responses of the initial ingot, powder, as-fabricated and solutionized $Ni_{50.8}Ti_{49.2}$.

The increase in the TTs is due to two main reasons. The first one is that laser processing is associated with evaporation. Since nickel has lower evaporation temperatures than titanium, the matrix composition shifts to higher titanium content and the temperatures increase [115]. The second reason is that in Ni-rich NiTi, high temperature processing can result in the formation of Ni-rich phases such as Ni_4Ti_3, Ni_3Ti_2, and Ni_3Ti. As a result of the formation of these phases, the matrix composition depletes in nickel. Hence, the matrix composition shifts to higher titanium content and the phase transformation temperatures increase [42].

After solutionizing, the TTs were decreased and the peaks became sharper. The broad peaks of the as-fabricated material can be attributed to the inhomogeneous microstructure of the alloys. During solution annealing, the secondary phases of the as-fabricated samples are dissolved, which results in an increase in the nickel content of the

matrix and homogenous microstructure and thus lower TTs but sharper transformation peaks [31].

Table 4-1 Transformation temperatures of ingot, powder, as-fabricated and solutionized $Ni_{50.8}Ti_{49.2}$.

$Ni_{50.8}Ti_{49.2}$	M_s(˚C)	M_f(˚C)	A_s(˚C)	A_f(˚C)
Initial Ingot	-22.91	-50.00	-20.65	-6.30
As-fabricated	8.66	-29.31	-6.26	30.80
Solutionized	-11.09	-27.27	-6.27	11.77

4.2 Microstructure

In the SLM fabrication process, the microstructure of the fabricated parts depends on the process parameters including powder layer thickness, laser power, scanning velocity, scanning path, distance between the individual laser vectors, size and location of the focus of the laser beam [78, 116, 117]. Figure 4-2 (a) shows the optical micrograph of the $Ni_{50.8}Ti_{49.2}$ alloy ingot. The initial ingot is a mixed phase at room temperature, with a dynamically recrystallized and equiaxed grain structure with average grain size of about 90 µm. Figure 4-2 (b) is the schematic representation of layer by layer SLM process. The figure also depicts the employed bidirectional scanning strategy for fabrication of current study. Figure 4-2 (c) and (d) are the microstructures of SLM fabricated samples from the building direction (BD) and perpendicular to building direction (PBD). SLM sample has checker grain along the BD and columnar structure along the PBD that reflects the scanning path.

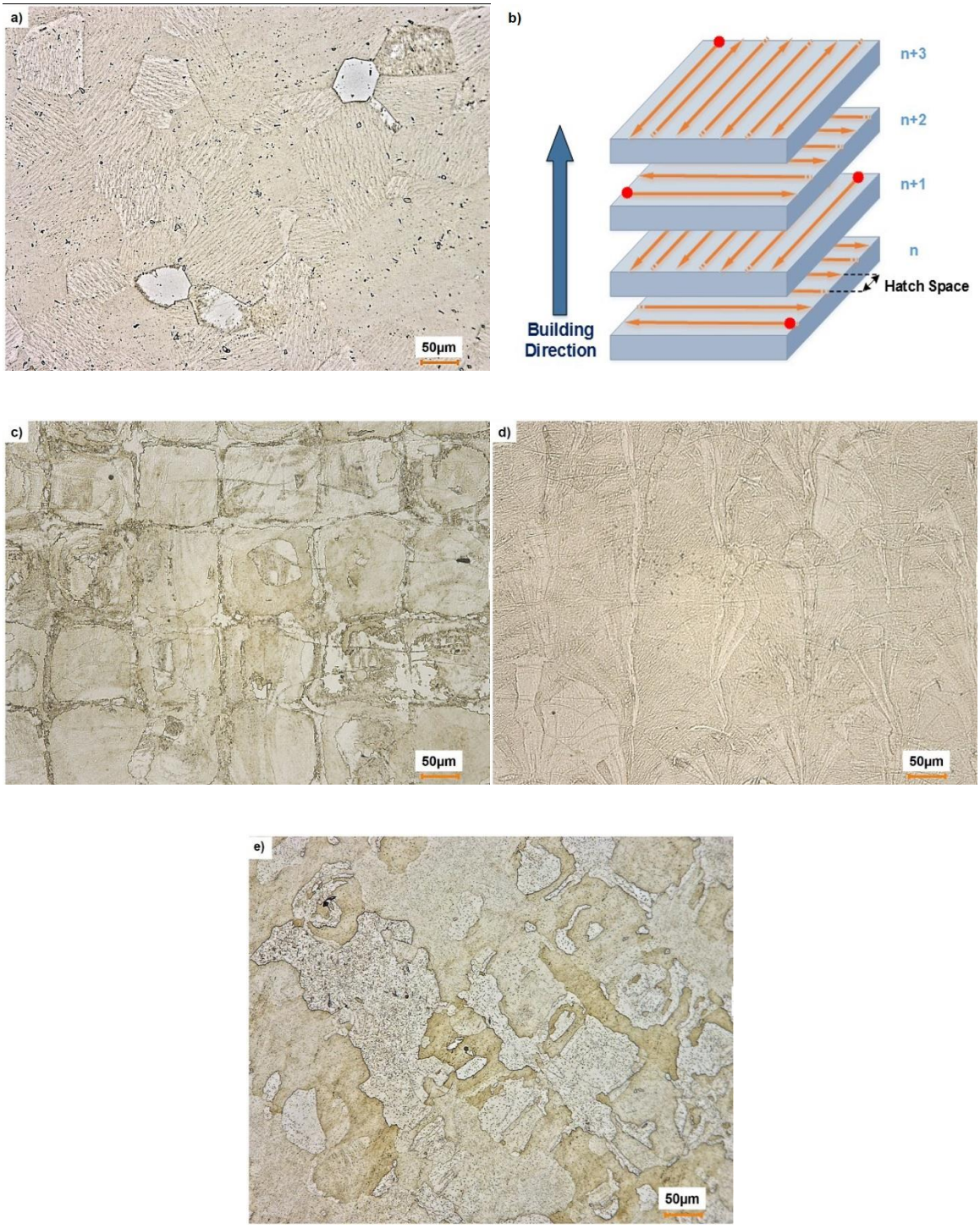

Figure 4-2 Optical micrographs of $Ni_{50.8}Ti_{49.2}$ in (**a**) the initial ingot, (b) schematic of SLM fabrication and scanning strategy (the red dots show the start points of laser track in each layer), (**c**) the BD, (d) the PBD of SLM fabricated, (e) Solutionized SLM

The microstructural features such as grain size, orientation of grains, precipitates, impurities, second phases, porosity or surface effects have a significant effective on shape memory properties. It is known that the grain size and average grain diameter in metals is crucial for toughness, strength and resistance to crack initiation [118]. The grain shapes in the initial ingot material are diverse and inhomogeneous while uniform rectangular shaped grains are formed after the SLM process. The average grain size was about 90 μm in initial ingot. After the SLM process, the size of newly formed square shape grains is relevant with the scanning line space, also known as hatch spacing, and about 100 to 140 μm. In addition, the formation of other small, slim and diverse grains along the large square grain boundaries is visible from morphology.

The rectangular arrangement of grains for as-fabricated SLM materials reflects the scanning path of the laser during the process. Solution annealing substantially increased the grain size and also dissolved the second phases or smaller grains on the rectangular boundaries of the as-fabricated sample.

4.3 Thermal Cycling under Stress

Figure 4-3 (a)–(c) show the thermal cycling under constant compressive stress of the initial ingot, as-fabricated and solutionized NiTi samples. At every cycle, the stress was isothermally applied at a temperature above A_f. The sample was then thermally cycled between this temperature and temperature below M_f while the applied compressive stress was kept constant. After one complete thermal cycle, the stress level was incremented for the next thermal cycle until the maximum transformation strain was obtained. It is worth noting that TTs increased with stress. For the ingot, M_s increased from −7 °C to 2 °C and A_f increased from 0 °C to 30 °C when the stress was increased from 50 to 300 MPa.

The M_s and A_f temperatures of the as-fabricated alloy were 13 °C and 37 °C under 50 MPa and increased to 26 °C and 54 °C under 300 MP a, respectively. In the solution annealed sample the M_s and A_f temperatures under 50 MPa were −8 °C and 12 °C and increased to 18 °C and 47 °C under 400 MPa, respectively.

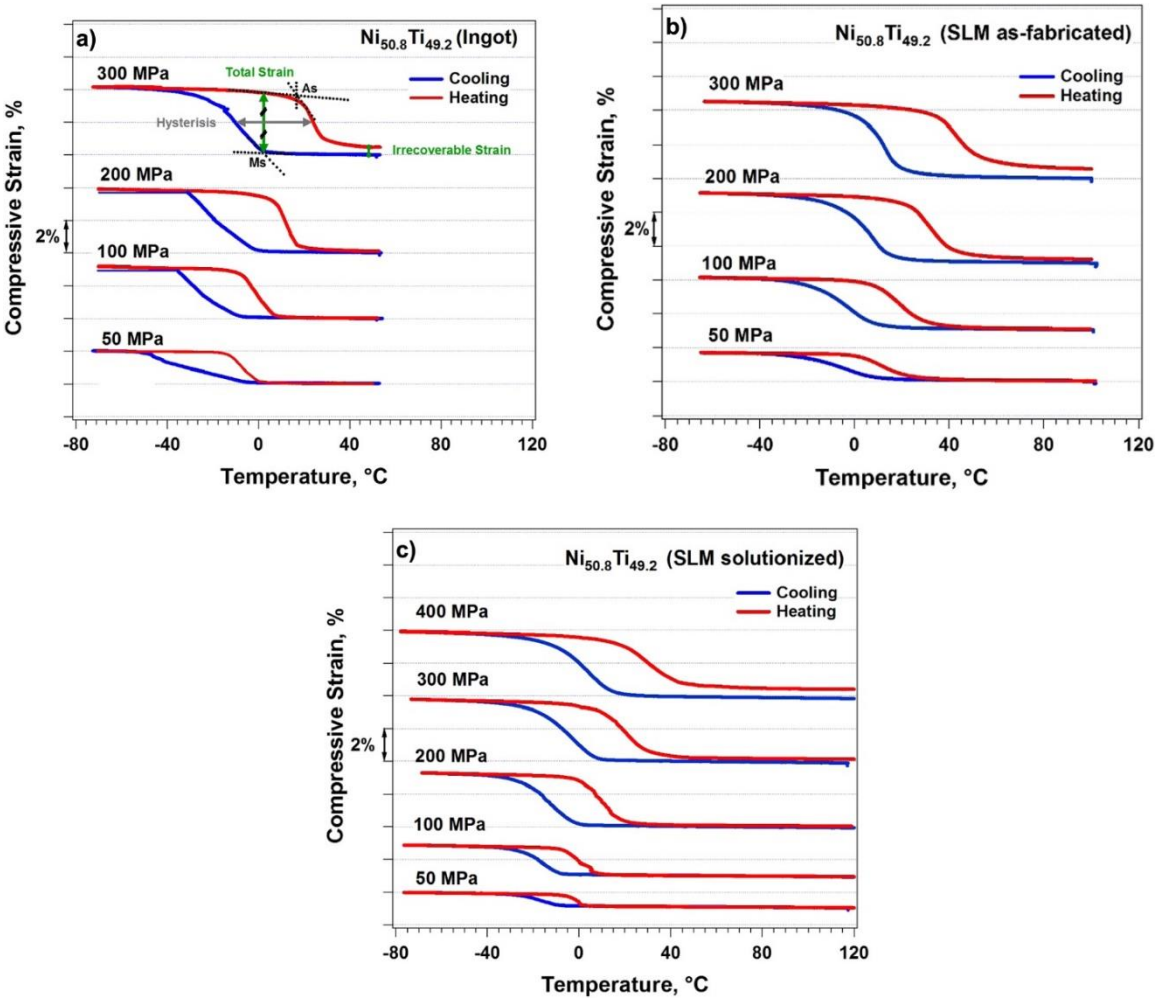

Figure 4-3 Thermal cycling under constant stress of (a) the initial ingot, (b) the as-fabricated SLM, and (c) the SLM solutionized $Ni_{50.8}Ti_{49.2}$ alloys

It should be noted there are small differences between the TTs obtained from DSC and MTS tests, which can be attributed to several reasons. (i) DSC tests are conducted in a fully enclosed environment with a small amount of material (~20 mg) while thermal cycling at MTS has been done by conduction heating on a large sample (~3 g). (ii) In

mechanical tests, only the change in sample length due to the formation of reoriented martensite variants can be measured. Thus, particularly at lower stress levels (e.g. 5 or 50 MPa), the phase transformation may start earlier than what can be detected by thermal cycling under stress experiments by the formation of self-accommodating martensite. (iii) The intersection methods, which is used to determine the TTs, can result in errors, depending on the shape of the curves.

The total and irrecoverable strains are measured between the tangents of the cooling and heating curves at M_s and A_f, respectively, and hysteresis is measured between these tangent lines at the midpoint of the transformation strain. The recoverable strain is calculated as the difference between the total and irrecoverable strains. Figure 4-4 (a) illustrates the temperature hysteresis and Figure 4-4 (b) shows the recoverable and irrecoverable strains as a function of applied stress. The hysteresis and strains of the as-fabricated sample are very similar to the ones from the ingot. It is clear that hysteresis increases with applied stress for both samples. The recoverable strains of the initial ingot and the as-fabricated samples have increased from 1.84% and 1.45% at 50 MPa to 3.26% and 3.47% at 300 MPa, respectively. The irrecoverable strain is almost negligible up to 100 MPa and reaches about 0.5% under 300 MPa for both samples. The temperature hysteresis of the solutionized sample is narrower than that of the others, which is in good agreement with the DSC results. For the solution annealed SLM sample, the recoverable strain was 0.67% under 50 MPa and increased to 2.93% under 300 MPa. Thus, solution annealing has increased the strength, resulting in an almost fully recoverable shape memory effect up to 200 MPa for solutionized SLM $Ni_{50.8}Ti_{49.2}$. The irrecoverable strain of all three tested conditions started to increase after 200 MPa. Under 300 MPa

the irrecoverable strain for both intial ingot and the as-fabricated samples is about 0.5% while for the solutionized sample it is 0.2%. The maximum work output of the initial ingot and as-fabricated SLM samples was about 10 J cm^{-3} under 300 MPa while the work output of the solution annealed SLM sample was found to be 12 J cm^{-3} under 400 MPa.

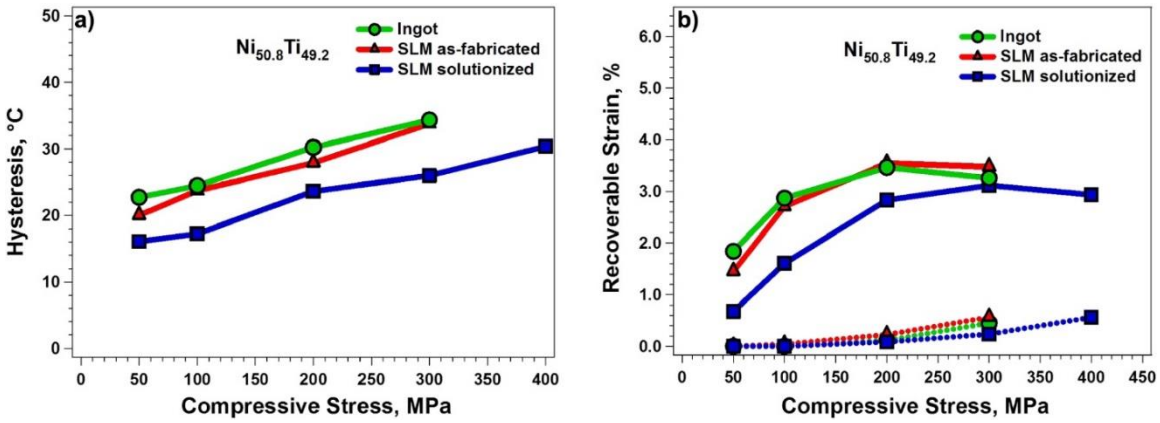

Figure 4-4 (a) The temperature hysteresis, and (b) recoverable (solid line) and irrecoverable (dashed line) strain of the initial ingot, the as-fabricated and the solutionized $Ni_{50.8}Ti_{49.2}$ alloys as function of applied stress.

4.4 Stress–Strain Responses

Figure 4-5 (a)–(c) show the temperature dependent stress–strain responses of the initial ingot, the as-fabricated and the solution annealed SLM $Ni_{50.8}Ti_{49.2}$ alloys. For each experiment, M_s was determined from the thermal cycling under 5 MPa results and the first testing temperature was selected as M_s + 10 °C. Then, the testing temperatures were increased with 10 °C increments. The specimen was loaded up to 3% strain and then unloaded, followed by heating to a temperature beyond A_f. The same procedure was repeated as the testing temperature was increased by 10 °C after every step. The initial ingot showed almost full recovery with a negligible residual strain at 2 °C that was recovered by subsequent heating. Superelastic testing at higher temperatures and subsequent heating resulted in a small amount of irrecoverable strain due to plastic

deformation. Meanwhile for the as-fabricated sample, only partial superelasticity was observed at all selected temperatures. The remnant strain upon unloading was recovered after heating at temperatures below 27 °C. At higher temperatures, irrecoverable strain was observed even after heating the samples to above A_f. At 37 °C, recoverable strain was 2.6% during unloading and 0.6% upon heating, when the irrecoverable strain was 0.2%. After solution annealing, the SLM $Ni_{50.8}Ti_{49.2}$ alloy showed almost perfect superelasticity between −5 °C and 15 °C.

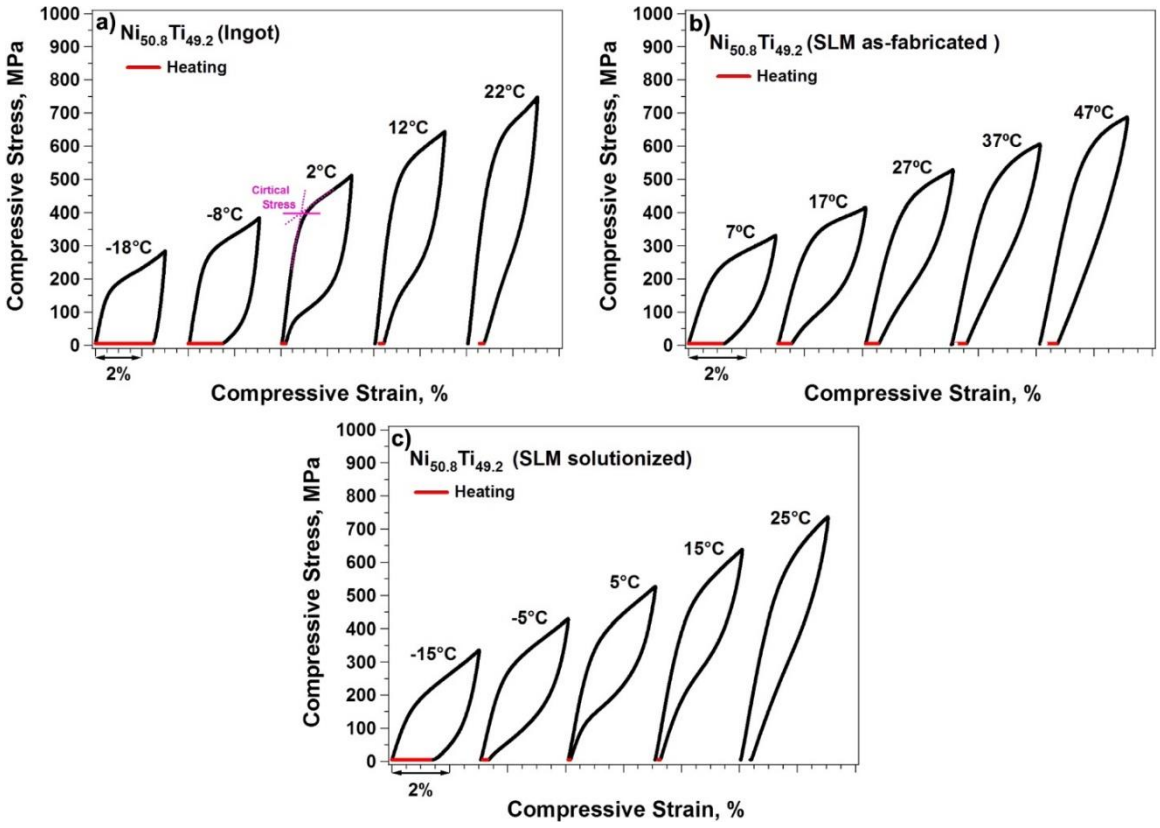

Figure 4-5 The stress versus strain responses of (a) the initial ingot, (b) the as-fabricated and (c) the solutionized $Ni_{50.8}Ti_{49.2}$ alloys.

The tangent method, as shown in figure 5(a), was used to graphically determine the critical stress for martensitic transformations as a function of temperature. Figure 4-6 depicts the change in critical stress for martensitic transformations with

temperature. It is evident that the critical stresses increase linearly with temperature, which is governed by the CC relation. The CC slope for the initial ingot was determined to be 11.5 MPa C^{-1}, which dropped to 8.4 MPa C^{-1} after the SLM process. The CC slope of the SLM fabricated alloy increases to 10.6 MPa C^{-1} after solution annealing. The CC slopes for equiatomic NiTi polycrystalline alloys has been reported to be about 12 MPa C^{-1} in compression[119].

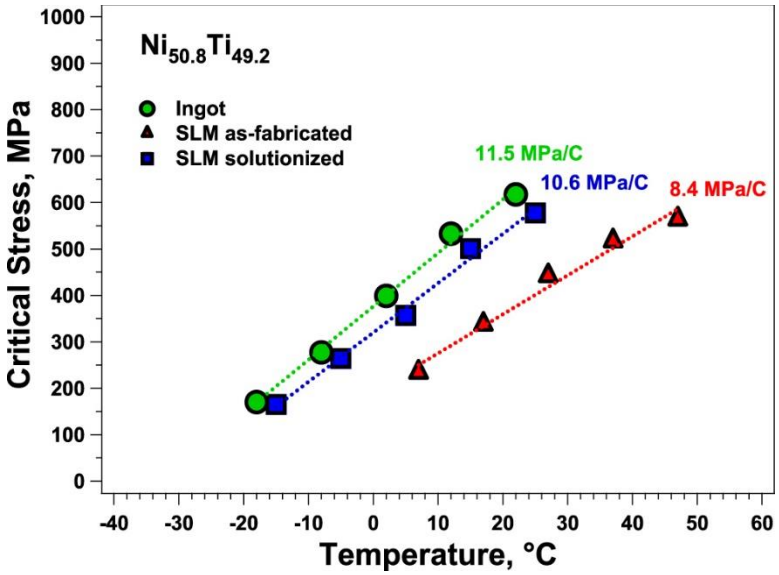

Figure 4-6 The critical stress versus the temperature of the initial ingot, the as-fabricated and the solutionized $Ni_{50.8}Ti_{49.2}$ alloys under compression

4.5 Discussion

As shown in Figure 4-5 (b), the as-fabricated sample showed only partial superelasticity while the initial ingot showed better superelasticity than the as-fabricated sample. This can be attributed to the formation of second phases along the grain boundaries and increased grain size after SLM. It is well known that the strength of materials decreases with grain size. Furthermore, the formation of soft second phases along the grain boundaries could result in plastic deformation and alter the composition of the matrix. It

should be kept in mind that in Ni-rich NiTi alloys, the strength of the alloy increases with Ni content. Thus, formation of Ni-rich second phases could result in decreased matrix strength. The strength of the SLM fabricated $Ni_{50.8}Ti_{49.2}$ alloy can be improved by aging with precipitation hardening. The effects of aging on the SLM fabricated $Ni_{50.8}Ti_{49.2}$ alloy will be revealed in detail in another study. The solutionized sample also shows better superelasticity than the as-fabricated alloy despite its larger grain size. This can be attributed to the fact that second phases, formed along the grain boundaries in the as-fabricated sample, are dissolved by solutionization and new precipitates are formed inside the grains. According to Figure 4-6, at each temperature the critical stress for the solutionized sample is higher than that of the as-fabricated and close to critical stress of the ingot. Thus, the phase transformation occurs at higher stress levels in solutionized and ingot samples which could result in more plastic deformation. However, due to their higher strength, they result in better superelastic response.

4.6 Summary and Conclusion

The shape memory behavior of as-fabricated and solution annealed $Ni_{50.8}Ti_{49.2}$ alloys fabricated using the selective laser melting (SLM) technique. Results were compared to the initial ingot that was used to fabricate powders. Optical microscopy was employed to reveal the microstructure. The shape memory effect under constant compressive stress and isothermal compressive stress cycling tests were utilized to investigate the shape memory characteristics of the initial ingot and fabricated alloys. It was revealed that the SLM method and post heat treatments can be used to tailor the microstructure and shape memory response. The main conclusions are:

- SLM process created checker and columnar grain structure reflecting the scanning strategy. The size of newly formed grains is related to the scanning line space.
- As-fabricated $Ni_{50.8}Ti_{49.2}$ shows good shape memory behavior and partial superelasticity without any post treatment.
- Solutionized SLM $Ni_{50.8}Ti_{49..2}$ demonstrated up to 3% recovery and 0.2% irrecoverable strains, while the as-fabricated SLM sample showed 3.4% recovery and 0.5% irrecoverable strains under 300 MPa.
- The as-fabricated sample shows partial superelasticity while the solutionized sample and the initial ingot show fully reversible superelasticity at 3% strain. Solutionizing the fabricated samples increased the strength and improved the superelasticity but slightly decreased the recoverable strain.

5 Chapter Five: The Influence of Heat Treatments on Solutionized Ni-rich SLM NiTi Alloy

As mentioned, equiatomic NiTi alloys do not show promising superelasticity due to their low strength [28] while Ni-rich NiTi alloys are more likely to show superelasticity since they have a higher intrinsic strength and can be precipitation hardened. Heat treatment is one of the most effective methods in order to control transformation temperatures (TTs) and increase the strength of Ni-rich NiTi alloys by the formation of Ni_4Ti_3, Ni_3Ti_2, and Ni_3Ti precipitates [27, 38]. The precipitation characteristics and the corresponding shape memory properties highly depend on aging temperature, aging time, cooling rate a nd alloying [27, 41-43]. So far, very few studies have focused on the superelasticity of SLM fabricated NiTi alloys where Haberland [75] has reported about 4% superelastic strain recovery for the SLM fabricated $Ni_{50.7}Ti_{49.3}$ alloys after aging. This chapter provides a systematic approach to employ proper aging time and temperature over solutionized samples to tailor transformation temperatures and improve hardness, shape memory effect, and particularly superelasticity.

5.1 Phase Transformation

Figure 5-1 (a) and (b) depict the DSC responses of solutionized SLM $Ni_{50.8}Ti_{49.2}$ alloys after thermal treatments at 350 °C and 450 °C, respectively. Heat treatment time was varied from 5 min up to 18 h. For comparison, the DSC responses of the ingot, as-fabricated and solutionized samples were also included. Figure 5-1 (a), it can be observed that the as-fabricated sample has higher TTs and broader peaks when it is compared to the ingot, which can be attributed to two main reasons. First, laser processing is associated with the evaporation of nickel during the process since nickel has a lower

evaporation temperature than titanium. Secondly, in Ni-rich NiTi, high-temperature processing can result in the formation of Ni-rich secondary phases. As a result of the formation of these secondary phases and/or evaporation of nickel, the matrix composition depletes in nickel. Hence, the matrix composition shifts to higher titanium content and the TTs increase [73, 120].

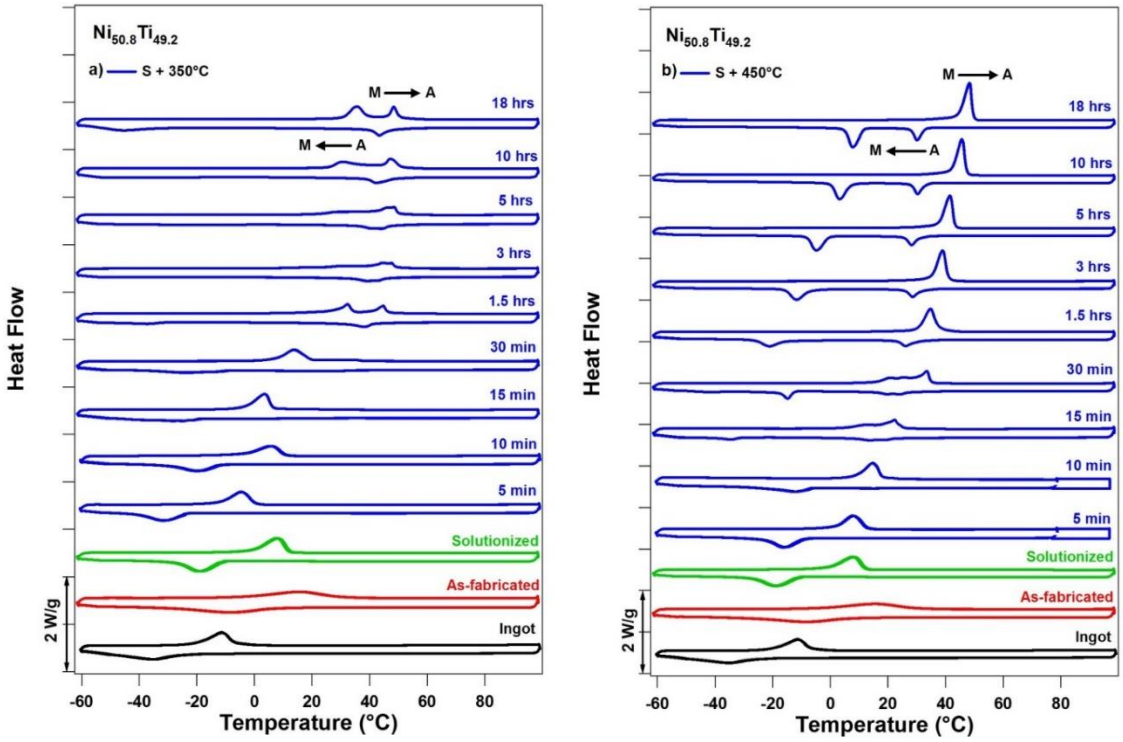

Figure 5-1 DSC response of solutionized SLM $Ni_{50.8}Ti_{49.2}$ alloys aged at (a) 350 °C, (b) 450 °C as a function of aging time

Figure 5-1 (a) also compares phase transformation behavior of as-fabricated sample to the solutionized. Evidently, TTs have decreased by about 20 °C and peaks are sharpened after solutionizing which can be attributed to the fact that the formed secondary phases through SLM process are dissolved, and a more homogeneous and nickel-rich matrix is created. As a result, the transformation temperatures decrease due to Ni-rich matrix and the peaks become sharper due to the homogenous microstructure.

Another visible trend in Figure 5-1 (a) is the increase of TTs with aging time. Similar to conventional Ni-rich NiTi, with post processing aging, the solubility of Ni increases with temperature which leads to the formation of Ni-rich precipitates. The newly formed precipitates deplete the Ni-content of the matrix and eventually increase the transformation temperatures. For heat treatments longer than 30 min, double transformation peaks were observed during cooling where the first peak can be attributed to austenite to R-phase transformation and the second peak can be attributed to R-phase to martensite transformation. R-phase formation after formation of Ni_4Ti_3 precipitates in NiTi alloys has been well documented [121-124]. Multiple step transformation can be clarified by three main arguments for conventional NiTi alloys which are also valid about SLM NiTi: i) formation of coherent stress fields around precipitates, ii) evolving Ni-concentration profiles between the particles and iii) differences in nucleation barriers between R-phase and martensite [123, 124].

For solutionized and 450 °C aged samples (Figure 5-1 (b)), phase transformation peaks are quite sharp and distinct. R-phase started to appear after only 15 min of aging. In 450 °C aged samples, R-phase can be clearly observed during the forward transformation upon cooling. The reverse transformation from martensite to austenite is completed through a single sharp peak. In comparison, R-phase transformation in Figure 5-1(a) appears as a shoulder during the reverse transformation of samples.

5.2 Thermal Cycling under Stress

Figure 5-2 depicts thermal cycling under constant load for solutionized and then 18 h aged sample at 350 °C. Under low load levels, austenite transforms to R-phase first and then to B19′ martensite which results in large temperature window for forward

transformation. Upon heating B19′ martensite transforms back to R-phase and then to austenite in a small temperature window. As a result of different temperature hysteresis between R-phase and B19′ martensite transformations, a triangular shape transformation can be observed. This behavior is in good agreement with the DSC results where double peaks during cooling and heating can be observed. R_s and M_s were 42 °C and −40 °C, respectively, under 50 MPa. As stress was increased, austenite to R-phase transformation was disappeared and symmetric behavior was observed during thermal cycling. It is notable that R-phase transformation is stable and R_s does not change with stress while M_s increases linearly with stress. Thus, after certain stress level, $M_s$becomes higher than R_s and R-phase transformation disappears. M_s was increased up to 62 °C under 500 MPa and single step transformation was observed. Figure 5-2 also demonstrates the thermal cycling responses of the solutionized sample at selected stress levels for comparison. TTs for solutionized sample are lower than aged sample which are in good agreement with DSC results. It should also be noted that irrecoverable strain was started to occur at 400 MPa for the solutionized sample while aged sample shows almost full recovery even under 500 MPa. Thus, we can conclude that aged sample has higher strength than the solutionized sample.

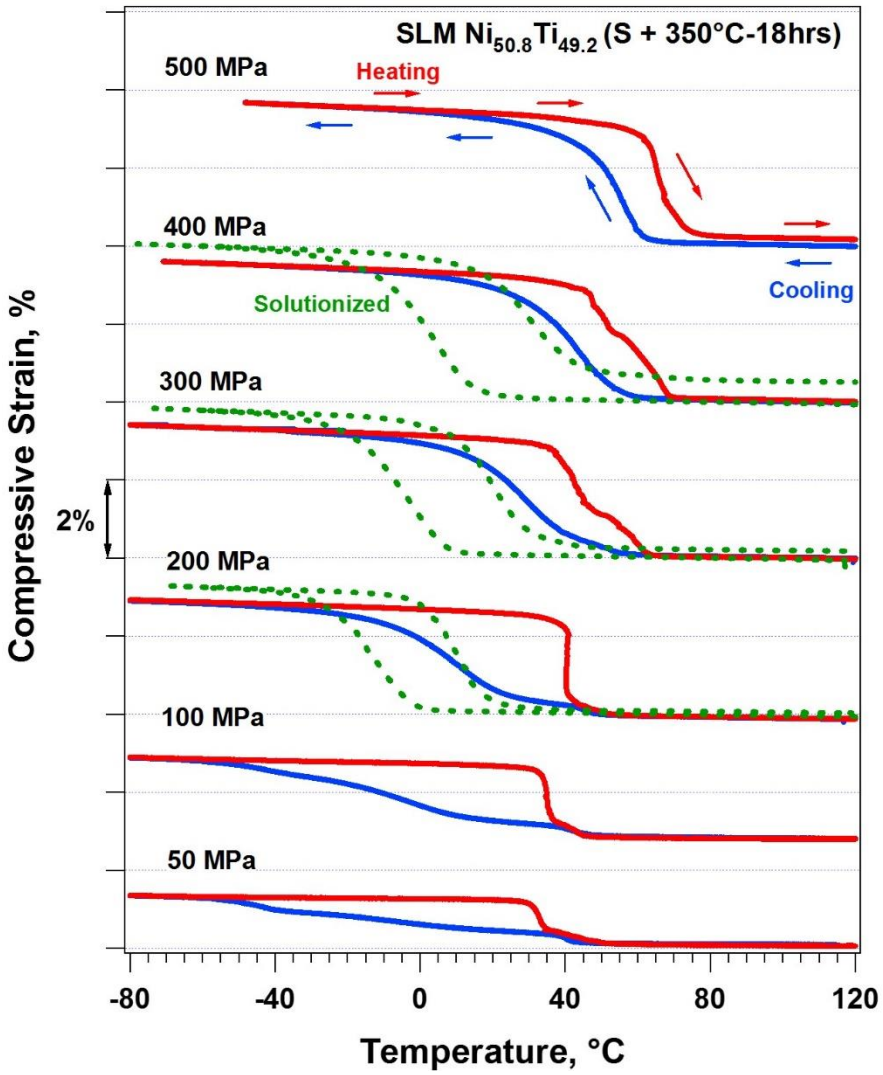

Figure 5-2 Thermal cycling under constant stress of solutionized and 18 h aged at 350 °C SLM $Ni_{50.8}Ti_{49.2}$

5.3 Hardness

Figure 5-3 compares the Vicker's hardness of ingot, as-fabricated, solutionized and aged samples at room temperature. Since all the hardness tests were conducted at room temperature, samples can be in different phases. The hardness of NiTi alloys is highly temperature dependent due to phase transformation where stress-induced austenite to martensite (or R-phase) transformation or variant reorientation could occur during the hardness test [16]. Vicker hardness value of the as-fabricated NiTi shows a drastic decrease

when it is compared to the ingot. Solutionizing increased the hardness of as-fabricated sample to the level of ingot's hardness. The hardness of aged samples increased with aging time and 350 °C aged samples have a higher hardness than 450 °C aged samples.

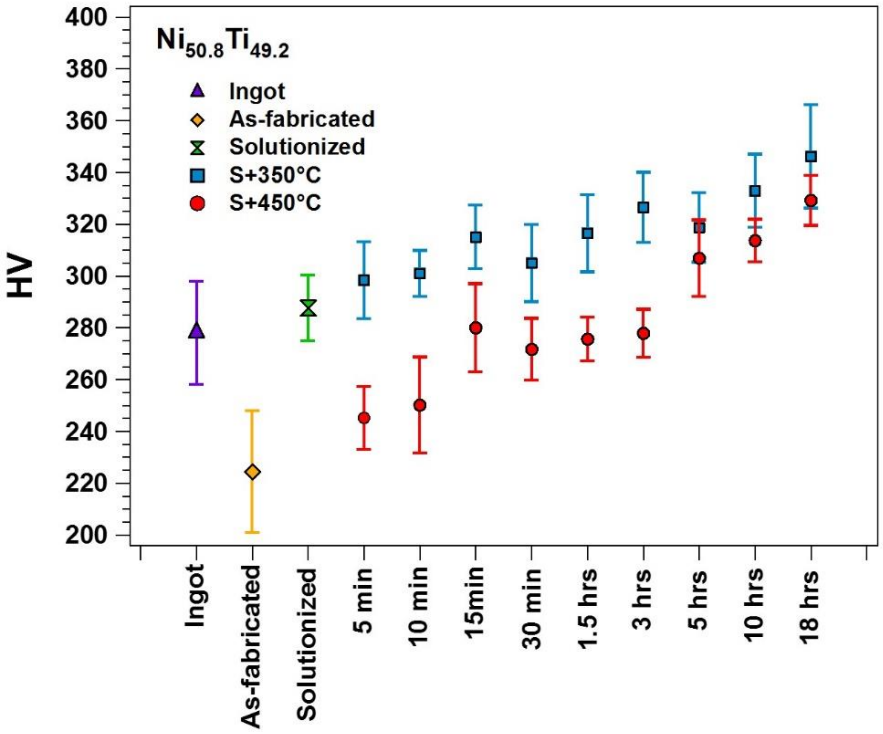

Figure 5-3 Vicker hardness of SLM $Ni_{50.8}Ti_{49.2}$ as function of aging conditions.

5.4 Stress-Strain Curves

Since higher hardness values were obtained for longer time aged samples, their mechanical responses were characterized. Samples aged for 5, 10 and 18 h at both 350 °C and 450 °C were compressed at their A_f+15 °C and the results are shown in Figure 5-4 (a) The mechanical results of as-fabricated and solutionized samples were added for comparison. Testing temperature was 70 °C for as-fabricated and 27 °C for solutionized samples. The testing temperatures (A_f+15 °C) of aged samples were between 65 and 67 °C. All the samples were loaded up to about 2000 MPa (limit of MTS Landmark system) and

then unloaded. The first plateau during loading corresponds to stress-induced martensitic transformation while the second plateau is associated with plastic deformation. It is obvious that the mechanical behavior can be strongly influenced by aging conditions. Formation of precipitates strengthens the material and increases critical stress for plastic deformation [125-127]. There was no superelastic recovery observed in as-fabricated and solutionized samples while partial recovery was observed in 350 °C aged samples. The recoverable strain was increased with aging time since precipitation hardening increased the critical stress for plastic deformation. Compared to as-fabricated and solutionized samples, plastic deformation of aged samples was quite small. The samples aged at 450 °C showed high irreversible strains than the samples aged at 350 °C. Figure 5-4 (b) shows the critical stresses for stress-induced martensitic transformation and plastic deformation. The increase of critical stress for plastic deformation after aging is clear. With increasing of aging time, critical stress for plastic deformation does not significantly change for both aging temperatures. For stress induced martensitic transformation, duration of aging on 350 °C is more effective than 450 °C. The required stress for stress-induced martensitic transformation in 350 °C aged samples is approximately 100 MPa higher than 450 °C aged samples.

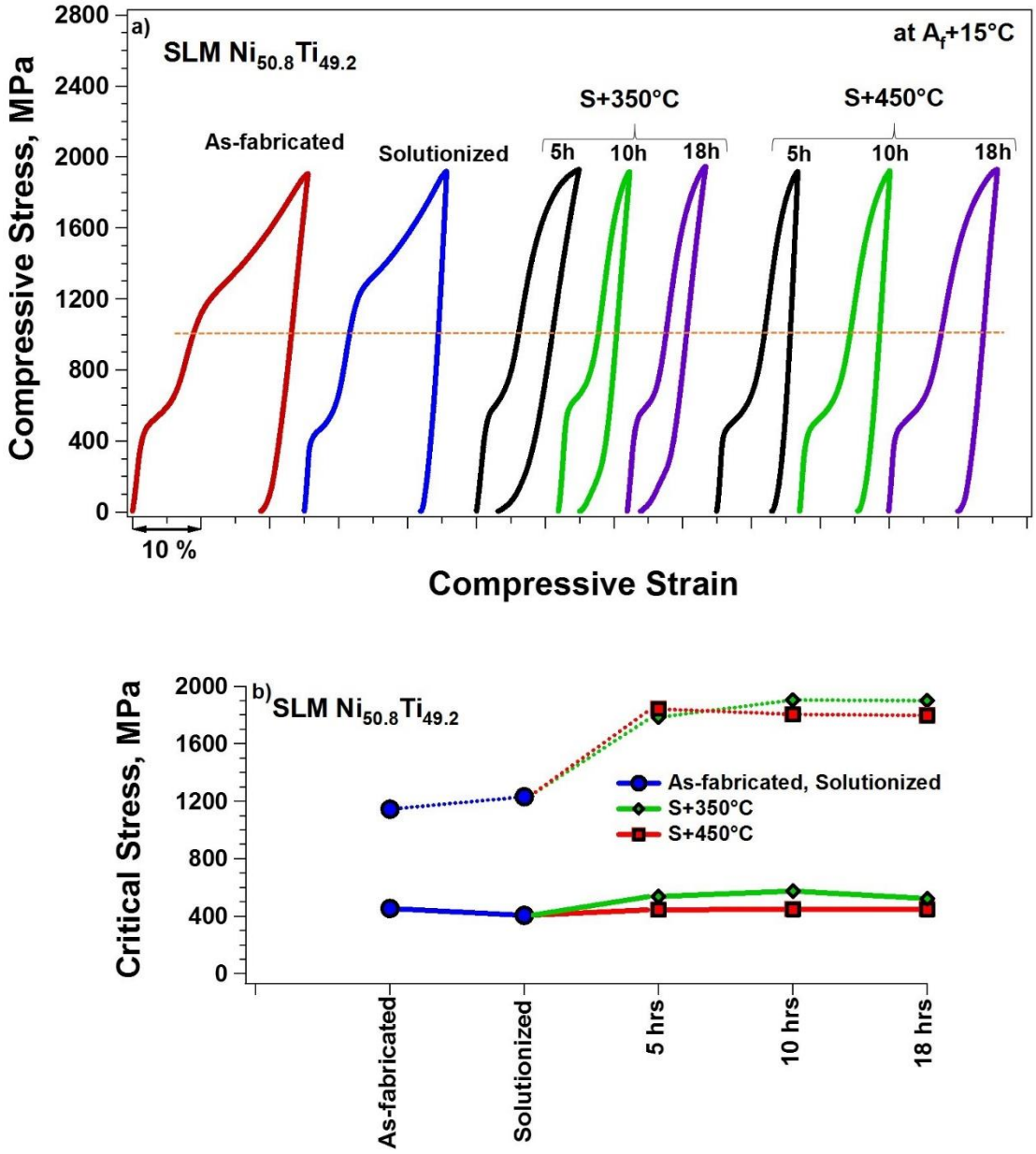

Figure 5-4 (a) Stress-Strain curve (comparison) for as-fabricated, solution annealed and aged samples, (b) Critical stress for stress-induced martensitic transformation (solid line) and plastic transformation (dashed line with aging time).

5.5 Superelasticity

For superelastic experiments, samples were loaded up to 1000 MPa before reaching the critical stress for plastic deformation and then unloaded at their A_f+15 °C. It is obvious from Figure 5-5 (a) that 350 °C aged SLM $Ni_{50.8}Ti_{49.2}$ showed fully reversible

superelasticity while 450 °C aged samples showed only partial superelasticity. Recoverable and irrecoverable strains of the samples are shown in Figure 5-5 (b). Irrecoverable strain for 450 °C aged samples is quite high while it is negligible for samples aged at 350 °C which is in good agreement with the hardness results shown in Figure 5-3. For 450 °C aged samples, recoverable and irrecoverable strains are almost equal after aging for 5 and 18 h. 450 °C-10 h aged sample showed slightly higher recovery than the other 450 °C aged samples. Although all the samples aged at 350 °C demonstrated almost perfect superelasticity, the 350 °C-18h aged sample had the highest recoverable (5.5%) and lowest irrecoverable (0.3%) strains. Improved superelasticity can be ascribed to the precipitation hardening due to the formation of Ni_4Ti_3 particles [54]. When these particles are coherent and small, they increase the strength of the material. It should be noted that aging temperature and time determine the precipitation characteristics. The size of the particles increases and interparticle distance decreases with aging time while volume fraction of the particles decreases with aging temperature [17, 128, 129]. Thus, 450 °C aging might have been resulted in lower volume fraction but bigger size and larger interparticle distance of particles which result in lower hardening effect and strength. As a result, diminished recovery during the superelasticity of 450 °C aged samples was observed.

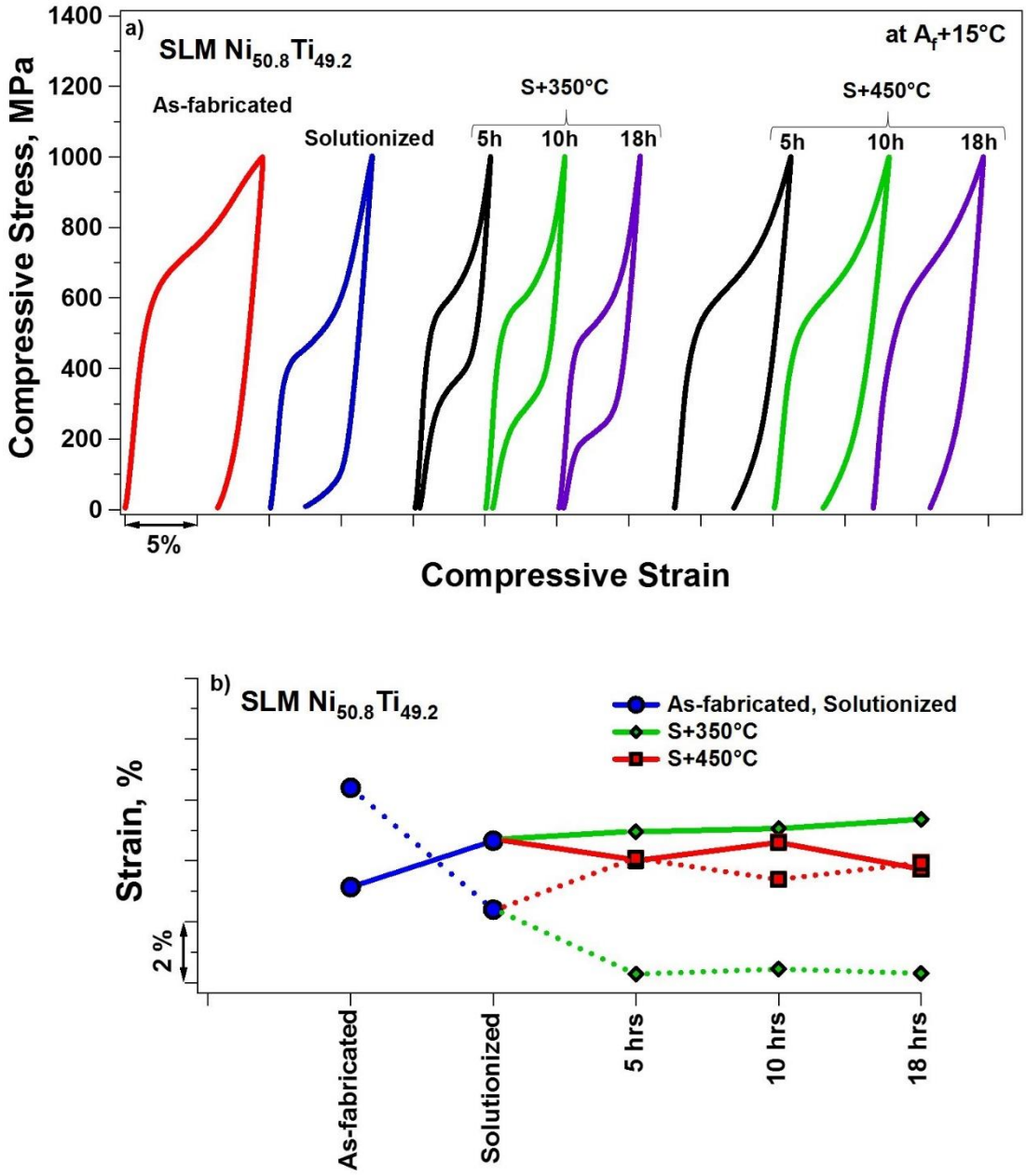

Figure 5-5 (a) Superelasticity of as-fabricated, solution annealed and aged samples, (b) Recoverable (solid line) and irrecoverable (dashed line) strains as function of aging condition.

5.6 Cyclic Response

To investigate the stability of superelastic response of the sample, cycling tests were conducted. Based on superelastic test results shown in Figure 5-5, two samples that are

aged at 350 °C for 18 h and 450 °C for 10 h were chosen for the cycling tests since they showed the highest recoverable strains. Cycling tests were also conducted on as-fabricated and solutionized for comparison. Figure 5-6 depicts the superelastic cycling results of as-fabricated, solutionized, 350 °C-18 h aged and 450 °C-10 h aged samples. Table 5-1 lists the total and recoverable strains of the samples for the first and tenth cycles. The as-fabricated sample showed a recoverable strain of only 2.6%, while solutionized sample showed the recoverable strain of 3.4% in the 10th cycle. As expected, the 350 °C-18 h aged sample showed better, stabilized superelasticity with a recoverable strain of 4.2% after 10th cycle while 450 °C-10 h aged sample showed a recoverable strain of 3.8%. The total irrecoverable strain after 10 cycles is 7.6% for as-fabricated sample and 5.6% after solution annealing. 450 °C-10 h aging did not improve the superelastic response significantly where it shows a similar response to the solutionized sample with 4.55% of total irrecoverable strain after 10 cycles while 350 °C-18 h aged sample shows a major improvement where the total irrecoverable strain of the sample after 10 cycles is only 2.5%. From Figure 5-6, it can be seen that all of the samples have broad stress hysteresis with pronounced plateaus in the first cycle. As the number of cycles was increased, the hysteresis decreased, plateaus become barely noticeable and the response stabilized. The highest irrecoverable strain was observed in the first cycle. The increased irrecoverable strain with cycling is due to the formation of microstructural defects, retained martensite variants, and plastic deformation.

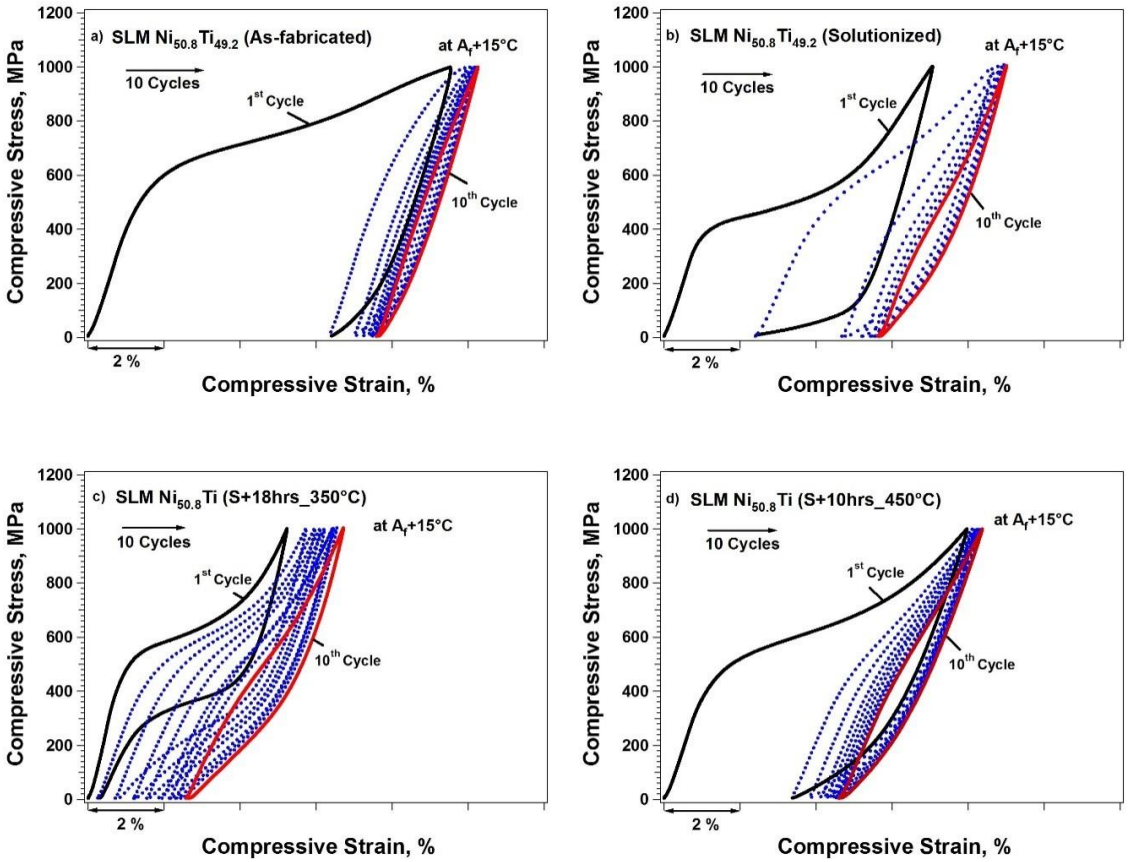

Figure 5-6 Superelastic cycling of SLM $Ni_{50.8}Ti_{49.2}$, (a) As-fabricated, (b) Solutionized, (c) Solutionized plus 18 h aged at 350 °C, (d) Solutionized plus 10 h aged at 450 °C.

Table 5-1 Total and recoverable strain at first and last cycles

	1st Cycle			10th Cycle	Total
SLM $Ni_{50.8}Ti_{49.2}$	Recoverable strain (%)	Total strain (%)	Recoverable / Total Strain (%)	Recoverable strain (%)	Irrecoverable Strain after 10 cycles (%)
As-fabricated	3.14	9.54	32.9	2.64	7.625
Solutionized	4.66	7.07	65.9	3.41	5.625
S+18 h_350°C	5.50	5.80	94.8	4.18	2.50
S+10 h_450°C	5.50	8.00	68.7	3.8	4.55

5.7 Discussion

The difference between the testing and transformation temperatures, and strength are the most important factors in observing superelasticity. In this study, we have demonstrated that they can be controlled through heat treatments. For instance, the yield strength of the samples can be increased from 1200 MPa to 1800 MPa and A_f can be adjusted from 0 to 50 °C by selecting the suitable heat treatment. Since transformation temperatures were increased with aging time, low time aging is suggested to observe superelasticity at room or body temperatures.

According to presented results after aging at 350 °C for 18 h, SLM fabricated $Ni_{50.8}Ti_{49.2}$could display superelasticity with 5.5% recoverable strain, 95% recovery ratio, at first, cycle and 4.2% stable recoverable strain after 10 cycles. It should be kept in mind that additive manufacturing could be employed to fabricate complex dense or porous structures. It even allows engineering the porosity characteristics where structures with the desired level of stiffness, pore size and morphology can be fabricated. Thus, these structures can be solutionized and aged to demonstrate superelasticity without the need for further processing. The possibility of adjusting the fabrication and heat treatment parameters to tailor the shape memory responses of NiTi provides novel opportunities in applications such as the ability to fabricate patient-specific parts in the biomedical industry.

5.8 Summary and Conclusion

Effects of solution annealing and subsequent aging on shape memory response of Ni-rich $Ni_{50.8}Ti_{49.2}$ alloys fabricated by Selective Laser Melting was experimentally studied. After solutionizing, samples were heat treated at selected times at 350 °C and 450 °C and their shape memory effect, superelasticity, and transformation temperatures were

determined. It has been concluded that aging is an effective method to tailor the shape memory properties and obtain superelasticity of SLM fabricated Ni-rich NiTi alloys since transformation temperatures, transformation behavior, strength, and recoverable strain are highly heat treatment dependent. Main conclusions are:

- R-phase transformation was observed during the thermally cycling of 350 °C-18 h aged sample under constant stress. The "triangle type" behavior for shape memory effect was detected below 300 MPa while the behavior was symmetric at higher stress.
- The strength of the fabricated alloys increased after heat treatments. Whereas 450 °C aged samples did not show promising superelasticity, 350 °C aged samples showed almost perfect superelasticity with 95% recovery ratio.
- 350 °C-18 h aging displayed 5.5% strain recovery and only 0.3% irrecoverable strain at first cycle under 1000 MPa loading at 65ºC.
- Superelastic responses of the samples were stabilized after cycling tests. Stress hysteresis, recoverable, and irrecoverable strains were decreased with number of cycles. 350 °C-18 h and 450 °C-10 h aged samples demonstrated stable recoverable superelastic strains of 4.2% and 3.8%, respectively, at the 10th superelastic cycle.

6 Chapter Six: Effects of Texture Formation and Aging on as-fabricated Ni-rich SLM NiTi

In this chapter, a systematic aging study (without prior solution annealing) is carried out to reveal the transformation behavior of SLM NiTi parts. In our previous work, a comprehensive aging study has been done on solution annealed SLM $Ni_{50.8}Ti_{49.2}$ [130]. The process of solutionizing, however, is challenging and might be accompanied by undesirable outcomes such as melting and oxidation. Lastly, the thermal cycling under stress and superelastic response of the selected aging conditions at room and body temperatures are determined and results are linked to the microstructure and texture analysis.

6.1 Texture

Figure 6-1 shows the XRD spectra of the ingot and SLM samples. Five main peaks were observed in the ingot and SLM samples. The largest peak, at 2Θ=42.8°, is from the (110) orientation while the other peaks at 61.9°, 78.1°, 93.3°, and 108.7° are from the (200), (211), (220), and (310) orientations, respectively. In both the ingot and SLM sample, B19′ is present besides B2. The change in the intensity ratios of the ingot and SLM samples suggests the formation of a different texture in the SLM fabricated samples. Since, the texture of materials highly depends on their fabrication method, and mechanical and shape memory properties are highly texture dependent, thus, it is important to investigate the texture of SLM fabricated samples.

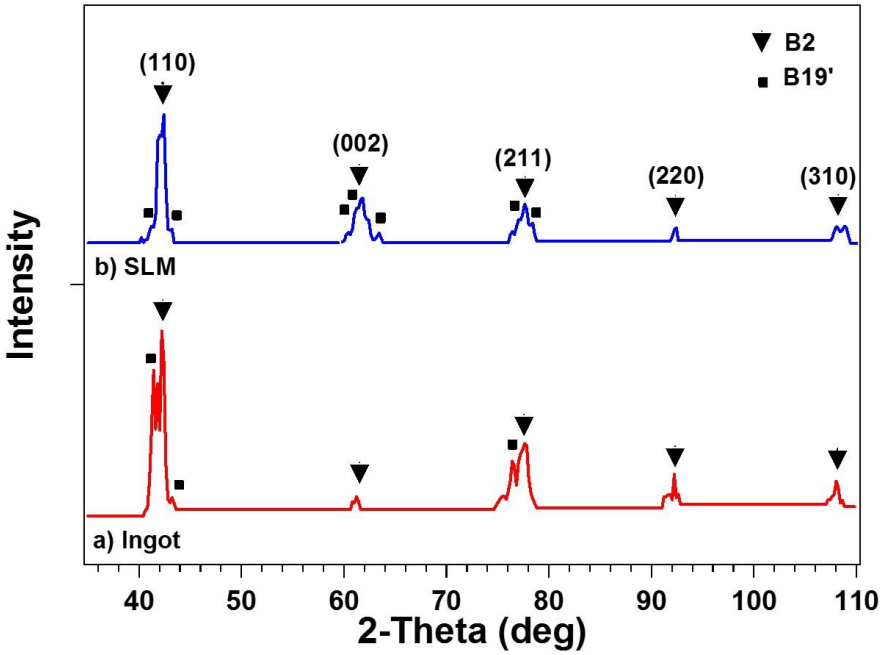

Figure 6-1 XRD spectra for (a) Ingot, and (b) SLM fabricated $Ni_{50.8}Ti_{49.2}$ obtained at RT

Figure 6-2 (a)-(c) presents the pole figures of [110], [002], [211], [220] excluding [310], orientations obtained from X-ray diffraction of the ingot and as-fabricated SLM sample along the BD and PBD. Pole figures provide a quantitative description of preferred orientations available in samples. SD is the normal direction while TD is the transverse direction. The pole figures of the initial ingot indicate a combined cubic and (111)<132> texture while SLM sample has only rotational cubic (fiber) texture. The rotational cubic texture of the SLM sample can be as a result of bidirectional scanning strategy at each layer where the formed cubic structured crystals are grown in different directions due to different maximum heat gradinet. Therefore the circular shape is observed in the center of pole figure. On contrary, rotation of the [200] plane which is paralel to the sample surface around the prepindicular axis, solely, will not provide necessary information for the initial ingot. Therfore, combination of diffractions from inclied planes with respect to the surface is required to establish. As it can be seen, the rotattion of the these inclined planes (for

instance [211]) around their prepindicular axis also produces peaks in intensity vs. rotation axis gragh which implies presence of in-plane texture in the initial ingot. The random texture of ingot which is consistent with the homogeneous nucleation mechanism inside the matrix means no preferential orientation of the nuclei is expected [131]. The ingot had a slight predominant [110] orientation, whereas SLM NiTi showed the highest intensity in [002] orientation at both the BD and PBD with a drastic reduction in the intensities of the other orientations. Since similar pole figures were observed in BD and PBD (Figure 6-2 (b) and (c)), similar shape memory responses can be expected. The hypotheis is the directional solidification of the NiTi parts fabricated by SLM develops a strong texture along the [001] orientation in these alloys which is in good agreement with the previous studies on NiTi [78, 132]. During the SLM process, the maximum thermal gradient is generally oriented along the building direction, therefore, the easy growth direction of grains is also aligned with this maximum gradient. Their rapid growth creates a texture which can be altered by modifying the scanning strategy [103]. Despite the fact that the formed texture depends on the local heat flow and the solidification mode, texture of SLM fabricated various materials can be different. For instance, SLM Tantalum has shown the preferred orientation of [111] in the BD [116] while most of the other SLM fabricated metals such as AlSi10Mg, CM247LC, Co29Cr6Mo, T-6Al-4V and 316L stainless steel have been reported to have [100] texture in the BD [94, 100, 114, 133-135]. Generally for alloys with the cubic crystal structure, epitaxial grain growth in [100] direction is expected [90, 114, 134]. However, availability of both [100] and [011] orientations has been reported for SLM CoCrMo alloy in the BD [90].

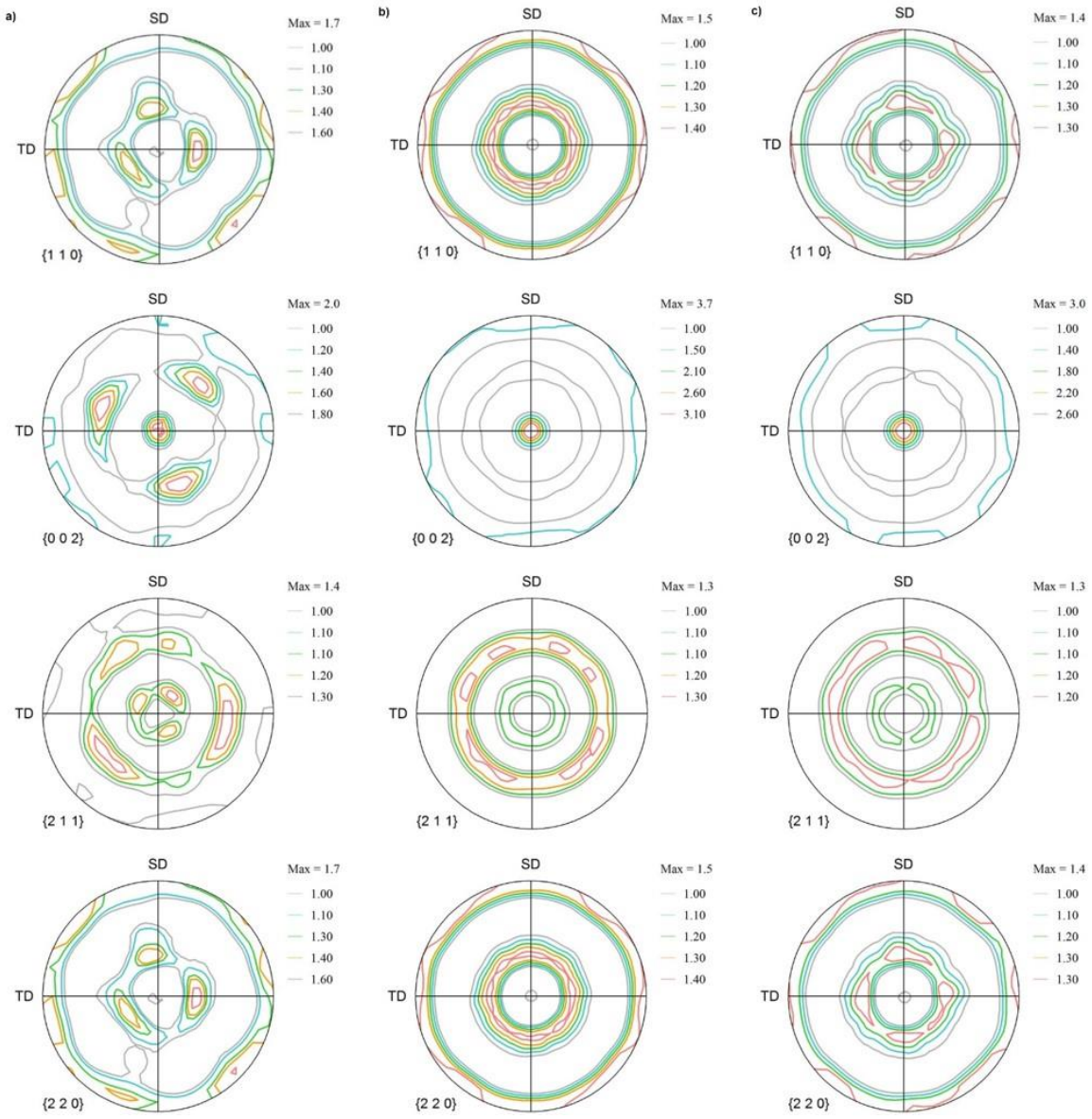

Figure 6-2 Pole figures of $Ni_{50.8}Ti_{49.2}$ in 002, 110, 211 and 220 orientations (a) the initial ingot, (b) BD, (c) PBD of SLM fabricated

6.2 Effects of aging temperature and time

Time, temperature and composition are the three main independent parameters for aging and aging in temperature range of 400-600ºC results in heterogeneous precipitation [40, 136, 137]. Figure 6-3 depicts the DSC graphs for SLM $Ni_{50.8}Ti_{49.2}$ alloys aged at temperatures from 350 ºC to 600ºC for 30 minutes, 1 hr and 1.5 hrs. DSC responses of the

ingot and the as-fabricated sample were included for comparison. TTs for as-fabricated samples is higher than the ingot which is consistent with our findings in our previous study [102]. TTs of samples were increased after aging up to 450ºC and then decreased after aging at higher temperatures. Aging of Ni-rich NiTi alloys causes variations in the nucleation energy, internal stress state and matrix composition with the formation of Ni-rich precipitates [138]. When the precipitates are small and coherent, their interparticle distance is also small that results in increased energy for nucleation and thus decreases M_s. On the other hand, formation of these Ni-rich precipitates depletes the Ni content of the matrix, resulting in increase of Ms. It should be noted that volume fraction of precipitates is temperature dependent as well. Lastly, the mismatch between matrix and precipitate lattice parameters may cause internal stresses around precipitates that can increase the M_s. Thus, when the precipitates are small and coherent, combined effects of all these three main factors in M_s should be taken into account. As the precipitates are grown larger and interparticle distance is increased, composition alteration becomes the main factor in the change of M_s.

The initial increase in TTs up to the aging temperature of 450ºC can be attributed to the formation of stress fields around the precipitates and composition change which is supported by the formation of R-phase as is discussed later. The drop of TTs for aging at higher than 450ºC is attributed to the reduction of volume fraction and coherency of precipitates. As the aging temperature increases precipitates grow larger, they lose their coherency and their inter-particle distance increases. At higher temperatures, the volume fraction of precipitates decreases and the matrix becomes Ni-rich again thus TTs are decreased [85, 120, 139-142].

Another important observation from Figure 6-3 is the formation of R-phase for the samples aged at temperatures equal or lower than 500ºC that results in double peaks. The corresponding R-phase peak is close to austenite peak (in reverse transformation) with small hysteresis while the very broad R-phase to martensite peak is hardly visible in most of the cases. The presence of R-phase is more visible because of its distinct peak during the B2 to B19' transformation. In reverse transformation, R-phase shows up as a shoulder of austenite peak after aging at 350 and 400ºC. The R-phase is a trigonal lattice with a martensitic nature and its formation is associated with the precipitation characteristics. Particularly, coherent Ni_4Ti_3 particles provide a microstructure which produces a strong resistance to large lattice variant deformations associated with the formation of B19' and favors the formation of the R-phase with smaller lattice variant prior to the formation of B19' [45, 123]. When samples were aged at a higher temperature than 500ºC, only a single peak was observed upon transformation which is also the case for as-fabricated and ingot. As the coherency of precipitates decrease at higher aging temperatures R-phase disappears at temperatures higher than 500ºC. The presented aging temperature dependent DSC charts of SLM fabricated $Ni_{50.8}Ti_{49.2}$ are in good agreement with previous studies on conventional $Ni_{50.8}Ti_{49.2}$ [143, 144].

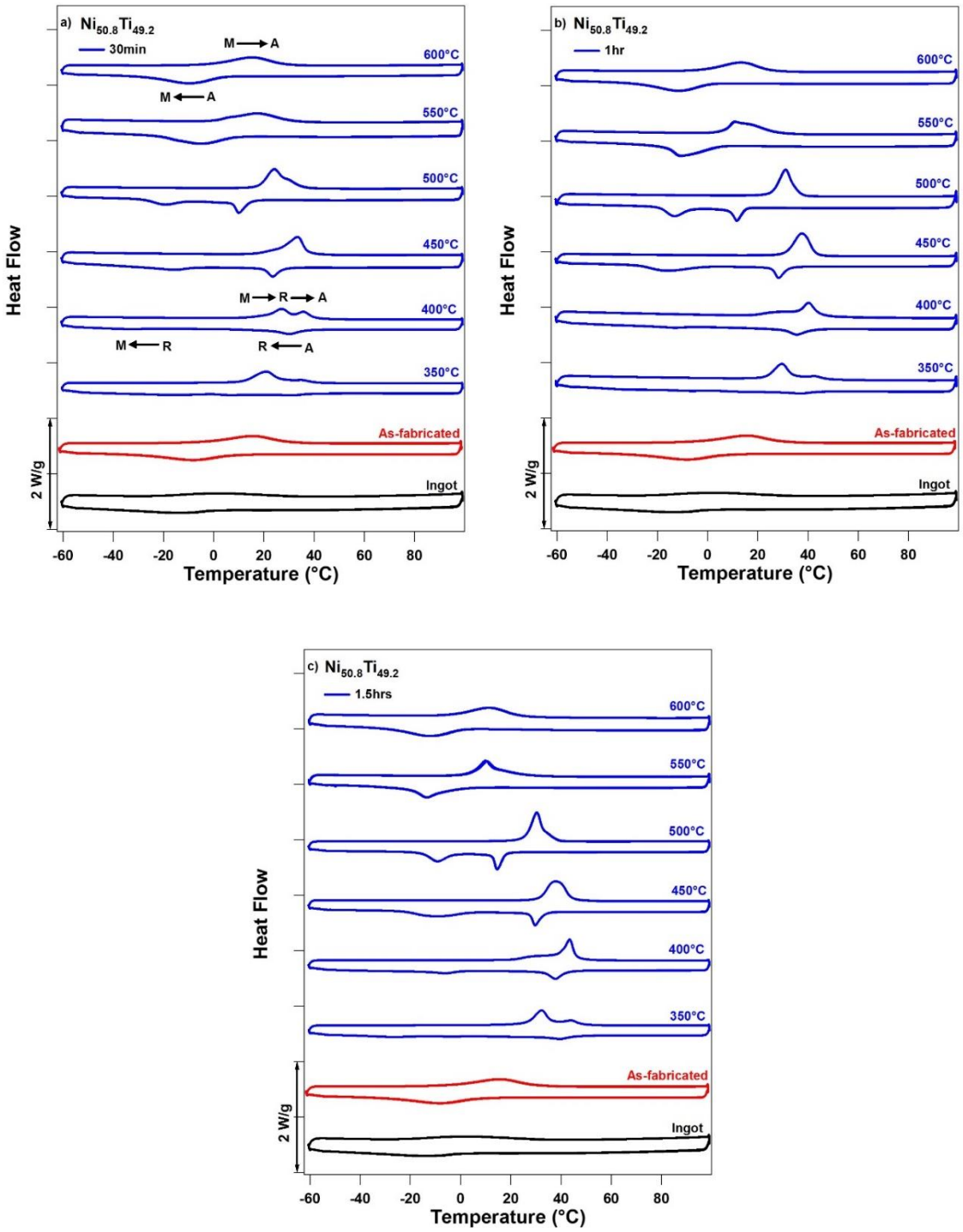

Figure 6-3 Temperature dependent DSC response of SLM Ni50.2Ti40.8 aged at 350 to 600ºC for (a) 30 min, b) 1hr, (c) 1.5 hr

Figure 6-4 (a) and (b) are the DSC responses of SLM samples aged at 350ºC and 600ºC as a function of time from 30 min to 18 hr. In all samples aged at 350ºC, R-phase

transformation was observed. While B2 (austenite) to R-phase peaks were pronounced in martensitic transformation, during the reverse transformation, B19'(martensite) to R-phase and R-phase to B2 peaks overlapped. For conventionally fabricated Ni-rich NiTi, it is possible to observe three or more peaks during transformation [45, 121, 136]. This behavior has been attributed to the composition inhomogeneity resulting from Ni_4Ti_3 precipitates and the difference between the nucleation barriers for R-phase and B19'. In SLM fabricated Ni-rich NiTi alloys also three peak or wavy transformation was observed when samples at 350ºC up to 1.5hr. For longer aging times, two distinct peaks were observed during the martensitic transformations. Although 350ºC-aged samples showed double peaks in certain conditions, 600ºC-aged samples showed single step but broad transformation peaks regardless of aging time. For 600ºC-aged samples, TTs were slowly decreased with aging time while TTs of aged samples at 350ºC were increased with aging time. Similar to increasing the aging temperature for a constant time, increasing the aging time at 350ºC, resulted in larger size particles and as a result, Ni in the matrix decreases and TTs are increased. However, in over-aged states (prolonged or high temperature aging) as large particles either lose their coherency or the particle spacing becomes too large, TTs start to decrease.

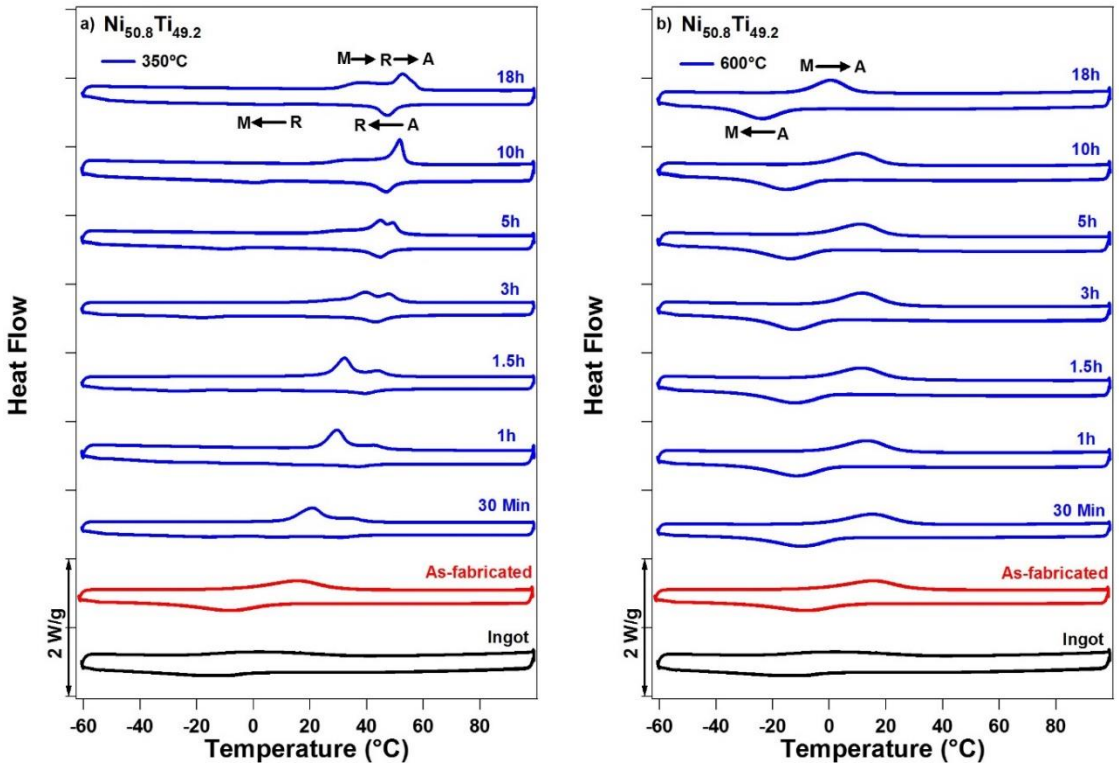

Figure 6-4 Time-dependent DSC response of SLM $Ni_{50.8}Ti_{49.2}$ aged from 30 min to 18 hr at (a) 350˚C, (b) 600˚C

6.3 Hardness

Figure 6-5 (a) shows the Vickers hardness of all samples aged for 30min, 1h and 1.5hr as a function of aging temperature at RT. Hardness of NiTi alloys is complicated and highly dependent on temperature and the existing phase. Therfore, stress-induced austenite to martensite (or R-phase) transformation or variant reorientation and dislocation could occur during the hardness test [16, 130]. In addition, the type of formed particles after aging, size and quantity of them may affect the measurements. All in all, Vickers hardness of all samples follows a decreasing trend with aging temperature. The 1 hr aged samples up to 450ºC have the highest Vickers hardness, however, for the samples aged above 450ºC hardness drops drastically. The reason might be grown precipitates and their inter-particle distance as a result of higher aging temperature. The hardness of 1.5 hr aged samples was

found to affect minor by temperature. Figure 6-5 (b) depicts Vickers hardness of all these samples as a function of aging time. Interestingly hardness of both aging sets follows a similar trend. Samples aged at 350ºC have higher Vickers hardness than 600ºC-aged samples. The highest hardness in both aging temperatures was determined to be at 5 hr.

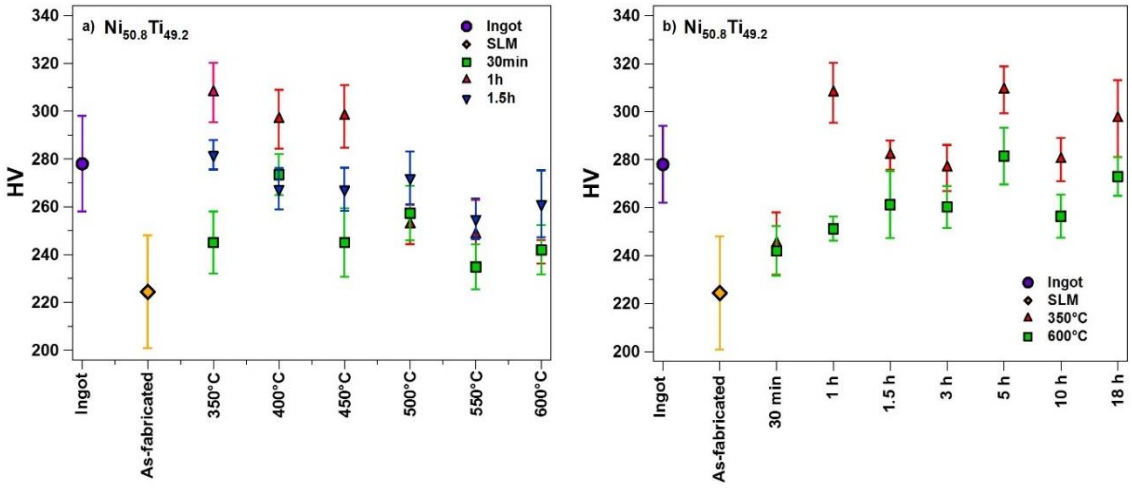

Figure 6-5 Vickers hardness of SLM $Ni_{50.8}Ti_{49.2}$ as function of aging (a) temperature, (b) time

6.4 Thermal Cycling under Stress

Figure 6-6 depicts the thermal cycling under selected stress levels of 350ºC-1h aged sample. At each cycle, the sample was loaded to selected compressive stress levels in austenite, then cooled down below M_f to fully transform to martensite and heated up to well-above A_f to transform back to the austenite. Multiple thermal cycling tests were performed at compressive stress levels ranging from 50 MPa to 400 MPa. A triangular shape transformation was observed under low-stress levels where the strain-temperature curve slope in the forward transformation was lower than that of the back transformation. It should be noted from the DSC response shown in Figure 6-4 that the transformation peaks were broader during cooling. The broad transformation temperature range during the cooling can be attributed to the large difference between R_s and M_f. Upon heating, the

temperature difference between R_f and A_s is low, thus resulting in more sudden back transformation [145].

As the stress level was increased, a symmetric behavior was observed since austenite transforms directly to martensite which can be attributed to the fact that R-phase transformation is stable while M_s increases linearly with stress. Therefore, after certain stress level, M_s becomes higher than R_s and R-phase transformation disappears. Figure 6-6 also depicts the thermal cycling responses of the as-fabricated sample at selected stress levels for comparison. In agreement with DSC results, TTs of the as-fabricated sample are lower than the aged sample. It is noteworthy that based on both hardness and thermal cycling under stress results, after only 1 h aging at 350ºC, the strength of the sample was increased considerably. Fully recovered transformation strain of up to 4% was observed for the aged sample while the irrecoverable strain of 0.5% occurred for the as-fabricatd SLM sample under 300 MPa. The temperature hysteresis and transformation strain of as-fabricated sample are slightly higher than aged sample. Fine, short spaced and coherent precipitates in aged sample might result in untransformed local regions in the microstructure, restrict the detwinning and growth of favored martensite variants and hence lower the transformation strain [47, 146, 147].

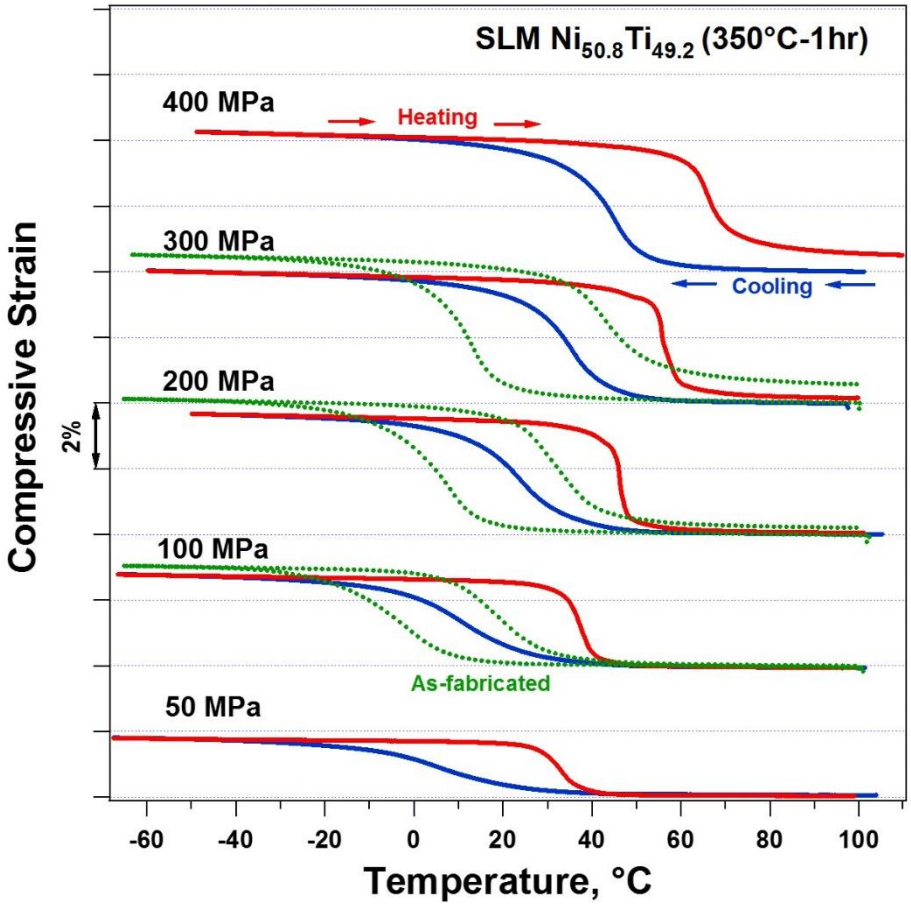

Figure 6-6 Thermal cycling under constant stress of 1 h aged at 350ºC SLM $Ni_{50.8}Ti_{49.2}$

6.5 Room/Body Temperatures Supeelastic Response

The superelastic responses of the ingot, as-fabricated, and aged SLM samples were shown in Figure 6-7**.** To consider the possibility of obtaining practical superelasticity for potential biomedical applications, all tests were carried out at room temperature 24 ºC or body temperature 37 ºC regardless of their A_f. To conduct the experiments samples were loaded to 2, 4, 6, and 8%, successively. Next, samples were loaded up to their failure to examine their ductility. It is clear that as the loading amount increased, plastic deformation and hysteresis were increased and resulted in higher irrecoverable strain.

Figure 6-7 (a) shows the response of the ingot at 24ºC. The A_f of the ingot was -6ºC. The sample showed 2% strain recovery at the first cycle. However, when loaded 4%, the irrecoverable strain of 0.6% was observed. After SLM fabrication, M_s and A_f were increased to 8 and 30ºC, respectively. The sample shows only partial superelasticity (Figure 6-7 (b)), indicating lower strength. The failure experiment shows a drastic decrease in ductility of the sample after SLM process. While the initial ingot failed after 20% deformation at a stress level of 3100 MPa, the as-fabricated endured only 12% deformation and failed at 1750 MPa. The decrease in ductility of the SLM-fabricated sample can be attributed to the texture, larger grain size and checker type grains. Polycrystalline alloys require higher stresses to initiate slip than in the equivalent single crystals due to the higher geometrical constraints of grains [148]. At the same time, SLM fabrication is prone to the formation of inner defects such as pores, unmolten particles or internal cracks which can affect the strength of material [149].

Compressive response of 350ºC-30min aged sample at 24ºC is shown in Figure 6-7 (c). The sample does not show full recovery even after only 2% loading. It should be noted that the A_f of the sample is 42ºC and thus, fully reversible SE is not expected. Nevertheless, the sample has better ductility than the as-fabricated SLM sample. Figure 6-7 (d) shows the compressive response of 350ºC-1h aged sample at 37ºC. The A_f of the sample is 49ºC and has a higher hardness than 30min aged sample. The sample shows up to 4% perfect superelasticity at 37ºC. After 6% loading, the irrecoverable strain is 1.5%.

Figure 6-7 (e) and (f) show the compressive stress cycling responses of the samples aged at 600ºC for 30 min and 1.5 h. The 30 min aged sample has A_f of 29 ºC and it showed full strain recovery after 2 % loading and then the irrecoverable strain of 0.5% was

observed after 4% loading. After increasing the aging time to 1.5 hr, (Figure 6-7(f)), the A_f was decreased to 24ºC. The sample fully recovered up to 4% strain at 24ºC. Even after 6% loading, only 0.7% irrecoverable strain was observed.

From Figure 6-7 critical stress for plastic deformation of samples can be determined. While the critical stress to initiate the plastic deformation for the ingot was 1175 MPa, the SLM fabricated sample showed higher critical stress which was about 1335 MPa. After only 30min aging at 350ºC, the critical stress for plastic deformation was increased to 1650 MPa and when the aging time doubled to 1hr, the critical stress for plastic deformation found to be 1820 MPa. Aging at 600ºC increased the critical stress for plastic deformation as well, however, with a slower rate. The critical stress for plastic deformation of the 600ºC-30min aged sample was 1350 MPa which was slightly higher than as-fabricated sample. When sample aged for 1.5hr, the critical stress of sample was increased to 1451 MPa.

Formation of Ni_4Ti_3 particles is known as the main reason for higher strength and superelasticity improvement, particularly when they are small and coherent [54]. Coherent particles in the matrix make the motion of dislocations difficult since they need to either pass through precipitates or bypass them [85]. Therefore, the hardening effect provided from Ni_4Ti_3 particles increases the critical stress for plastic deformation. Meanwhile, since these particles act as nucleation sites for martensite, the critical stress for the martensitic transformation of samples is decreased. It is noteworthy to mention that characteristics of these particles are critical and can be tailored by aging.

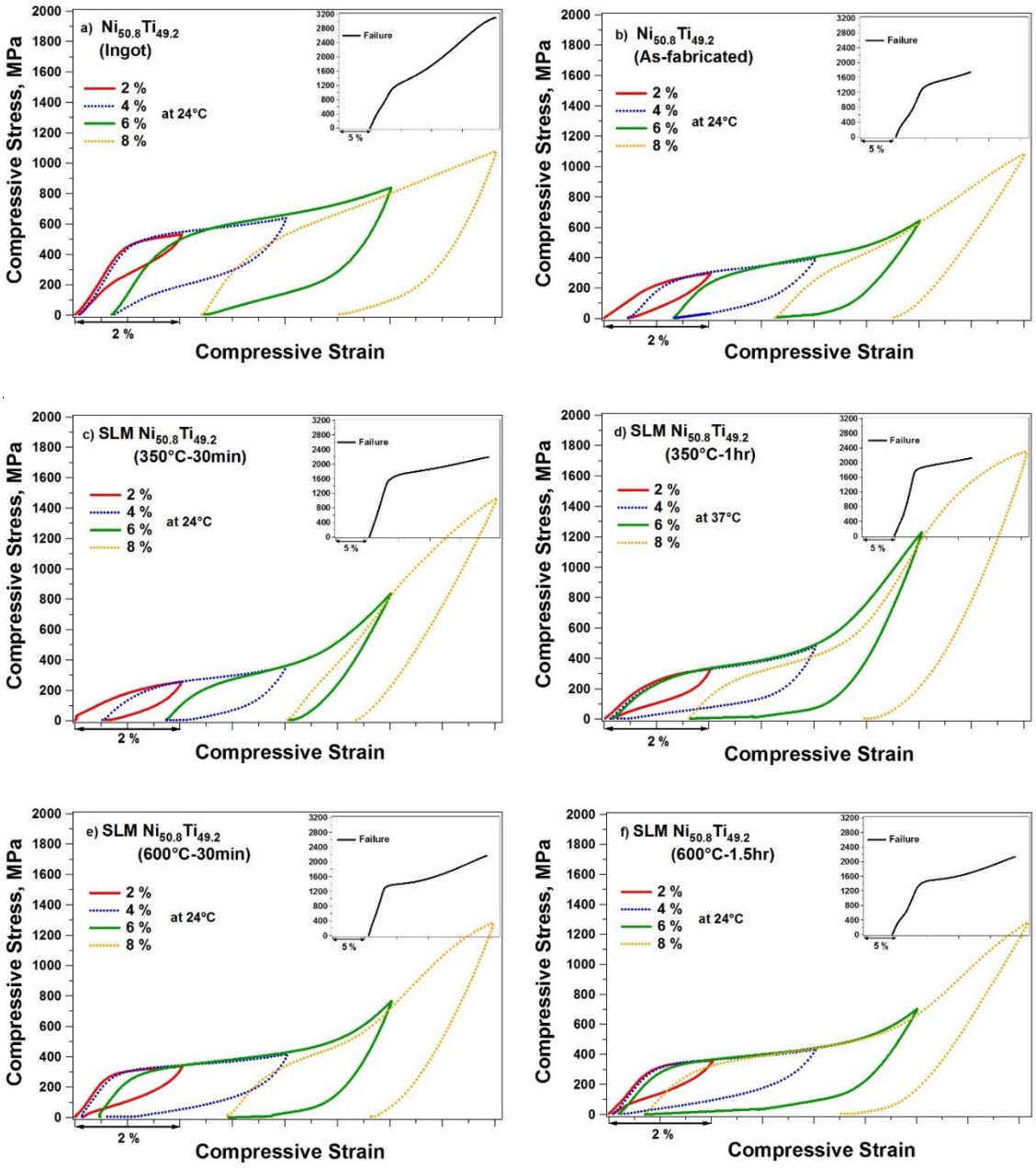

Figure 6-7 Superelastic response of SLM $Ni_{50.2}Ti_{40.8}$ aged for (a) The initial ingot, (b) SLM as-fabricated, (c) 30 min at 350˚C, (d) 1hr at 350˚C, (e) 30 min at 600˚C, (f) 1.5hr at 600˚C, at room and body temperatures

6.6 Discussion

For singlecrystal alloys, the critical stress for stress-induced martensite and maximum transformation strain are orientation dependent. Strain recovery is greater in orientations with lower critical stress. Similarly, the shape memory and superelastic

responses of polycrystalline NiTi are also texture dependent. If the texture is nearly random, as in the case of the initial ingot, the behavior of the polycrystal approximately becomes an average of the behavior of single crystals of all orientations [34]. Yet, if the polycrystalline NiTi, has a strong texture in a particular orientation, similar behavior as a single crystal of that orientation can be expected. The attempt to process a polycrystalline SMA to achieve strong texture close to the orientation exhibiting the best sets of shape memory or superelastic properties can be conducted using traditional techniques like cold rolling and cutting the sample in a specific direction. However, it is difficult to control texture precisely using these methods [34]. SLM fabrication process clearly creates a preferred and sharp texture in samples. SLM fabrication parameters such as laser power and scanning speed, the scanning strategy play a major role in the preferred orientation of growing crystal at each layer. Therefore, the possibility of tailoring the orientation provides another opportunity for enhancement of shape memory response of SLM fabricated NiTi alloys. As shown in Figure 6-7 the superelastic response of the SLM fabricated samples displays a Luders type transformation with lower critical stress for martensitic transformation which can be attributed to the strong [001]-texture. Noteworthy, the observed amount of recoverable of strain for aged SLM NiTi is equal or even higher than the 5.2 % theoretical number for maximum recoverable strain (given in Table 1-1) for [001] orientated single crystal [150]. Conversely, the ingot shows higher strain hardening and critical stress. This is in perfect agreement with the previous studies concerning the effects of orientation on shape memory response of single crystalline NiTi. It has been reported that [001] and [148] oriented $Ni_{50.8}Ti$ single crystals have the lowest Schmid factors for austenite slip among other directions and they produce the highest recoverable and

transformation strains while [111] oriented single crystal $Ni_{50.8}Ti$, delivers the smallest [13].

6.7 Summary and Conclusion

In this chapter texture of SLM fabricated $Ni_{50.8}Ti_{49.2}$ were investigated. A comprehensive aging study of as-fabricated alloys is also presented to reveal the effects of aging time and temperature on Transformation behavior. The shape memory properties were investigated by shape memory effect and superelasticity experiments. The main conclusions are as follows:

- The SLM fabricated samples are found to have texture along the [001] orientation in the BD while the initial ingot had random texture.
- Temperature dependent DSC chart displayed that TTs are increased when samples are aged up to 500ºC and phase transformations were accompanied with intermediate R-phase. When they were aged at higher temperatures, TTs decreased and R-phase formation was not observed
- Thermal cycling under the stress of 350ºC-1hr aged sample displayed 4% transformation strain under 300MPa stress.
- Full strain recovery of 4% and also 5.5% after 6% deformation was observed after 350˚C-1hr and 600˚C-1.5hr aging at body and room temperatures
- Shape Memory effect and superelasticity experiments provided very promising results which are aging dependent. The appropriate thermal treatment even without solution annealing can significantly improve the SLM fabricated NiTi thermo-mechanical behavior and at the same time adjust the transformation temperatures for specific applications.

7 Chapter Seven: Shape Memory Response of Equiatomic and Ni-rich Porous SLM NiTi

A major classification of porous metals, or metal foams, is between open-cell and closed-cell. In open cell metallic foams, metallic struts form the structure frame, and open pores are interconnected. In closed cell foams, the pores filled with gas are isolated by cell wall metal.

Depending on the necessity of the application, porous SMAs could be manufactured with open or closed pore designs, however, when it comes to fabricating functional porous metals it is open-cell porous metals that are the preferred standard [151]. Both types of foams are lightweight structures with a large surface to volume ratio; however, most of the pore surfaces in closed cell foams do not function [152]. Closed-cell porous metals are usually the result of a random foaming process, in which the size, shape and location of pores within the matrix varies, depending on the parameters of the fabrication process [153]. On the other hand open cell metal foams have well-controlled pore structures, they are lightweight with high stiffness, they have high gas/fluid permeability with a large surface area to volume ratio [152].

While conventional manufacturing processing does not allow for the production and engineering of porous NiTi [51], AM has offered unique opportunity to overcome the manufacturing difficulties in producing porous NiTi samples [73, 75, 154]. AM builds up a material directly from CAD data in layer by layer or even pixel by pixel to the desired shape. Consequently, complex components such as lattice-like structures can be fabricated

with ease. Fabricated parts by using selective laser melting (SLM) technology show low impurity, microstructure control and meet the requirements prescribed in the ASTM F2063-05 for medical NiTi. NiTi alloys due to their well-known shape memory effect and superelasticity have been used in a vast number of surgical instruments, cardiovascular, and orthodontic applications. In addition, they have high damping, wear resistance, ductility, fatigue resistance and biocompatiblity [24, 25, 155-163]. On top of these, NiTi alloys offer low stiffness, superelasticity behavior, and hysteresis similar to bone which make them perfect candidate to be used in biomedical applications, especially metallic scaffolds [51, 164]. In general, low stiffness at the level of bone is desirable in order to avoid stress shielding effect, which is the major reason for implant loosening and failure [165-167]. Titanium, cobalt-based alloys, and stainless steel are other commonly available alloys being used in biomedical applications. These materials present stiffness of about 110 GPa, 190 GPa, and 210 GPa, respectively [168, 169], which are much higher than the human cancellous (<3 GPa) or cortical (12-20 GPa) bones [170]. High stiff implants carry the major porting of loading while they shield the surrounding bone from carrying load. According to Wolf's law, the stress shielded bones would be due to the lack of required level of stress, and, therefore, the bones start to resorb and continue until the failure of implant [171-176]. Although NiTi present low stiffness (40-60 GPa), it is still required to further decrease and tune the stiffness to match that of cortical bone stiffness (12-20 GPa) [177].

A promising solution to tune the stiffness is to introduce porosity into the metallic implants [26, 170, 178]. Porous materials provide an excellent opportunity to engineer and optimize their mechanical properties by controlling the porosity level, and pore size, shape,

and distribution to better match the properties of natural bone [68, 179]. Since the stiffness decreases with porosity level in porous and cellular materials [169]. Porosity, in addition to lowering stiffness, enhances bone ingrowth, improves the strength of the implant/bone interconnection, and, an adjustable porosity in the range of 35-80% together with the superelastic properties of the SMA can decrease the risk of stress shielding effect [180, 181] and allows mechanical properties to adapt to the human bone [182]. Porosity also can be used to produce the desired texture on the surface for bone ingrowth. Pore size, geometry, and connectivity can be tailored to reduce the density and increase the permeability to allow blood vessels migrate, allow the bone ingrowth and improve the strength of the implant/bone interconnection [163, 169, 183, 184]. The optimum range of pore size has been reported to be from 100 to 600 μm to ensure the bone in-growth in the highly porous structures [54, 163, 180].

In this section, cellular lattice structured NiTi samples with selected morphology and levels of porosity were fabricated via SLM method. The mechanical properties and shape memory response of the porous SLM fabricated $Ni_{50.1}Ti_{49.9}$ (at %) parts were investigated and compared to that of the dense sample. Furthermore, since a bone implant may experience several cyclic loading during its operation causing the accumulation of plastic strain, functional stability along with the effects of cyclic loading on the mechanical response of NiTi cellular lattice structures are also assessed.

7.1 Fabrication

Powders of near equiatomic $Ni_{50.1}$-$Ti_{49.9}$ and Ni-rich $Ni_{50.8}$-$Ti_{49.2}$ (at.-%) ingots were used to fabricated SLM porous samples. Porous NiTi parts are generated by repeating identical unit cells in *x*, *y*, and *z* directions. In this study, three different geometries are

selected as unit cells. The first unit cell consists of three orthogonal struts that intersect at the midpoint as shown in Figure 7-1 (a) and this type is named as a simple cubic (SC) unit cell in this paper. The second unit cell is named as BCC which is constructed by eight diagonal struts to connect the center of the upper and lower faces of a cube to the center of its vertical edges as shown in Figure 7-1 (b). The third unit cell is named as BCC-Z and it has an additional vertical strut than the BCC, which connects the center of the lower and upper faces as shown in Figure 7-1 (c). The lattice structures created from BCC and BCC-Z unit cells offer nearly optimized configurations for bending, compression, and shear loadings [185-187].

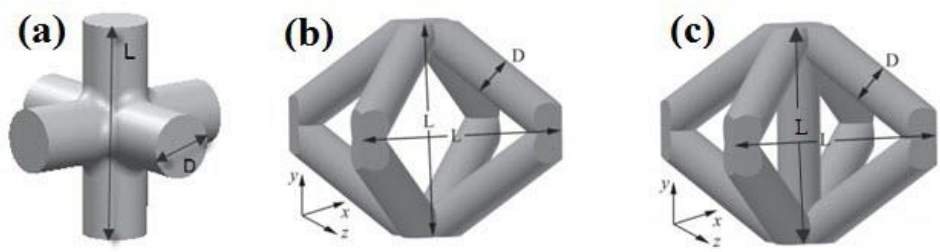

Figure 7-1 The repeating unit cell of (a) SC, (b) BCC, and (c) BCC-Z cellular lattice structure

To investigate the mechanical properties of the above-mentioned cellular lattices, three different parameters should be defined; strut diameter (D), cell length (L), and the number of repeating unit cells along each direction. Table 7-1 shows the selected parameters along with the relevant level of porosity which is defined as the ratio of the pore volumes to the total volume of the solid part.

Table 7-1 The dimensions of specimens and their relative level of porosity

Name	D (mm)	L (mm)	Number of Cells	Porosity (%)
Dense	4.78	10	-	0

SC-32	1.4	2	4 × 4 × 4	32
SC-45	1.2	2	4 × 4 × 4	45
SC-58	1	2	4 × 4 × 4	58
BCC-Z	0.65	2.33	4 × 4 × 3	65
BCC	0.65	2.33	4 × 4 × 3	69

The sample dimensions used for fabrication of porous SC, and BCC/BBC-Z for mechanical tests were 8 × 8 × 8 mm^3 and 9.32 × 9.32 × 7 mm^3, respectively. Two plates were attached to the bottom and top of each cell to facilitate the uniaxial compression testing. The thicknesses of these plates were 1.5 mm and 0.93 mm for SC and BCC/BCC-Z, respectively. Figure 7-2 shows the fabricated parts. The three levels of porosity achieved in the fabricated parts are 58%, 45%, and 32%. Also, a solid rod (with zero porosity) with 4.65 mm diameter and 10 mm height was fabricated and tested for comparison.

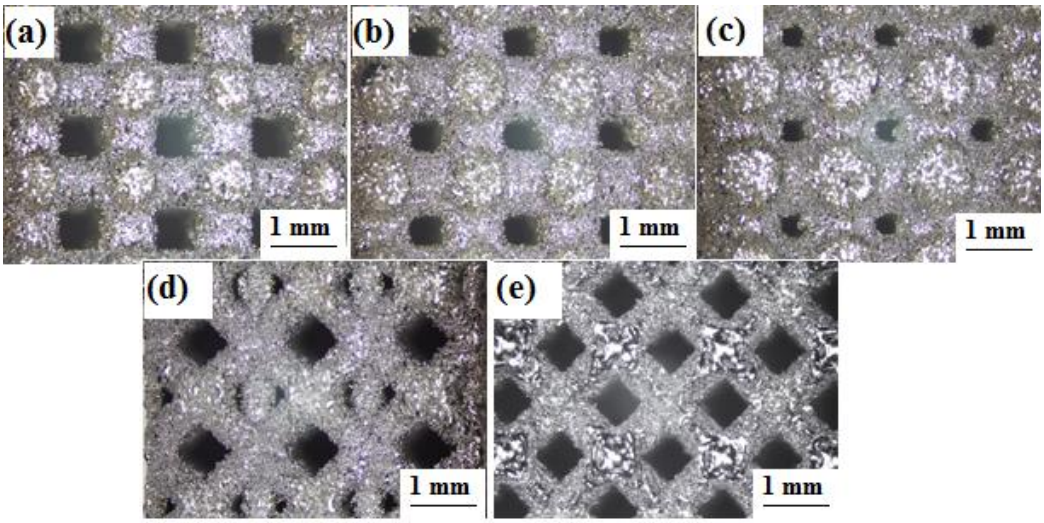

Figure 7-2 Images of SLM fabricated NiTi parts. (a) SC-58, (b) SC-45, (c) SC-32, (d) BCC-Z, and (e) BCC.

7.2 Thermo-Mechanical Response of Porous SLM $Ni_{50.1}Ti_{49.9}$

7.2.1 Thermal Analysis

Figure 7-3 shows the DSC plots of the initial ingot, powder and SLM $Ni_{50.1}Ti_{49.9}$. Multiple peaks were observed for powder DSC which was attributed to the inhomogeneous heat transfer in the powder and/or compositional inhomogeneity of particles [102]. While the initial ingot showed a small shoulder during martensitic transformation, phase transformation of SLM fabricated sample occurred in a single peak. Temperature hysteresis of the ingot and SLM samples were almost the same. However, transformation temperatures (TTs) were different. TTs determined from the DSC results are shown in Table 7-2. TTs had slightly shifted to lower temperatures after powder atomization, and increased after SLM process. When compared to the ingot, in the SLM sample, M_s and M_f were both decreased by 12˚C while A_s and A_f were decreased by about 10˚C and 14˚C, respectively. The change in TTs after SLM process can be attributed to the picked up impurities, particularly oxygen and carbon during the process. Since titanium is active, secondary phases such as TiC, TiO_2, Ti_2NiO_x can be formed. The formation of such Ti-rich secondary phases increases the Ni concentration of the matrix as well as they may hinder the martensite nucleation and consequently decreases the TTs.

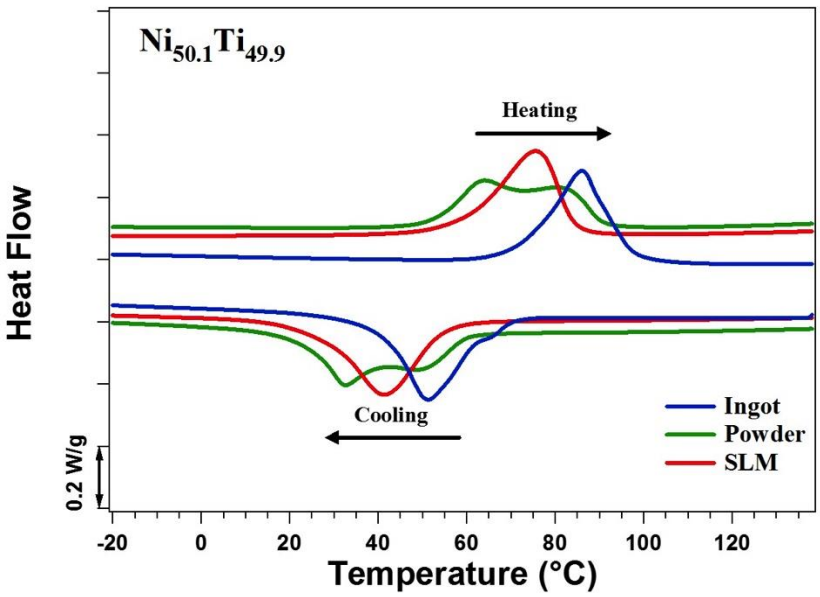

Figure 7-3 DSC plots of Powder and SLM $Ni_{50.1}Ti_{49.9}$

Table 7-2 Transformation temperatures of Ingot, Powder, and SLM $Ni_{50.1}Ti_{49.9}$ extracted from DSC plots

$Ni_{50.1}Ti_{49.9}$	M_s(˚C)	M_f(˚C)	A_s(˚C)	A_f(˚C)
Ingot	73	38.75	68.8	100
Powder	59.1	22.5	53	91
SLM	58	26	59	85

Figure 7-4 shows the DSC curves of ingot and SLM $Ni_{50.1}Ti_{49.9}$ for 20 cycles. For both samples, TTs decreased and then stabilized with thermal cycling. The A_f and M_s temperatures of the initial ingot decreased from 100 ºC and 73 ºC at first cycle to 91 ºC and 56 ºC at the 20th cycle. The A_f and M_s temperatures of the SLM fabricated sample dropped from 85 ºC and 58 ºC at first cycle to 80 ºC and 52ºC at the 20th cycle. The shift of TTs to lower temperatures is in good agreement with literature [85, 188]. Thermal cycling results

in increased dislocation density and statistically distributed martensite variants results in opposing strain fields. These fields accommodate on each other or slow down the growth of new martensite. Therefore, M_S decreases steadily during cycling. With increasing the cycling number, smaller martensite plates form between the larger regions of stabilized martensite. This results in a higher number of martensite/austenite interfaces and consequently increases a driving force for reverse transformation upon heating and therefore the A_s also decreases [188]. Similar results for near equiatomic NiTi produced by SLM are reported in previous works [61, 70].

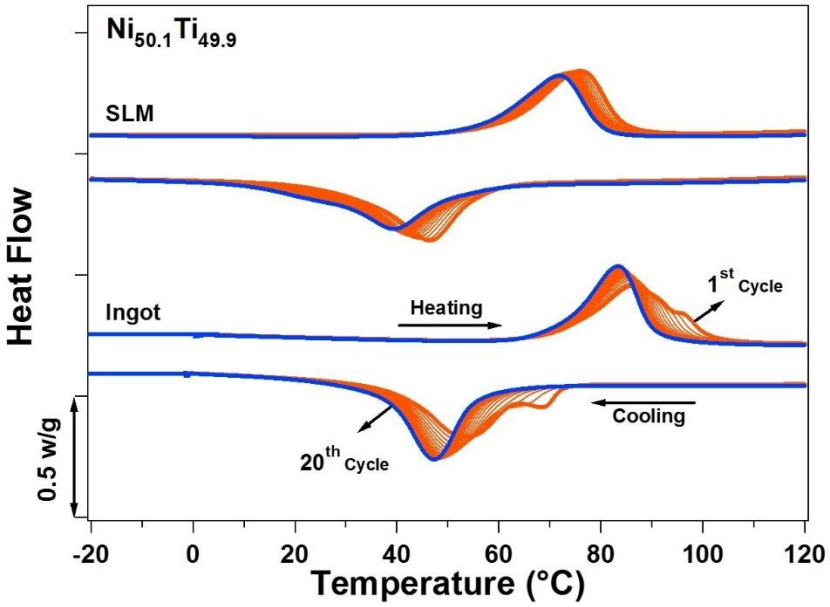

Figure 7-4 Thermal cycling behavior of ingot and SLM $Ni_{50.1}Ti_{49.9}$

7.2.2 Failure Analysis

Figure 7-5 compares the compressive response of dense and porous samples up to failure at 24ºC. It is clear that the mechanical response of NiTi is highly affected by adding porosity to the structures. Young modulus, critical stresses, and strains were all decreased with increased porosity level. Ductility of the samples were also decreased with porosity.

While dense structure endured the deformation of 30.2 % and failed at 1620 MPa, SC-58 was failed after 15.6% at 410 MPa. BCC-69 was failed at 63 MPa with 10.5% deformation. Pore morphology also affects the mechanical response of the samples. It has been previously shown that by increasing the portion of the axial load in the deformation mechanisms of a porous material, the stiffness of that material would increase in the loading direction. However, in the case of porous SMAs, by increasing the portion of bending in the deformation mechanisms of a porous SMA, the effects of asymmetric material response will increase [185].

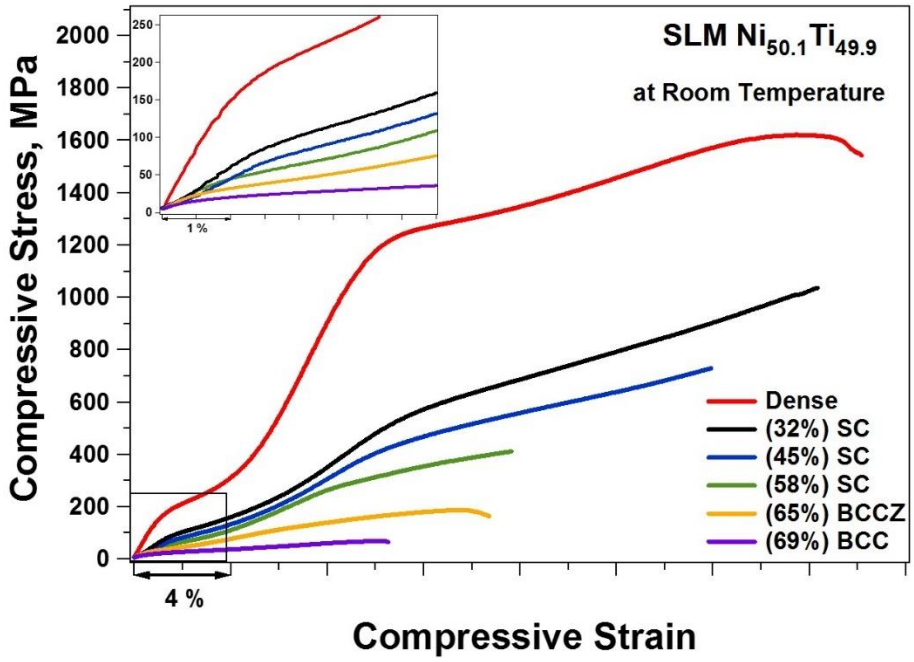

Figure 7-5 Compressive response of dense and porous SLM Ni50.1Ti49.9 samples at room temperature

7.2.3 Superelasticity of Dense SLM $Ni_{50.1}Ti_{49.9}$

Figure 7-6 (a) shows the temperature dependent compressive response of dense sample. The first test was conducted at 80ºC which is above M_s. The sample was loaded up to 5% strain where stress-induced martensite transformation was observed and then

unloaded. Superelasticity is not observed since the testing temperature is below A_f, however when the sample was heated above A_f, recoverable strain (ε_{rec}) of 2.9 % was observed due to back transformation. The irrecoverable strain (ε_{irr}) was 0.85 % after heating, which can be attributed to plastic deformation and/or stabilized martensite. The testing temperature was increased by 20˚C at the next step and the same procedure repeated. At 100 ºC and 120 ºC, partial recovery was observed during unloading and further recovery was observed during heating. At 100 ºC, the ε_{rec} was 2.5% upon unloading and 4.1% after heating. At 120˚C, the ε_{rec} was increased to 3.1% upon unloading and further recovery was not observed upon heating. The superelastic recovery was decreased at 140˚C since increased temperature results in the higher required critical stress for martensitic transformation and thus, increased plastic deformation. Based on the above results, 120˚C was chosen to run superelastic cycling tests as shown in Figure 7-6 (b). The samples were cycled eight times between 5 and 800 MPa. In the first cycle, the sample is loaded till 8% and only small back transformation was observed upon unloading with ε_{irr} of 5%. The response is stabilized with cycling and stress hysteresis and ε_{irr} of each cycle were decreased with increasing number of cycles. At the eight cycle, the ε_{irr} was less than 0.1% and the total residual strain in the sample was determined to be 6%.

The poor superelastic response of the SLM fabricated NiTi samples is as expected since equiatomic NiTi do not show superelasticity even in the solutionized conditions due to low strength [31]. One of the practical method to improve the shape memory properties of NiTi alloys is the use of Ni-rich alloys and precipitation formation [130]. Another advantage of Ni rich samples is their lower transformation temperatures. Additionally, SLM fabricated samples are prone to formation of secondary phases inner defects such as

pores, unmolten particles or internal cracks which can affect the strength of material in compare to conventionally fabricated NiTi [149].

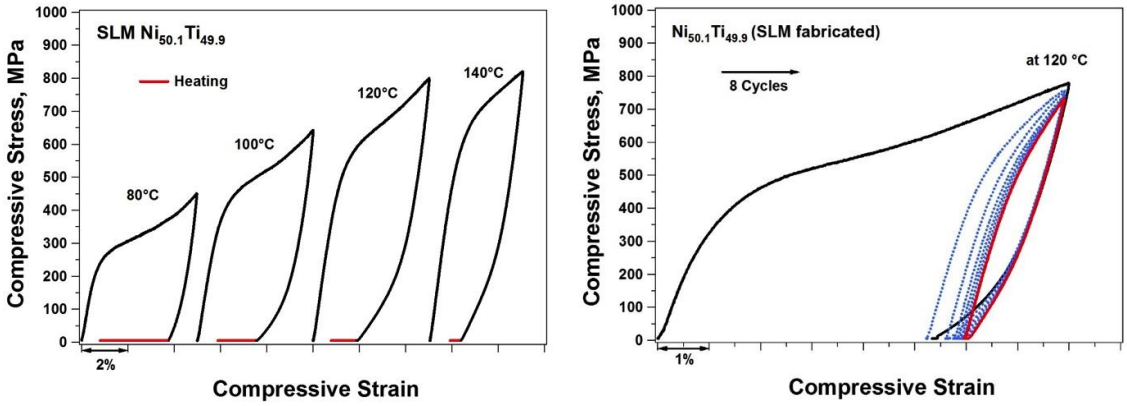

Figure 7-6 (a) Temperature dependent stress-strain curves and (b) Superelasticity cycling of dense SLM $Ni_{50.1}Ti_{49.9}$ sample

7.2.4 Shape Memory effect and Cyclic Stability of SLM $Ni_{50.1}Ti_{49.9}$

NiTi cellular lattice structures are suitable candidates for being used as bone implants. A bone implant may experience several cyclic loading during its operation causing the accumulation of plastic strain. To be able to assess the effects of cyclic loading on the mechanical response of NiTi cellular lattice structures, all the fabricated samples tested under stress-controlled cyclic compression. Figure 7-7 shows the cyclic mechanical behavior of dense and SC porous samples to evaluate the functional stability of the shape memory effect. In each cycle, the sample was deformed at room temperature in martensite state and the plateau corresponds to detwinning of martensite. After reaching to certain stress level, the sample was unloaded and heated up to 140˚C, which is well above A_f and then cooled back to room temperature for next cycle. The procedure was repeated for eight times. The maximum stress level for each sample was determined according to the failure results provided in Figure 7-5. It is well known that equiatomic NiTi alloys have poor

superelastic responses due to their low strength [31]. Thus, in general, they are used in applications where shape memory effect is employed.

Figure 7-7 (a) displays the stress-strain responses at room temperature while 7b shows the strain recovery curves of the samples upon heating. To comprehend the figures, the test procedure for the first cycle has been sequenced. First, samples were loaded at room temperature to selected stress level (process 1-2) and then unloaded (process 2-3) to 5 MPa. Next, the samples were heated up to a temperature above Af temperature (process 3-4) to observe the recovery. Lastly samples were cooled down to room temperature to start the next cycle (process 5-6). Due to the back transformation and induced strain upon cooling, the second cycle starts at point 6. The process 5-6 were omitted for the rest of cycles to make the figure clear. The maximum stress levels for cycling experiments were determined from failure tests and adjusted according to the porosity levels. Applied maximum stresses during the cycling tests were 800 MPa for dense sample. Stress levels of 420, 320, and 240 MPa were used for SC-32, SC-45, and SC-58 porous samples, respectively, which were adjusted due to their density. Dense sample shows full shape recovery upon heating at first cycle while negligible irrecoverable strain was observed in porous samples, however, all as the number of cycles were increased the response was stabilized and full recovery was achieved in all of the samples. Figure 7-8 (a) and (b) depict the evolution of ε_{rec} and ε_{irr} , respectively, with cycling where the data were extracted from Figure 7-7. An accumulation of ε_{irr} occurs during cycling. The highest ε_{irr}can be observed in the first cycle, while they decay by increasing cycles. Moreover, the amount of ε_{irr} increases by increasing the level of porosity.

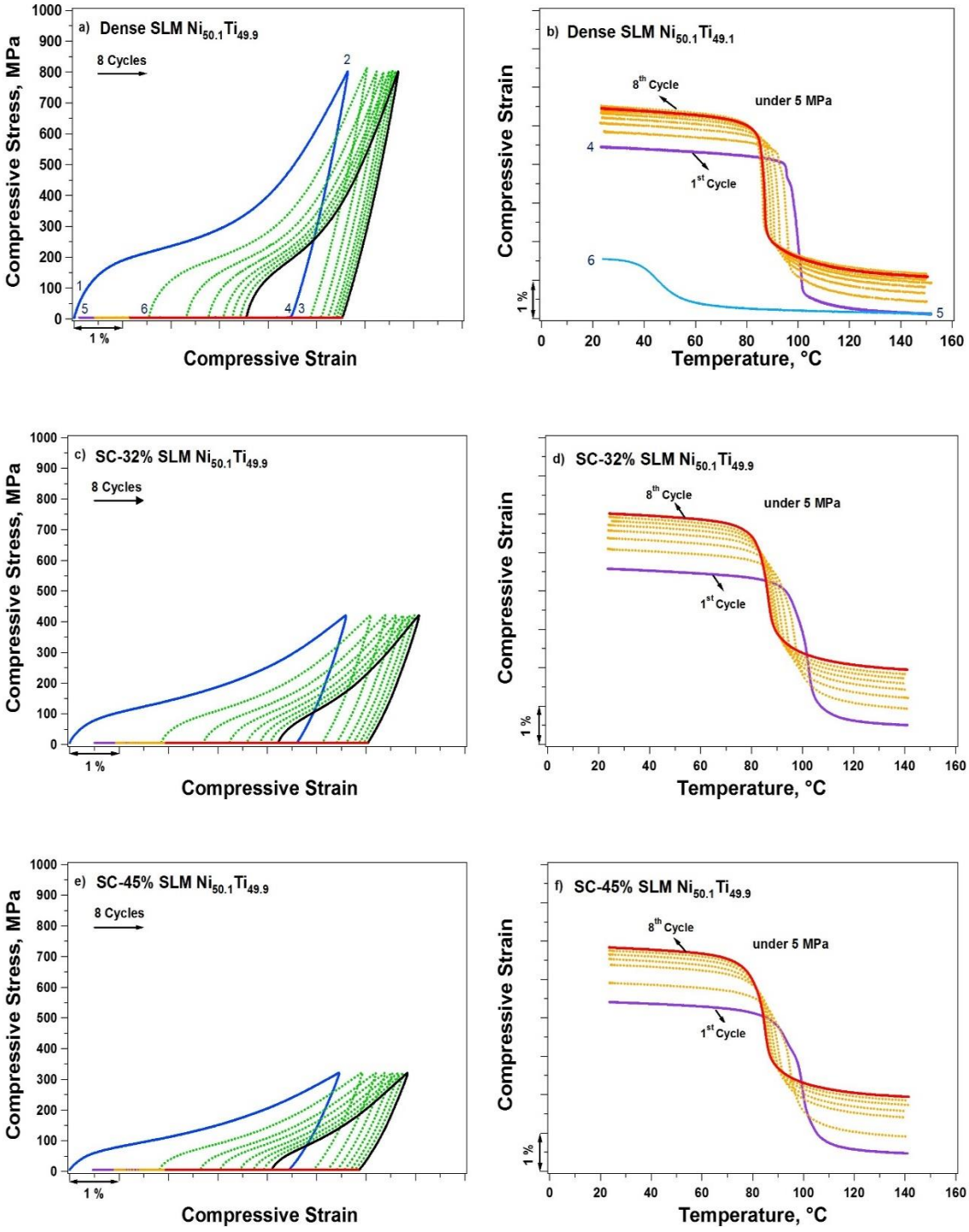

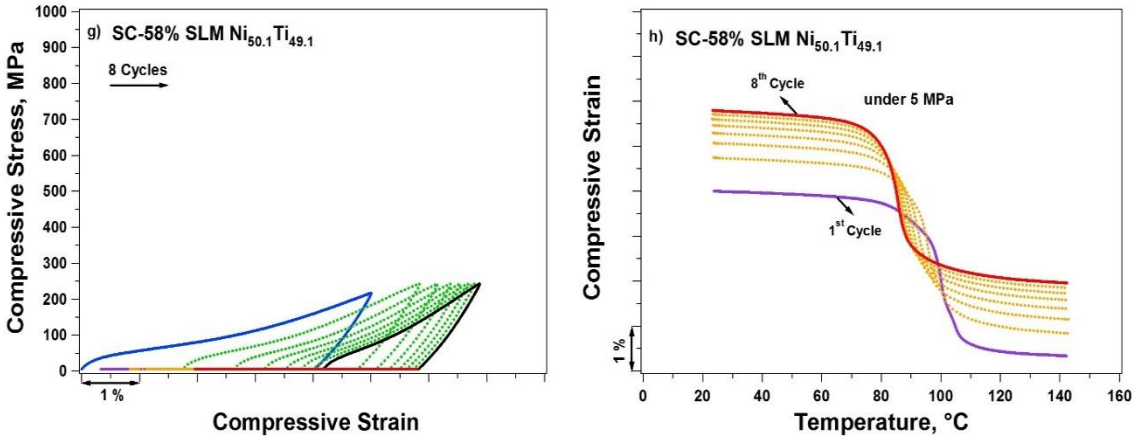

Figure 7-7 (a), (c), (e), (g) Stress-strain curves of cycling tests of Dense, SC-58, SC-45 and SC-32 SLM $Ni_{50.1}Ti_{49.9}$, (b), (d), (f), (h) The heating procedure of the same experiment to above A_f after unloading

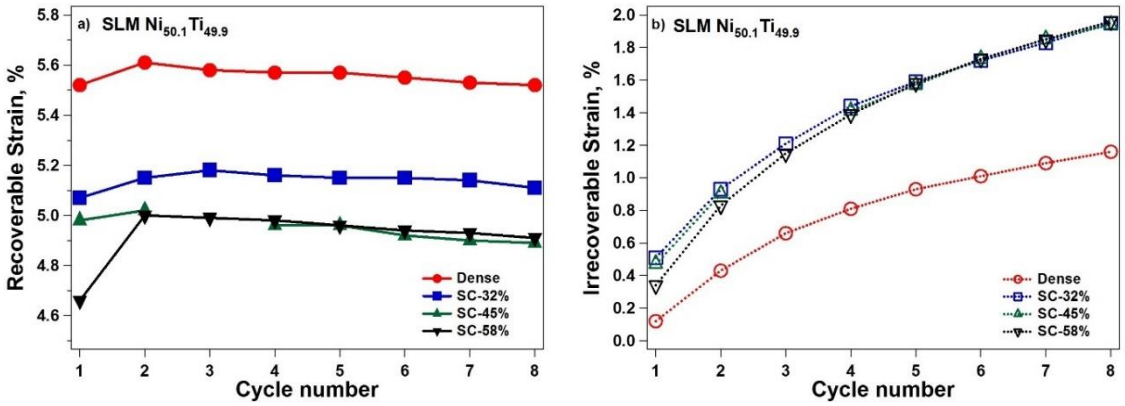

Figure 7-8 The change of (a) ε_{rec} and (b) ε_{irr} with cycling of dense, SC-58, SC-45 and SC-32

Figure 7-9 shows the shape memory effect of BCC and BCC-Z porous samples. According to the failure tests the maximum stress levels for cycling experiments of BCC and BCC-Z were determined. Consequently, BCCZ and BCC loaded up to 90 and 50 MPa at 24ºC respectively. After unloading, the samples were heated above A_f to observe shape recovery and cooled back to room temperature for next cycle. In the first cycle, the samples were deformed till 3.8 and 4.8% for BCCZ and BCC, respectively, and fully recovered upon unloading and subsequent heating. The strain curves during heating show that the transformation temperatures slightly reduced in the second cycle. It should be noted that

the maximum applied stresses are very low in BCC and BCC-Z structures due to their higher porosity levels than SC samples.

The maximum residual strain of all samples was decreased with cycling. Because of the porous microstructure of the samples, some portions of the sample may experience higher plastic deformation than others due to stress concentrations. The increased slope during transformation in BCC and BCC-Z samples in comparison with SC structure can be attributed to increased plastic deformation due to variant-variant interaction and dissipation. The slope of transformation strongly depends on the pore morphology, microstructural defects, and martensite morphology.

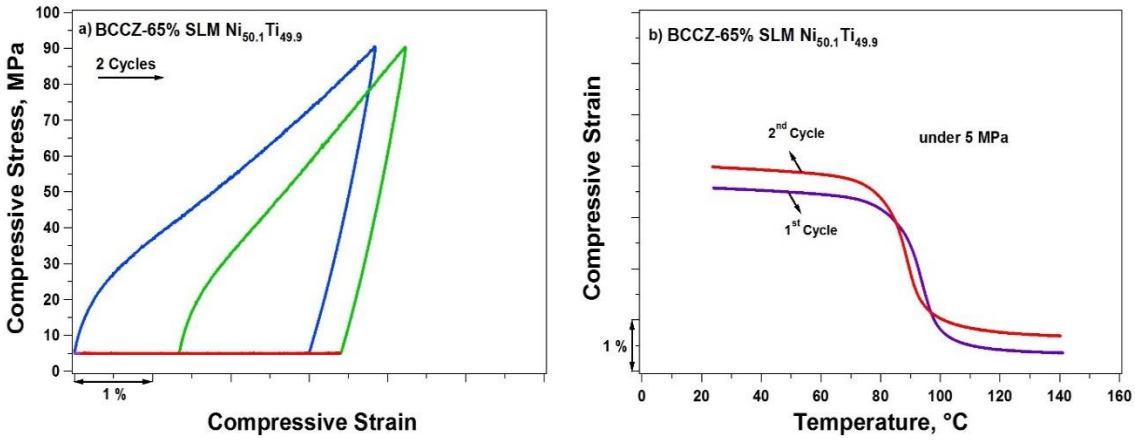

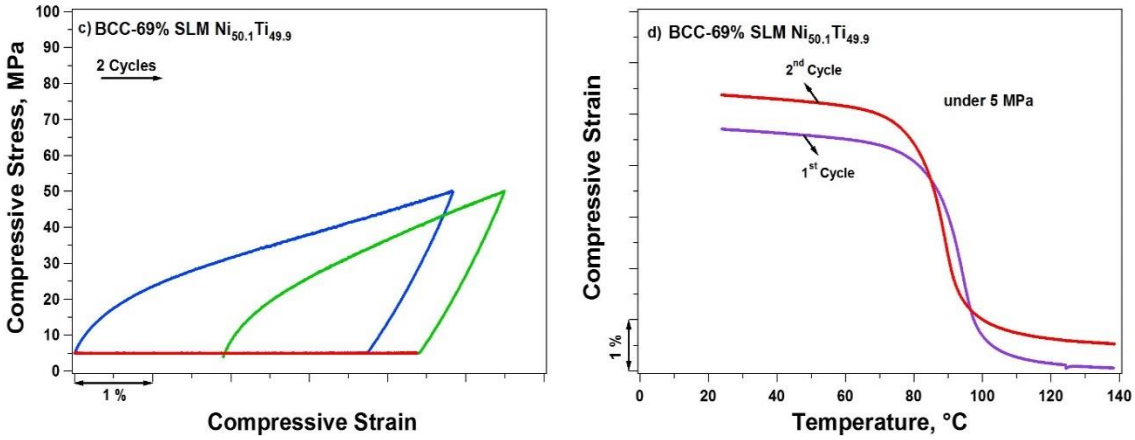

Figure 7-9 (a) and (c) Stress-strain curves for cycling tests, (b) and (d) The heating procedure of the same experiment to above A_f after unloading to 5 MPa. of BCC and BCC-Z,

Elastic modulus, ultimate compressive stress, failure strain, maximum applied stress, ε_{rec}, and ε_{irr} in the first cycle, ε_{rec} in the eight cycle, and total irrecoverable strain ($\varepsilon_{irr,tot}$) are summarized in Table 7-3. The recovery ratio at first cycle was calculated as the ratio of recoverable strain to total strain.

The dense sample exhibited the highest ε_{rec} of 5.52% and lowest ε_{irr} of 1.16 % after eight cycles. SC-32 displayed ε_{rec} of 5.07 % and ε_{irr} of 0.5% in the first cycle. When porosity increased to 58%, the ε_{rec} was 4.66% and ε_{irr} was 0.34% in the first cycle. All the samples showed more than 90% recovery in the first cycle and accumulation of ε_{irr} during cycling. There is a considerable increase in the ε_{rec} in the second cycle for all the samples. After this cycle the ε_{rec} is leveled and then declined with increased cycle number (Figure 7-8 (a)). After cycling, all porous samples showed stabilized shape memory effect with recoverable strain of 5 %. The dense sample has the highest elastic modulus of 69 GPa, and the modulus decreased by increasing the level of porosity.

Table 7-3 Summary of stress-strain curves of cycling tests of Dense, 58%, 45% and 32% porosity SLM $Ni_{50.1}Ti_{49.9}$

SLM $Ni_{50.1}Ti_{49.9}$	Elastic Modulus, (GPa)	Ultimate Comp. Stress, (MPa)	Failure Strain, %	Max Stress Level for cycling, (MPa)	1st Cycle			Last Cycle	
					Irrec. Strain,%	Rec. Strain,%	Recovery Ratio, %	Rec. Strain,%	Total Irrec. Strain,%
Dense	69.0	1619	30.2	800	0.12	5.52	97.8	5.52	1.16
SC-32	41.2	1035	28.3	420	0.51	5.07	90.8	5.11	1.95
SC-45	30.0	728	24	320	0.47	4.98	91.3	4.89	1.94
SC-58	20.5	410	15.6	240	0.34	4.66	93.2	4.91	1.96
BCC-Z	16.5	187	13.6	90	0	3.4	100	3.3	0
BCC	5.97	63	10.5	50	0	5.8	100	5.8	0

7.2.5 Summary and Conclusion

Selective laser melting was used to produce dense and porous near equiatomic NiTi parts, and thermo-mechanical tests were conducted to characterize the mechanical and shape memory properties. In addition to the dense sample, five porous samples with different level of porosity from 32% to 69% with two different structures were characterized. Transformation temperatures decreased slightly (about 10-14ºC) after SLM, which was attributed to composition change and picked up impurities. The superelastic response of the SLM fabricated near equiatomic NiTi showed only partial recovery. This is also true for conventional NiTi since equiatomic NiTi does not have high enough strength to display full strain recovery. The dense and porous samples showed a good shape memory effect and functional stability. Dense SLM NiTi recovered almost entirely while

less than 0.5% irrecoverable strain remained in porous samples. At the end of cycling tests, SME behavior stabilized, and their irrecoverable strain was negligible.

Mechanical properties of samples such as elastic modulus and ductility of the SLM fabricated NiTi samples found to be highly porosity level and pore structure dependent. It was shown that it is feasible to decrease the Young modulus of the samples up to 86% by increased porosity and still retain the shape memory effect of SLM fabricated samples.

7.3 Thermo-Mechanical Response of Porous SLM $Ni_{50.8}Ti_{49.2}$

In addition to bone-matched stiffness, it is desirable to maintain and enhance the superelasticity behavior of porous NiTi structures. As explained in section 1.2.4 superelasticity takes place as a result of stress-induced martensitic transformation during loading and subsequent reverse transformation upon unloading. The phenomena occur only at a specific temperature range which is higher than austenite finishing temperature, A_f. Binary NiTi alloys have the TTs typically between -40˚C and 100 ˚C and show a temperature hysteresis of 20–40 ˚C [29-31]. It was also discussed in section 1.3.1 that with having slightly higher Ni content in NiTi alloys, it is possible to dramatically decrease the TTs of the alloys (about 93 °C/at% with Ni content) [32]. Moreover, it is more likely for Ni-rich NiTi alloys to show superelasticity since they have the higher intrinsic strength and can be precipitation hardened with heat treatments (Section 1.3.2). Therefore, proper aging is extremely important for precipitation characteristics and the corresponding shape memory properties.

In chapter 4, it was shown that SLM fabricated NiTi shows very similar functional properties to the conventional NiTi. The chapter 5, and 6 showed with proper aging, strain recovery of up to 5.5% with a recovery ratio of 95% can be achieved. However, for

biomedical applications, it is essential to have the superelastic response at body temperatures. So far, no work has been conducted to enhance superelasticity behavior of porous SLM NiTi structures exclusively at body temperatures for orthopedic implant applications. In this experimental section, dense as well as porous SLM fabricated NiTi structures with porosity levels ranging from 32% to 58% are considered to cover the stiffness range of cortical bone, and, therefore, minimize the risk of stress shielding for biomedical implants. After an appropriate heat treatment, the shape memory effect, superelastic and cyclic response of dense and porous SLM NiTi parts are experimentally investigated t in target temperatures.

7.3.1 Morphology

Figure 7-10 shows the fabricated porous samples. Also, a dense rectangular (with zero porosity) included for comparison. Figure 7-11 (a)-(d) show the cross-section images of dense, 32%, 45%, and 58% porous SLM fabricated samples, respectively.

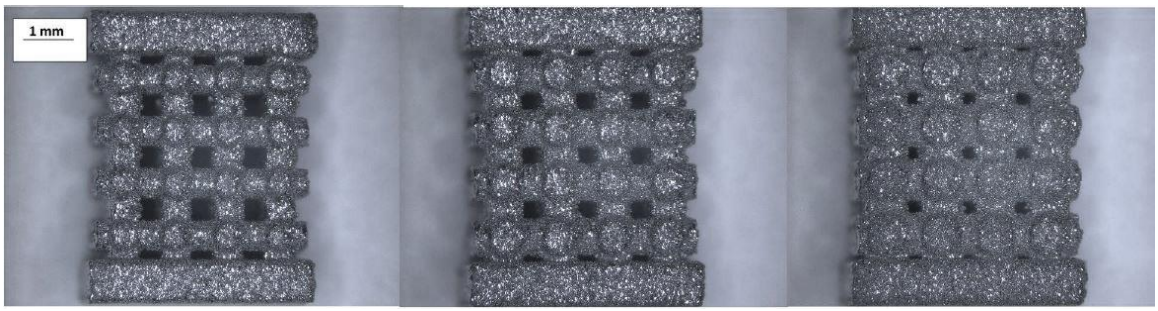

Figure 7-10 SLM fabricated NiTi parts. From left to right, parts have porosities of 58%, 45%, and 32%.

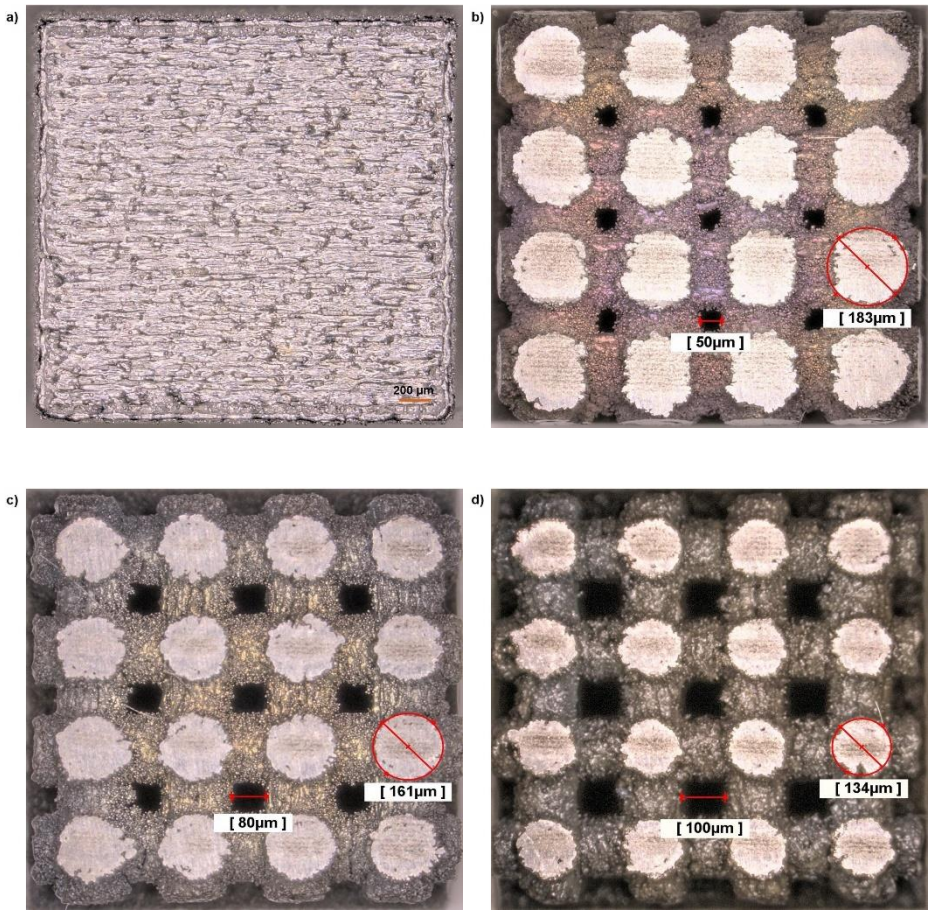

Figure 7-11 Optical micrographs of cross section of (a) dense, (b) 32%, (c) 45%, and (d) 58% porous SLM fabricated $Ni_{50.8}Ti_{49.2}$

Porous parts were generated by repeating identical unit cells in *x*, *y*, and *z* directions. The unit cell consisted from four struts that intersect at the midpoint, which is called Simple Cubic (SC) unit cell. It is visible that pore size gets larger as the porosity level increases. The pore distribution is uniform with a pore diameter of 50 µm, 80 µm, and 100 µm for 32%, 45%, and 58% respectively. Three important porosity parameters are strut-diameter (D), midpoint cell length (L), and the number of repeating unit cells along each direction [189]. The horizontal D is 1.4 mm, 1.2 mm and 1.0 mm for 32%, 45% and 58% porosities, respectively. The L was constant at 2 mm and $4 \times 4 \times 4$ number of each cell was repeated for all the porous samples in order to fabricate the whole part.

7.3.2 TTs Adjustment

Figure 7-12 illustrates the typical DSC curves of SLM fabricated $Ni_{50.8}Ti_{49.2}$ in as-fabricated, solutionized and 350˚C-15 min aged conditions. The time and temperature have been selected based on a previous aging study in chapter 5. The as-fabricated condition has broad transformation peaks with A_f of 32˚C, meaning that the sample can be mixed phased at room temperature. Solution annealed sample has sharper peaks and its TTs shift to lower temperatures with -11 ºC and 12ºC for M_s and A_f, respectively. After aging the TTs were decreased once again and the M_s and A_f temperatures were found to be -17 ºC and 7ºC, respectively. The reason of change in TTs after solutionization and aging has been discussed thoroughly in previous chapters. The forward transformation shows a wavy and broad peak while the backward transformation happens with a sharp peak. The A_f of aged sample is 6˚C, thus it is austenite at room and body temperature.

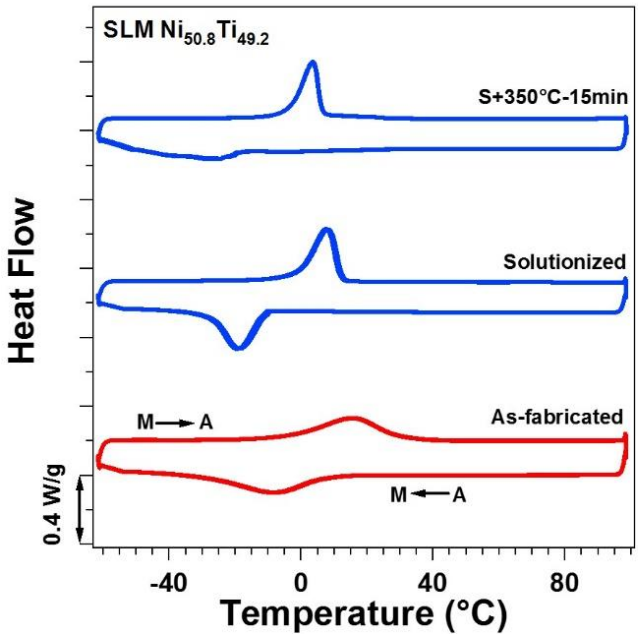

Figure 7-12 DSC curves of SLM $Ni_{50.8}Ti_{49.2}$ in as-fabricated, solutionized and aged conditions

7.3.3 Thermal Cycling under Stress of Porous SLM $Ni_{50.8}Ti_{49.2}$

Figure 7-13 (a)–(d) show the thermal cycling under constant compressive stress responses of 300C-15min aged dense, 32%, 45%, and 58% porous SLM NiTi, respectively. In each cycle, compressive stress was applied at a temperature above $A_{f,}$ and the sample was cooled to below M_f to fully transform to martensite and then heated up again to above A_f. The applied stress was kept constant during each cycle and successively increased for the next thermal cycles until the maximum transformation strain was obtained. All the samples showed shape memory effect and their TTs were increased with increasing the compressive stress. Figure 7-13 indicates a clear connection between applied stress and strain recovery with the level of porosity since the irrecoverable strain has increased with porosity level at the same stress level. Figure 7-13 (a) shows that dense sample had a full recovery after 300 MPa and an irrecoverable strain of 0.6% was observed after 400 MPa. Figure 7-13 (b) and Figure 7-13 (c) indicate that irrecoverable strain was firstly observed at 200 MPa for 32% porous sample and at 100 MPa for 45% porous sample. The 58% porous sample showed the highest irrecoverable strain of 0.37% under 100 MPa. The irrecoverable strains were 0.8%, 1.75% and 2.5 % for the 32%, 45% and 58% porous samples, respectively, under 200MPa. It should be noted that recoverable strain was increased initially with stress and then dropped at higher stress while total strain always increased with stress for all samples.

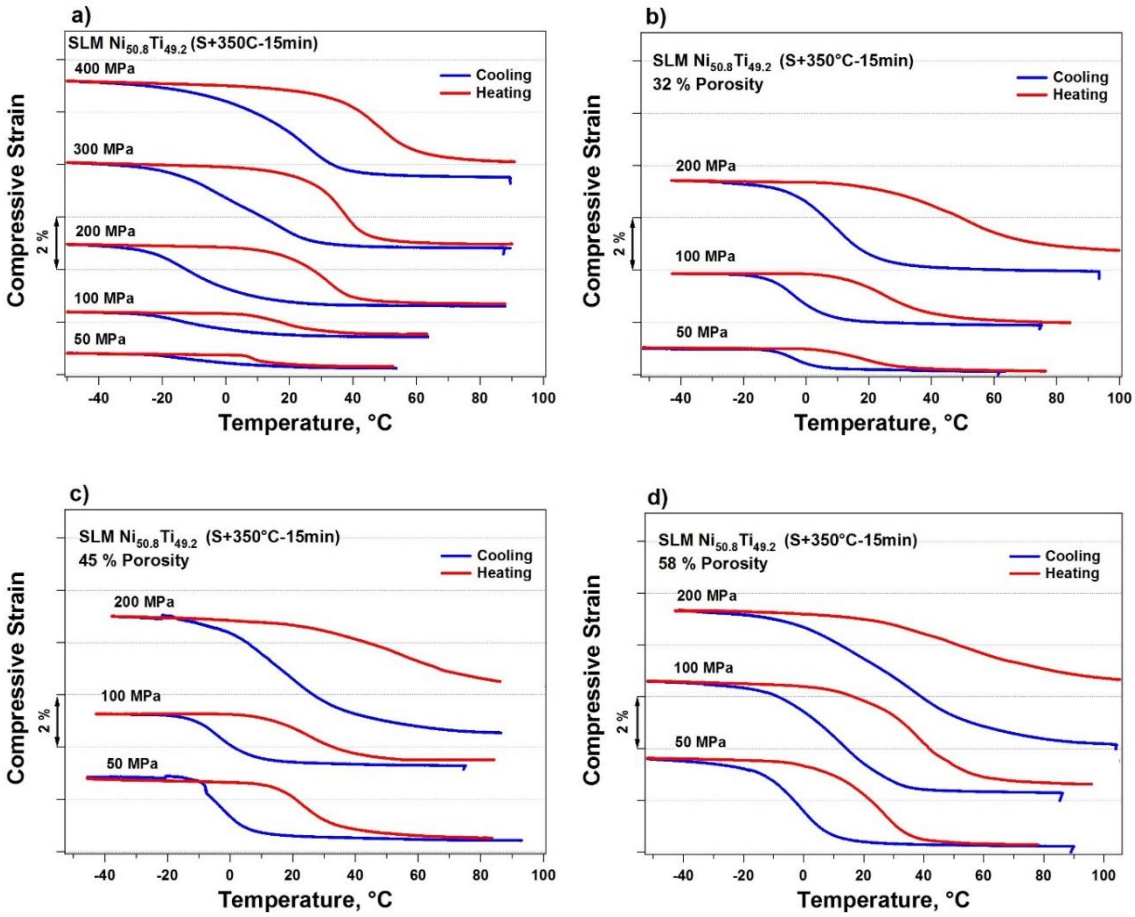

Figure 7-13 Thermal cycling under stress of (a) Dense, (b) 32% porous, (c) 45% porous, and (d) 58% porous SLM $Ni_{50.8}Ti_{49.2}$

For better comparison, Figure 7-14 (a) depicts the recoverable and irrecoverable strains of all samples as a function of porosity level which were extracted from Figure 7-13 for two highest stress levels (100 and 200 MPa). Recoverable strain was increased with porosity but began to decrease or level for higher porosities while the irrecoverable strain starts to appear as the porosity level was evolved since their strength decreased drastically. Figure 7-14 (b) presents the ratio of recoverable strain to total strain as a function of applied stress. The recovery ratio for all samples regardless of their porosities decrease with applied stress level. However, the decreasing trend is drastic when the porosity is too high. For instance, the 99% recovery ratio of the dense sample, drops to only 52% for the 58% porous

sample under 100 MPa. Since the dense sample is stronger, the 95% recovery can be achieved even under 300 MPa. When porous samples are compared, the decreasing trend of recovery ratio for 32% and 45% porous samples displays a sharp fall in higher than 100 MPa while it happens between 50 to 100 MPa for 58%.

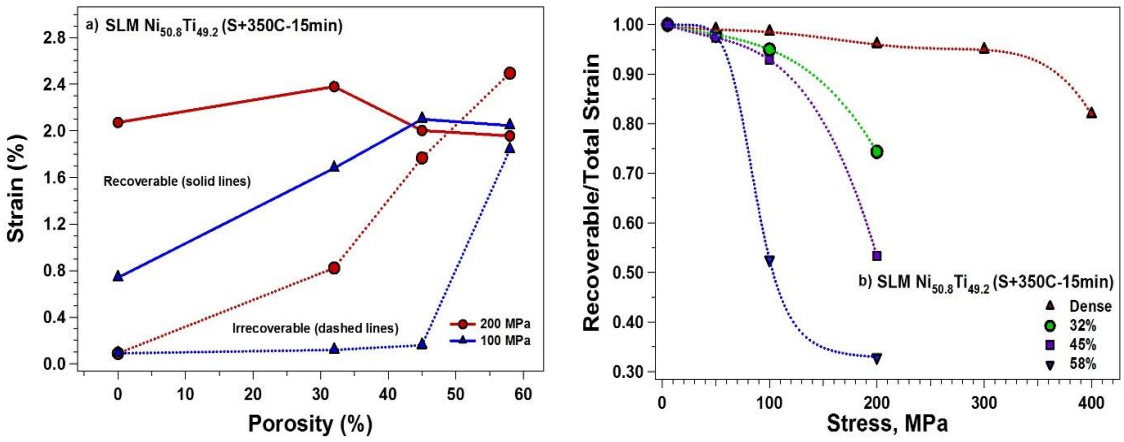

Figure 7-14 (a)Recoverable and irrecoverable strain as a function of porosity, (b) Recovery ratio of dense and porous SLM $Ni_{50.8}Ti_{49.2}$ as a function of applied stress

7.3.4 Superelasticity of Porous SLM $Ni_{50.8}Ti_{49.2}$

Figure 7-15 illustrates the stress–strain responses of the dense aged SLM $Ni_{50.8}Ti_{49.2}$ alloys from 10 ºC to 50 ºC. The specimen was loaded up to 3% strain and then unloaded, followed by heating to a temperature beyond A_f. The same procedure was repeated as the testing temperature was increased by 10 °C. The dense sample showed full strain recovery of 3% in the temperature range of 20-40 ºC. Superelastic testing at 50ºC resulted in a small remnant strain of 0.3% in which further strain of 0.18 % is recovered with subsequent heating indicating the formation of retained martensite.

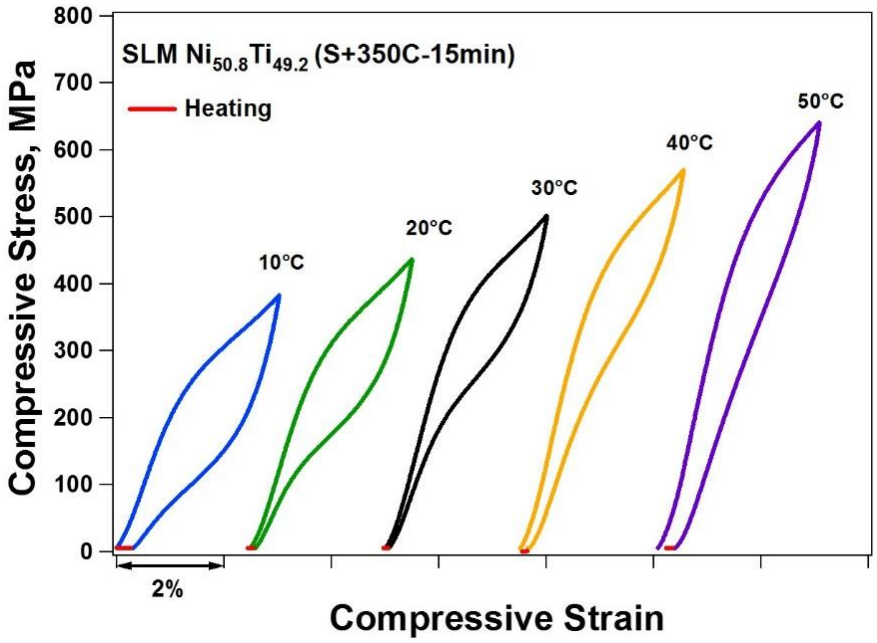

Figure 7-15 Temperature dependent stress-strain curves of aged (S+350C-15min) SLM $Ni_{50.8}Ti_{49.2}$

Figure 7-16 (a) and Figure 7-16 (b) are the incremental superelasticity experiments of the dense samples at 24 ºC and 37ºC. The samples were loaded from 2% up to 6% and then unloaded. Figure 7-16 (a) shows that dense sample could fully recover the total strain of 4% at room temperature. Even after loading till 6%, the total recoverable strain was 5.65%. Likewise, sample recovered almost fully up to 4% at 37ºC (Figure 7-16 (b)). After loading till 6%, the irrecoverable strain of 0.375% was observed. These numbers are comparable to dense NiTi parts fabricated with other powder metallurgy methods. For instance, superelastic response with 5% strain at room temperature has been observed for SPS fabricated dense $Ni_{50.9}Ti_{49.1}$ after 320ºC-30min aging [190]. In another study, HIP fabricated dense $Ni_{51}Ti_{49}$ homogenized at 1000C-4hr and aged at 400C-4hr displayed strain recovery of 6.5% at room temperature [168].

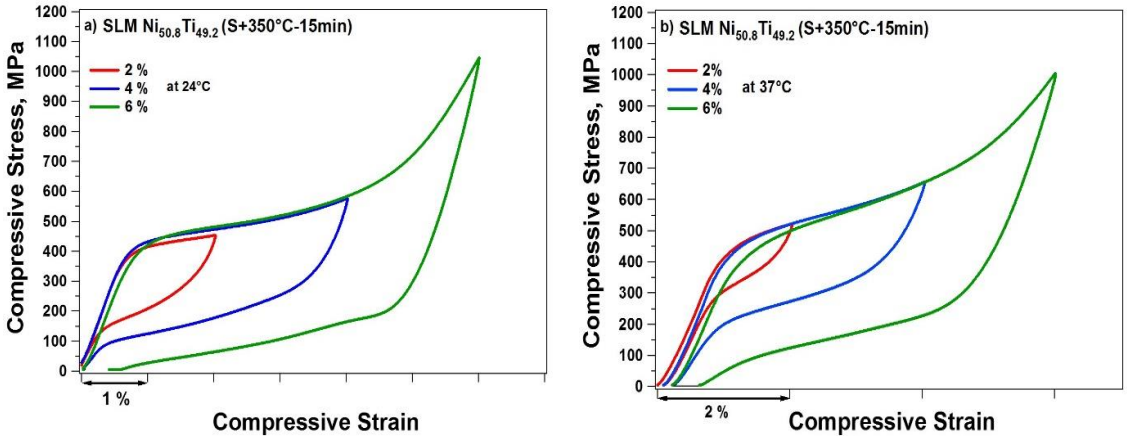

Figure 7-16 Superelastic response of aged (S+350C-15min) dense sample at (a) Room and (b) Body temperatures

To investigate the stability of superelastic responses, cycling tests were conducted at 24 ºC and 37ºC. The same samples were loaded till 800 MPa then unloaded for 10 cycles. After 10 cycles, they were heated up to a temperature above A_f to observe the recoverable strain after cycling. Figure 7-17 (a) and Figure 7-17 (b) display the cycling results for dense at 24ºC and 37ºC. As the number of cycles was increased, the stress hysteresis and irrecoverable strain were decreased and the response was stabilized. After 10 cycles, the stabilized superelastic response of 3.55% and 3.0% were obtained while total irrecoverable strains were 2.17% and 3.6% at 24ºC and 37ºC, respectively. More than 1% of the unrecovered strain was regained through heating indicating remained martensite in the sample and the residual strain due to plastic deformation was not recovered.

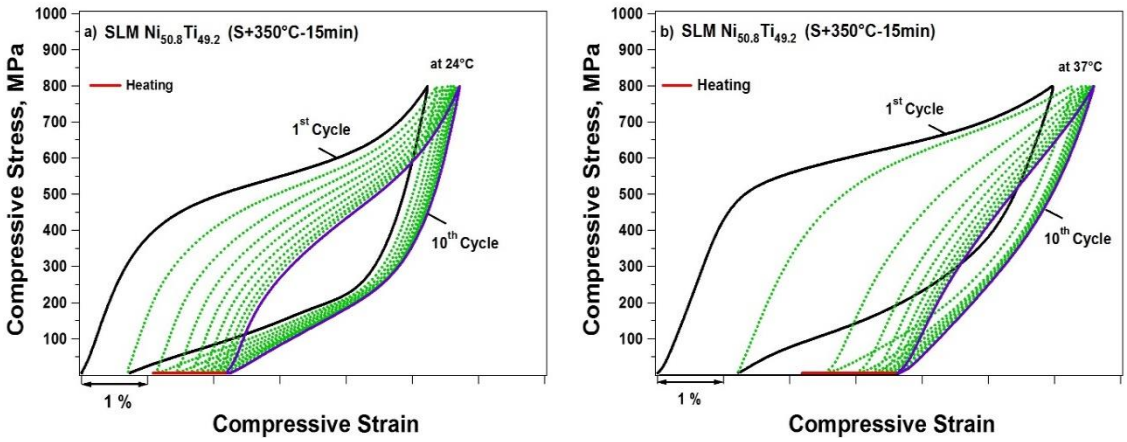

Figure 7-17 Superelastic cyclic response of aged (S+350C-15min) dense sample at a. room, b. body temperatures

Figure 7-18 (a)-(c) are superelastic cyclic responses of porous samples at body temperature. The experiments were carried out with 4% constant strain limit for all test samples. Similar experiments were conducted with considering stress limit for loading. Since for dense sample cyclic tests provided in Figure 7-17, 800 MPa had been selected, therefore 544 MPa, 440 MPa, and 336 MPa stress were applied for 32, 45 and 58% porous samples, respectively. Figure 7-18 (d) shows the experimental result for 58% porous sample with 340 MPa stress limit. Other samples were not presented to avoid repetition. From Figure 7-18 (a) and. (b), both 32% and 45% porous samples with similar behaviors have recovered about 3.5% of the deformation at first cycle after 4% deformation. The last cycle of both experiments showed a full strain recovery of 2.75%. The 58% porous sample demonstrated a poorer response in the first cycle and recovers 2.7%. At 10^{th} cycle, the sample still could show 1.75% superelasticity. The main reason for the good superelastic behavior of the higher density sample is the rather continuous connectivity between adjacent unit cells. The higher porosity in the specimen, either such connectivity is not established or is not uniform, therefore, the superelastic response is diminished. Such

correlation can be found for porous NiTi parts fabricated through other methods. 18%-61% porous $Ni_{50.8}Ti_{49.2}$ was produced with SPS technique were tested at room temperature and superelastic recovery strains of the porous NiTi alloys decreased by increasing the porosities and pore size, while the residual strains increased [191]. In other studies, lower levels of porosities have been considered. 12%-13% porous SPS fabricated dense $Ni_{50.9}Ti_{49.1}$ aged at 320ºC for 30min has been reported to show up to 5% superelasticity [190, 192]. 16% porous HIP fabricated $Ni_{51}Ti_{49}$ homogenized at 1000C-4hr and aged at 400C-4hr demonstrated 3 and 6% strain recovery after 4 and 8% deformation, respectively [168]. In a different study, 27% porous HIP fabricated $Ni_{50.8}Ti_{49.2}$ (aged at 450C- 30 min) were cyclically loaded at different strain levels [193]. About 4% strain recovery has been observed which similar to presented results in this work, the highest irrecoverable strain was found in the first cycle where the response stabilizes with further cycling along with degradation. The superelastic response of 30%-40% porous CS and HIP fabricated $Ni_{50.8}Ti_{49.2}$ (heat treated at 1050ºC-5hr and 450C-30 min) has been compared by Yuan, et al [194]. While 2% irrecoverable strain has been seen after 4% deformation for CS sample, HIP sample has shown a significant improvement with only 0.3% irrecoverable strain udder similar deformation. MIM produced 51% porous $Ni_{50.6}Ti_{49.4}$ has shown more than 3.5% recovery after 4% deformation at body temperature [195]. Again MIM produced 61% porous $Ni_{50.8}Ti_{49.2}$ (aged at 500C-1hr) has shown only partial recovery at body temperature while A_f temperature was 60ºC [196].

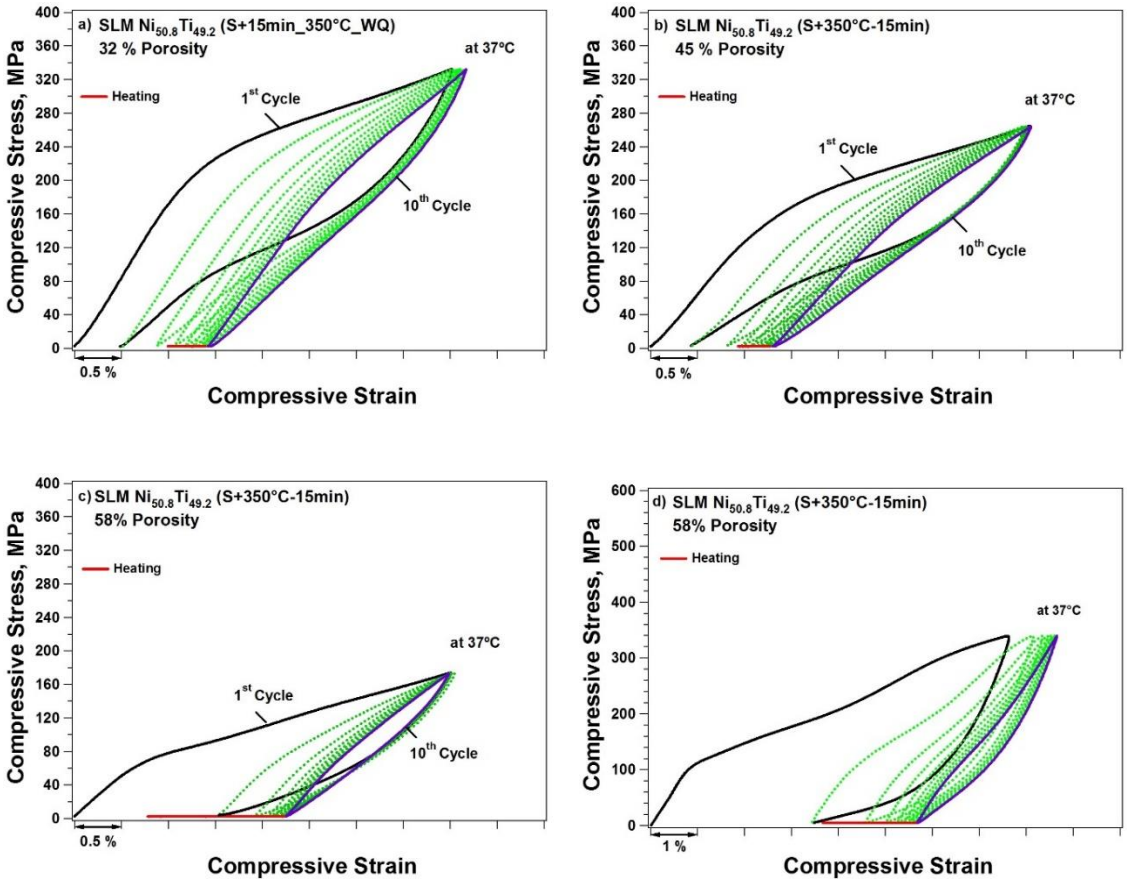

Figure 7-18 Superelastic cyclic response of 32%, 45%, and 58% porous SLM $Ni_{50.8}Ti_{49.2}$ at body temperature (a)-(c) with strain limit and (d) with 4% stress limit

As mentioned the compressive strength and the Young's modulus mismatch between NiTi and bone have been one of the remaining problems during the previous year's preventing in vivo experiments for bone implants. Table 7-4 displays the Young's modulus and critical stress for plastic deformation of test samples at 37ºC. The information regarding critical stress for plastic deformation has been extracted from loading of the samples to higher stress levels, e.g., Figure 7-18 (d). The table indicates that elastic modulus of dense SLM NiTi drops from 44.2 GPa to 9.4 GPa by adding 58% porosity. The decrease is roughly 80%. The stiffness of NiTi structure can be tailored to the stiffness level of the compact bone (<20 GPa) with only 32% porosity. This stiffness matching can

avoid bone resorption and local weakness that usually occurs due to stress shielding between bone and the implant materials. In addition, critical stress for plastic deformation decreases with porosity as expected due to the existence of larger stress concentration for higher porosities. However, the critical stress of the porous SLM NiTi alloys which ranged from 300 to 1224 MPa is still well above the compression strength of human cortical bone (100–230 MPa) [197].

Table 7-4 Table 1: Variation of young modulus and plastic deformation of SLM $Ni_{50.8}Ti_{49.2}$ with porosity at body temperature

Porosity (%)	0	32	45	58
Young's Modulus(GPa)	**47**	**18**	**13**	**9**
Plastic Deformation(MPa)	**1224**	**503**	**398**	**305**

Figure 7-19 shows stabilized superelastic response and accumulated irrecoverable strain with cycling extracted from Figure 7-18 (a)-(c). It should be kept in mind that to deform samples up to 4% they have been loaded to different stress levels. Therefore, samples have been loaded 335 MPa, 265 MPa, 175 MPa with respect to their porosities. Regardless of porosity level, samples have exhibited similar characteristics and accumulated strain increased and then suppressed. The increase is more pronounced and steep in early cycles and not significant in last ones which can be referred to the high irrecoverable strain at first cycles. As the superelastic response stabilizes the irrecoverable strain decreases. It is noteworthy that there is a slight difference in irreversible strain of 32% and 45% samples at first cycle. The same trend has been continued in the rest of cycles. In contrast, the 58% porous sample shows significantly higher irrecoverable strain

at first cycle. It seems that porosity higher than 50% drastically lowers the strength. However, similar accumulation characteristic with cycling is observable. It can be perceived that training can greatly improve the superelastic response.

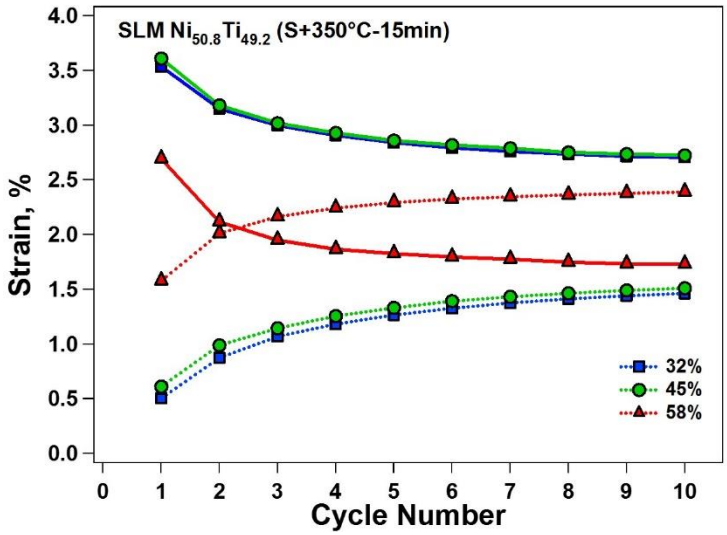

Figure 7-19 Stabilized recovery (solid line) and accumulation of irrecoverable strain (dashed line) during cycling tests for 32%, 45%, and 58% porous SLM $Ni_{50.8}Ti_{49.2}$ at body temperature

7.3.5 Modeling and Simulations

The superelastic responses of porous NiTi samples were further simulated numerically by the finite element method (FEM) using 3D constitutive model [198] implemented into commercial program Abaqus 6.14. At first step, the experimental and simulation results for a dense sample at body temperatures was evaluated. As can be seen from Figure 7-20 the simulation results are seen in a very good agreement with the experimental findings.

As illustrated in Figure 7-21 (a), a porous structure was consisted of repeating the unit cell in all *x*, *y*, and *z* directions. The geometry of unit cell model of the porous structures was consisted of three orthogonal struts, intersecting at the mid-point. To minimize the simulation cost a proper unit cell as shown in Figure 7-21 (b), had been constructed for

each porous structures and utilized in FEM analysis. The porosity level was formulated by the ratio of the diameter to the length of a strut. Symmetric periodic boundary conditions were defined and the nominal stress was calculated by dividing the axial force with the projected area of the unit cell on the plane normal to the loading direction.

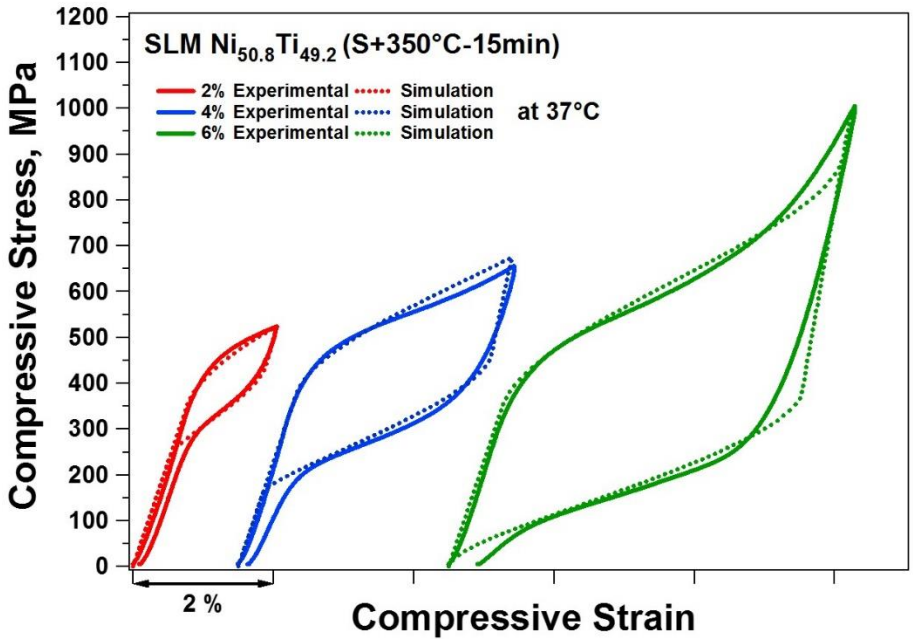

Figure 7-20 Comparison of experimental (solid line) and simulation (dashed line) of dense SLM $Ni_{50.8}Ti_{49.2}$ at body temperature

(a)

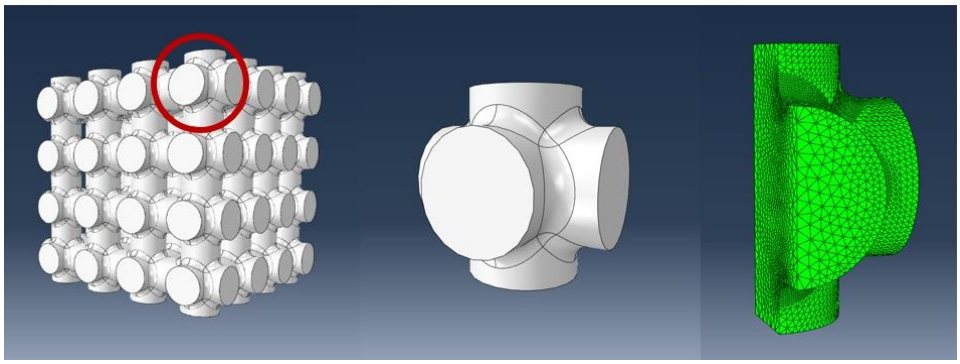

(b)

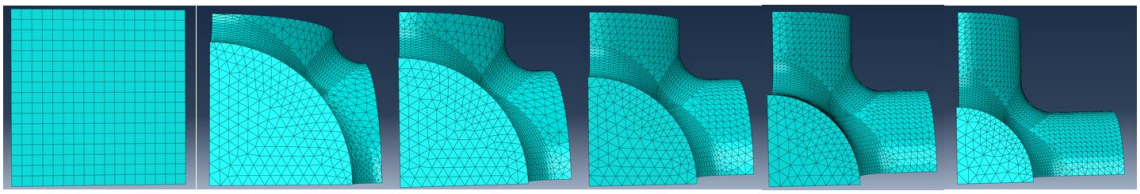

Figure 7-21 (a) The geometry and unit cell model for a 45% porous NiTi alloy and (b) The unit cell FE models for all dense and porous NiTi alloys (20%, 32%, 45%, 58%, and 71%).

The material parameters of the dense and porous parts including the modulus of martensite and austenite, TTs, and critical transformation stresses were extracted from 10th cycle of the experimental results at body temperature (from Figure 7-18) and used for the simulations. Table 7-5 Summary of Material Properties of SLM NiTi in 10th cycle, used for FE simulationsummarizes the material parameters used in the FE analysis.

Table 7-5 Summary of Material Properties of SLM NiTi in 10th cycle, used for FE simulation

Austenite Modulus E_A (GPa)	Martensite Modulus E_M (GPa)	γ_A, γ_M	Critical stress-martensite start σ_{Ms} (MPa)	Critical stress-martensite finish σ_{Ms} (MPa)	Critical stress-austenite start σ_{As} (MPa)	Critical stress-austenite finish σ_{Af} (MPa)
36	**56**	**0.3**	**220**	**900**	**520**	**0**

Figure 7-22 depicts the comparisons of experimental and simulated superelastic responses of dense and porous samples. The predictions for NiTi alloys with 20% and 71% porosities have been included as well. Simulations and experiments showed similar trends in stiffness reduction as the percentage porosity increased. The agreement between simulation results and experimental indicates that properties of SLM NiTi can be further

tailored with introducing porosity to the parts as well as engineering the geometry and level of porosity.

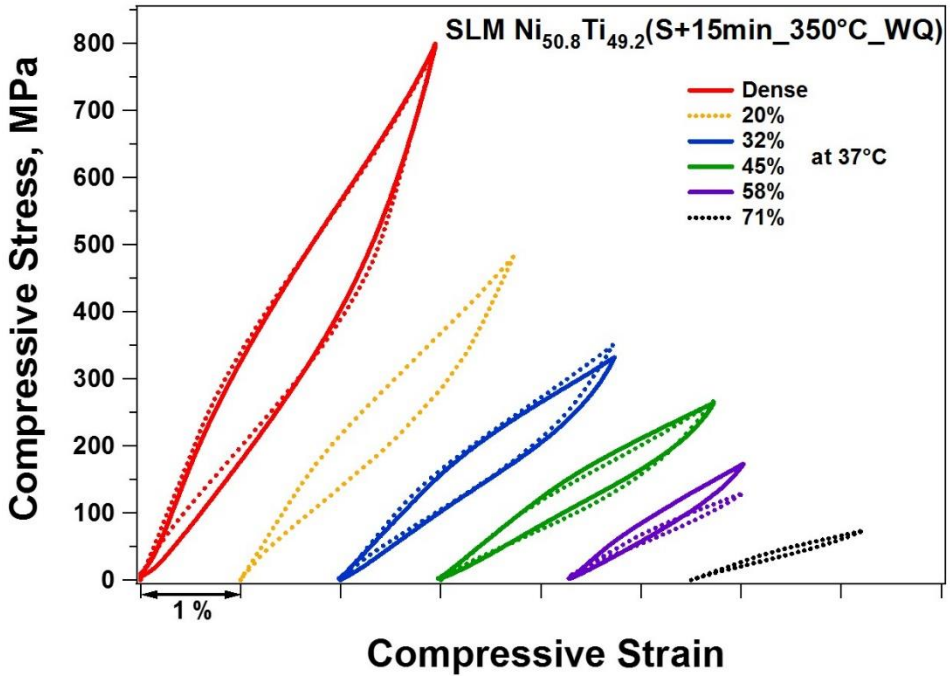

Figure 7-22 Compression of 10th cycle of experimental results (solid line) and simulation (dashed line) for SLM $Ni_{50.8}Ti_{49.2}$ at body temperature) with different porosities

7.3.6 Summary and Conclusion

Porous NiTi scaffolds are more favorable than almost any other biocompatible metallic scaffolds due to their unique bone-like properties including low stiffness and Superelasticity behavior. This section had focused on the techniques to enhance superelasticity properties within porous NiTi structures. Selective Laser melting (SLM) method was employed to fabricate dense and porous Ni-rich NiTi structures with different level of porosities (32-58%). Subsequently, proper heat treatment (solution annealing+ aging at 350ºC for 15 mins) was applied on the samples. Particular attention was given to the superelasticity and cyclic response at body and room temperatures. The thermo-

mechanical and mechanical properties of structures were determined as functions of temperature and stress. The conclusions of this study are reported here:

- Thermal cycling under constant stress experiments proved that SLM porous sample can show proper shape memory effect under stress. The dense sample showed almost full recovery under stress up to 300MPa. 32% and 45% porous samples showed greater than 90% recovery ratio under stress up to 100MPa.
- The SLM NiTi alloys displayed a perfect superelastic loop covering both room and body temperatures after adjusted thermal treatment. The dense SLM NiTi can fully recover up to 4% strain at room and body temperatures. After 6% deformation, 5.65% strain recovery was observed.
- The superelastic response of porous samples was examined at body temperature. 32% and 45% porous samples with similar behaviors, recovered 3.5% of 4% deformation at first cycle. The last cycle of both experiments showed a full strain recovery of 2.75%. The 58% porous sample demonstrated a poorer response in the first cycle with 2.7% strain recovery. At the 10^{th} cycle, the sample still could show 1.75% superelasticity. The good superelastic behavior of the higher density samples was attributed to the higher mechanical strength and continuous connectivity between adjacent unit cells.
- The superelastic recovery strain ratio of the porous NiTi alloy could be improved significantly through training. This enhanced superelasticity will greatly degrade the mechanical mismatch between bones and porous NiTi. Furthermore, with increasing the porosity and pore size, elastic modulus and compressive strength of the porous NiTi alloys decreased.

- Simulation results showed a perfect agreement with experimental findings which suggests that modeling can be implemented to predict behavior of NiTi parts with a variety of porosity level and geometry.
- The unique combination of inter-connected pore characteristics, low elastic modulus, high strength and large superelastic recovery strain makes SLM NiTi a good candidate for ideal long-term load-bearing hard tissue implants. In addition, according to the provided results, mechanical properties of porous NiTi alloys are directly related to the pore characteristics, and it can be well designed and controlled by SLM method which opens a promising window for future works.

8 Chapter Eight: Conclusions and Future Work

8.1 Conclusions

The traditional NiTi fabrication methods are challenging and not flexible for producing porous and complex structures Additive manufacturing is an attractive method for overcoming these problems. The combination of such fabrication flexibility with unique NiTi properties such as superelasticity and shape memory effect, makes SLM NiTi parts promising candidates for employment in numerous applications. It has been well documented that fabrication routes affect the functional properties of NiTi alloys.

In this study, a detailed investigation was carried out on the shape memory response, transformation temperature and microstructure of selective laser melting fabricated NiTi. The effects of SLM process parameters such as laser power, scanning speed, and hatch spacing was studied on thermomechanical behavior of NiTi parts. It was shown that the selection of the right process parameters can improve the mechanical response of the final products. It was concluded that adjustment of each of these parameters individually results in densification, chemical composition, crystallographic structure, grains size, and shape, formed secondary phases, TTs, hardness, and finally mechanical response alterations. The energy level was found to have an important role on the densification of the SLM fabricated components. To fabricate fully dense parts either high laser power should be combined with high scanning speed or low laser power with a low scanning speed. TTs of fabricated parts were found to be different and an increasing trend as a function of energy level was observed. High energy level driven through low laser power and low scanning speed seems the most favorable for SLM fabrication of NiTi in terms of mechanical response. 5.77% superelasticity with more than 95% recovery ratio was obtained in as-fabricated condition

for SLM NiTi fabricated by 100W laser power and 125 mm/s scanning speed. The same sample showed 5.5% stabilized strain recovery after 10 cycles. The sample with 250 w laser power and 1500 mm/s scanning speed displayed a poor mechanical response with only 48% recovery ratio, proving the importance of selecting right process parameters for SLM. It was presented that samples with same energy levels but fabricated by different parameters did not show similar behavior which indicates a combination of all involved parameters should be investigated to find the optimum process window for NiTi SLM fabrication. The gran size and microstructural features showed a dependence on employed hatch spacing. Decreasing the hatch spacing improved the hardness and mechanical results substantially.

It was found that the SLM grain growth mechanism is very similar to welding technology and the preferential growth direction for NiTi alloy is [001]. Therefore, after directional solidification at each layer, with epitaxial grain growth, the [001] direction becomes the major direction of the grains after several layers. The intensity of the orientation was found to extend as a function of the energy level of fabrication.

In this study shape memory response of SLM fabricated was compared to the initial ingot as well. It was shown that low energy $Ni_{50.8}Ti_{49.2}$ in as-fabricated condition shows good shape memory behavior and partial superelasticity without any post treatment. Solutionizing was presented as a solution to increase the strength of the material which improved the superelasticity and superelastic window (according to observed CC slopes) and resulted in 3% full recovery at 5ºC. The failure experiment showed a drastic decrease in ductility of the sample after SLM process which was attributed to the different grain structure of SLM sample. TTs of the Ni-rich NiTi alloy were increased after SLM

fabrication. The increase can be attributed to several reasons like Ni evaporation, formed secondary phases and/or picked up impurities during the process.

A comprehensive aging study was conducted over as-fabricated and solution annealed SLM $Ni_{50.8}Ti_{49.2}$ to reveal effects of aging time and temperature. For solutionized condition, samples were aged at selected times at 350 °C and 450 °C and their shape memory effect, superelasticity, and transformation temperatures were determined. It has been concluded that aging is very effective method to tailor and improve the shape memory properties. In comparison, 450 °C aged samples did not show as promising superelasticity as 350 °C aged samples. 350 °C-18 h aging displayed almost perfect shape recovery about 5.5% which was more than 95% of the total deformation at 65ºC. The process of solutionizing is challenging. Therefore, a systematic aging study was also conducted over as-fabricated condition. After only 1 h aging at 350ºC, the strength of the sample was increased considerably and transformation strain of up to 4% was observed for when thermally cycled under 300 MPa while the irrecoverable strain of 0.5% had been observed for the as-fabricated SLM sample under the same stress level. It was shown with 1.5 h aging at 600C more than 5.2% strain recovery can be obtained at room temperature. The remarkable superelastic response of the samples which was even higher than theoretical calculations for single crystal $Ni_{50.8}Ti_{49.2}$ was attributed to Ni-rich precipitates formed by aging and the strong [100] texture formed by SLM.

In addition to the dense sample, five porous near equiatomic $Ni_{50.1}Ti_{49.9}$ samples with different levels of porosity from 32% to 69% with two different structures were characterized. Mechanical properties of samples such as elastic modulus and ductility of the SLM fabricated NiTi samples were found to be highly porosity level and pore structure

dependent. It was shown that it is feasible to decrease the Young's modulus of the samples up to 86% by increased porosity. However, since the equiatomic NiTi alloys do not show superelasticity, porous Ni-rich $Ni_{50.8}Ti_{49.2}$ parts with different level of porosities (32-58%) were experimentally evaluated. A proper heat treatment (solution annealing+ aging at 350ºC for 15 mins) was applied on the samples based on the aging study to adjust TTs for biomedical applications. Particular attention was given to the superelasticity and cyclic response at body and room temperatures. 32 and 45% porous samples with similar behaviors, recovered 3.5% of 4% deformation at first cycle. The last cycle of both experiments showed a full strain recovery of 2.75%. The 58% porous sample demonstrated a poorer response in the first cycle with 2.7% strain recovery. At the 10^{th} cycle, the sample still showed 1.75% superelasticity. The better superelastic behavior of the higher density samples was attributed to the higher mechanical strength and continuous connectivity between adjacent unit cells.

8.2 Future work

This work has proved that selection of SLM process parameters dramatically changes the response of fabricated alloys. Also, aging was found to be an extremely effective tool to improve the shape memory response. It was shown how SLM fabrication flexibility can be employed to fabricated porous and complex geometries and retain the unique features of shape memory alloys at the same time. A great time allocation and future works are required to understand every aspect of SLM fabrication and the resultant features of laser fabrication on NiTi SMAs. Some of the very potential future studies can be:

- More detailed microstructure analysis and TEM study of aged and as- fabricated conditions.

- A systematic aging study over SLM NiTi fabricated by high energy density.
- Study of effects of building direction.
- Tensile, torsion, damping and fatigue testing of SLM NiTi.
- Higher porosity levels or verity of other porosity geometries.

9 References

1. Otsuka, K. and C.M. Wayman, *Shape memory materials*. 1999: Cambridge university press.
2. GRENINGER, A.B. and V.G. MOORADIAN, *Strain Transformation in Metastable Beta Copper-Zinc and Beta Copper-Ti Alloys.* AIME TRANS, 1938. **128**: p. 337-369.
3. Kurdjumov, G. and L. Khandros, *First reports of the thermoelastic behaviour of the martensitic phase of Au-Cd alloys.* Doklady Akademii Nauk SSSR, 1949. **66**: p. 211-213.
4. Chang, L. and T. Read, *Plastic deformation and diffusionless phase changes in metals-The gold-cadmium beta-phase.* Transactions of the American Institute of Mining and Metallurgical Engineers, 1951. **191**(1): p. 47-52.
5. Wollants, P., J. Roos, and L. Delaey, *Thermally-and stress-induced thermoelastic martensitic transformations in the reference frame of equilibrium thermodynamics.* Progress in Materials Science, 1993. **37**(3): p. 227-288.
6. Panchenko, E.Y., et al., *Effect of disperse Ti3N4 particles on the martensitic transformations in titanium nickelide single crystals.* The Physics of Metals and Metallography, 2008. **106**(6): p. 577-589.
7. Sehitoglu, H., et al., *Hysteresis and deformation mechanisms of transforming FeNiCoTi.* Mechanics of materials, 2006. **38**(5): p. 538-550.
8. Sehitoglu, H., et al., *Deformation of FeNiCoTi shape memory single crystals.* Scripta materialia, 2001. **44**(5): p. 779-784.
9. Hamilton, R., et al., *Stress dependence of the hysteresis in single crystal NiTi alloys.* Acta Materialia, 2004. **52**(11): p. 3383-3402.
10. Kus, K. and T. Breczko, *DSC-investigations of the effect of annealing temperature on the phase transformation behavior in Ni-Ti shape memory alloy.* Materials Physics and Mechanics, 2010. **9**(1): p. 75-83.
11. Della Gatta, G., et al., *Standards, calibration, and guidelines in microcalorimetry. Part 2. Calibration standards for differential scanning calorimetry*(IUPAC Technical Report).* Pure and applied chemistry, 2006. **78**(7): p. 1455-1476.
12. Lagoudas, D., *Shape Memory Alloys: Modeling and Engineering Applications*. 2008, Springer, New York.
13. Sehitoglu, H., et al., *Compressive response of NiTi single crystals.* Acta Materialia, 2000. **48**(13): p. 3311-3326.
14. Wollants, P., et al., *Thermodynamic analysis of the work performance of a martensitic-transformation under stressed conditions. 2. numerical-analysis.* Zeitschrift fur metallkunde, 1979. **70**(5): p. 298-304.
15. Benafan, O., et al., *Temperature dependent deformation of the B2 austenite phase of a NiTi shape memory alloy.* International Journal of Plasticity, 2013. **51**: p. 103-121.
16. Turabi, A.S., et al., *Experimental Characterization of Shape Memory Alloys.* Shape Memory Alloy Actuators: Design, Fabrication, and Experimental Evaluation, 2015: p. 239-277.
17. Otsuka, K. and X. Ren, *Physical metallurgy of Ti–Ni-based shape memory alloys.* Progress in materials science, 2005. **50**(5): p. 511-678.

18. Contardo, L. and G. Guenin, *Training and two way memory effect in Cu・Zn・Al alloy.* Acta Metallurgica et Materialia, 1990. **38**(7): p. 1267-1272.
19. Šittner, P., et al., *In situ neutron diffraction studies of martensitic transformations in NiTi polycrystals under tension and compression stress.* Materials Science and Engineering: A, 2004. **378**(1): p. 97-104.
20. Shida, Y. and Y. Sugimoto, *Water jet erosion behaviour of Ti-Ni binary alloys.* Wear, 1991. **146**(2): p. 219-228.
21. Oshida Yoshiki , M.S., *Corrosion and biocompatibility of shape memory alloys.* Zairyo-to-Kankyo, 1991. **40**(12): p. 834-844.
22. Li, D., *Wear behaviour of TiNi shape memory alloys.* Scripta Materialia, 1996. **34**(2): p. 195-200.
23. Lin, H., et al., *Wear characteristics of TiNi shape memory alloys.* Metallurgical and Materials Transactions A, 1997. **28**(9): p. 1871-1877.
24. Ryhänen, J., et al., *Biocompatibility of nickel-titanium shape memory metal and its corrosion behavior in human cell cultures.* Journal of biomedical materials research, 1997. **35**(4): p. 451-457.
25. Putters, J., et al., *Comparative cell culture effects of shape memory metal (Nitinol®), nickel and titanium: a biocompatibility estimation.* European surgical research, 1992. **24**(6): p. 378-382.
26. Elahinia, M.H., et al., *Manufacturing and processing of NiTi implants: a review.* Progress in Materials Science, 2012. **57**(5): p. 911-946.
27. Nishida, M., C. Wayman, and T. Honma, *Precipitation processes in near-equiatomic TiNi shape memory alloys.* Metallurgical Transactions A, 1986. **17**(9): p. 1505-1515.
28. Santo Padula, I., et al., *Effect of upper-cycle temperature on the load-biased, strain-temperature response of NiTi.* Metallurgical and Materials Transactions A, 2012. **43**(12): p. 4610-4621.
29. Stoeckel, D., *The Shape Memory Effect-Phenomenon, Alloys and Applications.* Proceedings: Shape Memory Alloys for Power Systems EPRI, 1995: p. 1-13.
30. Buehler, W.J. and F.E. Wang, *A summary of recent research on the Nitinol alloys and their potential application in ocean engineering.* Ocean Engineering, 1968. **1**(1): p. 105-120.
31. Funakubo, H., Kennedy, JB, *Shape memory alloys.* Gordon and Breach, xii+ 275, 15 x 22 cm, Illustrated, 1987: p. 78.
32. Tang, W., *Thermodynamic study of the low-temperature phase B19' and the martensitic transformation in near-equiatomic Ti-Ni shape memory alloys.* Metallurgical and Materials Transactions A, 1997. **28**(3): p. 537-544.
33. Frenzel, J., et al., *Influence of Ni on martensitic phase transformations in NiTi shape memory alloys.* Acta Materialia, 2010. **58**(9): p. 3444-3458.
34. Ma, J., I. Karaman, and R.D. Noebe, *High temperature shape memory alloys.* International Materials Reviews, 2010. **55**(5): p. 257-315.
35. Yoneyama, T. and S. Miyazaki, *Shape memory alloys for biomedical applications*. 2008: Elsevier.
36. Massalski, T.B., et al., *Binary alloy phase diagrams*. Vol. 1. 1986: American Society for Metals Metals Park, OH.

37. Fan, G., et al., *Origin of abnormal multi-stage martensitic transformation behavior in aged Ni-rich Ti–Ni shape memory alloys.* Acta Materialia, 2004. **52**(14): p. 4351-4362.
38. Turabi, A.S., Saedi, S., Saghaian, S. M., Karaca H.E., Elahinia M., *Experimental Characterization of Shape Memory Alloys*, in *Shape Memory Alloy Actuators: Design, Fabrication, and Experimental Evaluation*. 2015, John Wiley and Sons, Inc: Hoboken, New Jersey.
39. Gall, K., et al., *The Influence of Aging on Critical Transformation Stress Levels and Martensite Start Temperatures in NiTi: Part I—Aged Microstructure and Micro-Mechanical Modeling.* Journal of Engineering Materials and Technology, 1999. **121**(1): p. 19-27.
40. Pelton, A.R., J. Dicello, and S. Miyazaki, *Optimisation of processing and properties of medical grade Nitinol wire.* Minimally Invasive Therapy & Allied Technologies, 2000. **9**(2): p. 107-118.
41. Motemani, Y., et al., *Effect of cooling rate on the phase transformation behavior and mechanical properties of Ni-rich NiTi shape memory alloy.* Journal of Alloys and Compounds, 2009. **469**(1): p. 164-168.
42. Karaca, H.E., et al., *Shape memory behavior of high strength Ni54Ti46 alloys.* Materials Science and Engineering: A, 2013. **580**(0): p. 66-70.
43. Haberland, C. and M.H. Elahinia, *Fabricating NiTi SMA Components.* Shape Memory Alloy Actuators: Design, Fabrication and Experimental Evaluation, 2015: p. 191.
44. Yang, Z., W. Tirry, and D. Schryvers, *Analytical TEM investigations on concentration gradients surrounding Ni 4 Ti 3 precipitates in Ni–Ti shape memory material.* Scripta materialia, 2005. **52**(11): p. 1129-1134.
45. Carroll, M., C. Somsen, and G. Eggeler, *Multiple-step martensitic transformations in Ni-rich NiTi shape memory alloys.* Scripta Materialia, 2004. **50**(2): p. 187-192.
46. Sehitoglu, H., et al., *Shape memory and pseudoelastic behavior of 51.5% Ni–Ti single crystals in solutionized and overaged state.* Acta Materialia, 2001. **49**(17): p. 3609-3620.
47. Sehitoglu, H., et al., *Detwinning in NiTi alloys.* Metallurgical and Materials Transactions A, 2003. **34**(1): p. 5-13.
48. Weinert, K. and V. Petzoldt, *Machining of NiTi based shape memory alloys.* Materials Science and Engineering: A, 2004. **378**(1): p. 180-184.
49. Chen, C., *A study on the machinability of a Ti49. 6Ni50. 4 shape memory alloy [J]*. Mater Lett, 1999. **40**: p. 27-32.
50. Wu, M.H. *Fabrication of nitinol materials and components*. in *Materials Science Forum*. 2002. Trans Tech Publ.
51. Andani, M.T., et al., *Metals for bone implants. Part 1. Powder metallurgy and implant rendering.* Acta biomaterialia, 2014. **10**(10): p. 4058-4070.
52. Frenzel, J., et al., *High quality vacuum induction melting of small quantities of NiTi shape memory alloys in graphite crucibles.* Journal of Alloys and Compounds, 2004. **385**(1): p. 214-223.
53. Mohsen Taheri Andani, C.H., Jason M. Walkera, Ali Sadi Turabi , Soheil Saedi,, R.R. Mohammadreza Karamooz, Haluk Karaca , David Dean, Mahmoud

Kadkhodaei,, and a.M. Elahinia, *Achieving biocompatible stiffness in NiTi through additive manufacturing.* Journal of Intelligent Material Systems and Structures, 2015.
54. Aydogmus, T. and A. Bor, *Production and characterization of porous TiNi shape memory alloys.* Turkish Journal of Engineering and Environmental Sciences, 2011. **35**(2): p. 69-82.
55. German, R.M., *Powder metallurgy and particulate materials processing: the processes, materials, products, properties, and applications*. 2005: Metal powder industries federation Princeton, NJ.
56. Haberland, C., *Additive Verarbeitung von NiTi-Formgedächtniswerkstoffen mittels Selective-Laser-Melting*. 2012: Shaker.
57. Likibi, F., et al., *Osseointegration study of porous nitinol versus titanium orthopaedic implants.* European Journal of Orthopaedic Surgery & Traumatology, 2004. **14**(4): p. 209-213.
58. Thompson, S.M., et al., *An overview of Direct Laser Deposition for additive manufacturing; Part I: Transport phenomena, modeling and diagnostics.* Additive Manufacturing, 2015. **8**: p. 36-62.
59. Gibson, I., D. Rosen, and B. Stucker, *Additive manufacturing technologies: 3D printing, rapid prototyping, and direct digital manufacturing*. 2014: Springer.
60. Haberland, C., et al. *Visions, concepts and strategies for smart Nitinol actuators and complex Nitinol structures produced by Additive Manufacturing*. in *ASME 2013 Conference on Smart Materials, Adaptive Structures and Intelligent Systems*. 2013. American Society of Mechanical Engineers.
61. Haberland, C., *Additive Verarbeitung von NiTi- Formgedächtniswerkstoffen mittels Selective Laser Melting*. 2012, Ruhr University Bochum: Aachen, Germany.
62. Bram, M., et al., *Reproducibility study of NiTi parts made by metal injection molding.* Journal of materials engineering and performance, 2012. **21**(12): p. 2701-2712.
63. Mentz, J., et al., *Powder metallurgical processing of NiTi shape memory alloys with elevated transformation temperatures.* Materials Science and Engineering: A, 2008. **491**(1): p. 270-278.
64. Shishkovsky, I., E.Y. Tarasova, and A. Petrov, *The synthesis of a biocomposite based on nickel titanium and hydroxyapatite under selective laser sintering conditions.* Technical Physics Letters, 2001. **27**(3): p. 211-213.
65. Arutyunov, Y.I., et al., *Structure and properties of the Ni-Ti intermetallic phases synthesized upon selective laser sintering: II. Structure and corrosion behavior.* Physics of metals and metallography, 2002. **93**(2): p. 185-188.
66. Pokoev, A. and I. Shishkovskii, *Structure and Properties of Ni—Ti Intermetallic Phases Synthesized upon Selective Laser Sintering: I. X~ Ray Diffraction Analysis.* Physics of metals and metallography, 2002. **93**(2).
67. Shishkovsky, I., *Shape memory effect in porous volume NiTi articles fabricated by selective laser sintering.* Technical physics letters, 2005. **31**(3): p. 186-188.
68. Shishkovsky, I., et al., *Porous biocompatible implants and tissue scaffolds synthesized by selective laser sintering from Ti and NiTi.* Journal of Materials Chemistry, 2008. **18**(12): p. 1309-1317.

69. Clare, A.T., et al., *Selective laser melting of high aspect ratio 3D nickel–titanium structures two way trained for MEMS applications.* International Journal of Mechanics and Materials in Design, 2008. **4**(2): p. 181-187.
70. Meier, H., et al., *Selective Laser Melting of NiTi shape memory components.* Innovative developments in design and manufacturing: advanced research in virtual and rapid prototyping, 2009: p. 233-238.
71. Meier, H. and C. Haberland, *Experimental studies on selective laser melting of metallic parts.* Materialwissenschaft und Werkstofftechnik, 2008. **39**(9): p. 665-670.
72. Meier, H., C. Haberland, and J. Frenzel, *Structural and functional properties of NiTi shape memory alloys produced by selective laser melting.* Innovative developments in design and manufacturing: advanced research in virtual and rapid prototyping, 2011: p. 291-296.
73. Haberland, C., H. Meier, and J. Frenzel. *On the Properties of Ni-Rich NiTi Shape Memory Parts Produced by Selective Laser Melting*. in *ASME 2012 Conference on Smart Materials, Adaptive Structures and Intelligent Systems*. 2012. American Society of Mechanical Engineers.
74. Haberland, C., et al. *Additive manufacturing of shape memory devices and pseudoelastic components*. in *Proceedings of SMASIS 2013-Conference on Smart Materials, Adaptive Structures and Intelligent Systems*. 2013.
75. Haberland, C., et al., *On the development of high quality NiTi shape memory and pseudoelastic parts by additive manufacturing.* Smart Materials and Structures, 2014. **23**(10): p. 104002.
76. Dadbakhsh, S., et al., *Effect of SLM Parameters on Transformation Temperatures of Shape Memory Nickel Titanium Parts.* Advanced Engineering Materials, 2014. **16**(9): p. 1140-1146.
77. Dadbakhsh, S., et al., *Influence of SLM on shape memory and compression behaviour of NiTi scaffolds.* CIRP Annals-Manufacturing Technology, 2015. **64**(1): p. 209–212.
78. Bormann, T., et al., *Microstructure of selective laser melted nickel–titanium.* Materials Characterization, 2014. **94**: p. 189-202.
79. Bormann, T., et al., *Tailoring selective laser melting process parameters for NiTi implants.* Journal of Materials Engineering and Performance, 2012. **21**(12): p. 2519-2524.
80. Bormann, T., et al. *Assessing the morphology of selective laser melted NiTi-scaffolds for a three-dimensional quantification of the one-way shape memory effect*. 2013.
81. Speirs, M., et al. *The effect of SLM parameters on geometrical characteristics of open porous NiTi scaffolds*. in *High Value Manufacturing: Advanced Research in Virtual and Rapid Prototyping: Proceedings of the 6th International Conference on Advanced Research in Virtual and Rapid Prototyping, Leiria, Portugal, 1-5 October, 2013*. 2013. CRC Press.
82. de Wild, M., et al., *Damping of Selective-Laser-Melted NiTi for Medical Implants.* Journal of Materials Engineering and Performance, 2014. **23**(7): p. 2614-2619.

83. Habijan, T., et al., *The biocompatibility of dense and porous Nickel–Titanium produced by selective laser melting.* Materials Science and Engineering: C, 2013. **33**(1): p. 419-426.
84. Miyazaki, S., et al., *Characteristics of deformation and transformation pseudoelasticity in Ti-Ni alloys.* Le Journal de Physique Colloques, 1982. **43**(C4): p. C4-255-C4-260.
85. Karaca, H., et al., *Effects of nanoprecipitation on the shape memory and material properties of an Ni-rich NiTiHf high temperature shape memory alloy.* Acta Materialia, 2013. **61**(19): p. 7422-7431.
86. Meng, X., et al., *Effect of aging on martensitic transformation and microstructure in Ni-rich TiNiHf shape memory alloy.* Scripta materialia, 2006. **54**(9): p. 1599-1604.
87. Elahinia, M., et al., *Manufacturing and processing of NiTi implants: A review.* Progress in Materials Science, 2012. **57**(5): p. 911-946.
88. Liu, Z., et al., *Crystal structure analysis of M2 high speed steel parts produced by selective laser melting.* Materials Characterization, 2013. **84**: p. 72-80.
89. Yap, C., et al., *Review of selective laser melting: Materials and applications.* Applied Physics Reviews, 2015. **2**(4): p. 041101.
90. Zhou, X., et al., *Textures formed in a CoCrMo alloy by selective laser melting.* Journal of Alloys and Compounds, 2015. **631**: p. 153-164.
91. Song, B., et al., *Microstructure and tensile properties of iron parts fabricated by selective laser melting.* Optics & Laser Technology, 2014. **56**: p. 451-460.
92. Kruth, J.P., et al., *Selective laser melting of iron-based powder.* Journal of Materials Processing Technology, 2004. **149**(1–3): p. 616-622.
93. Li, Y. and D. Gu, *Parametric analysis of thermal behavior during selective laser melting additive manufacturing of aluminum alloy powder.* Materials & Design, 2014. **63**: p. 856-867.
94. Carter, L.N., et al., *The influence of the laser scan strategy on grain structure and cracking behaviour in SLM powder-bed fabricated nickel superalloy.* Journal of Alloys and Compounds, 2014. **615**: p. 338-347.
95. Thijs, L., et al., *A study of the microstructural evolution during selective laser melting of Ti–6Al–4V.* Acta Materialia, 2010. **58**(9): p. 3303-3312.
96. Read, N., et al., *Selective laser melting of AlSi10Mg alloy: Process optimisation and mechanical properties development.* Materials & Design, 2015. **65**: p. 417-424.
97. Kempen, K., et al., *Processing AlSi10Mg by selective laser melting: parameter optimisation and material characterisation.* Materials Science and Technology, 2014.
98. Li, R., et al., *316L stainless steel with gradient porosity fabricated by selective laser melting.* Journal of Materials Engineering and Performance, 2010. **19**(5): p. 666-671.
99. Yadroitsev, I., P. Bertrand, and I. Smurov, *Parametric analysis of the selective laser melting process.* Applied Surface Science, 2007. **253**(19): p. 8064-8069.
100. Takaichi, A., et al., *Microstructures and mechanical properties of Co–29Cr–6Mo alloy fabricated by selective laser melting process for dental applications.* Journal of the Mechanical Behavior of Biomedical Materials, 2013. **21**: p. 67-76.

101. Vandenbroucke, B. and J.-P. Kruth, *Selective laser melting of biocompatible metals for rapid manufacturing of medical parts.* Rapid Prototyping Journal, 2007. **13**(4): p. 196-203.
102. Saedi, S., et al., *Thermomechanical characterization of Ni-rich NiTi fabricated by selective laser melting.* Smart Materials and Structures, 2016. **25**(3): p. 035005.
103. Kruth, J.-P., et al., *Additive manufacturing of metals via Selective Laser Melting: Process aspects and material developments.* 2015.
104. Song, B., et al., *Differences in microstructure and properties between selective laser melting and traditional manufacturing for fabrication of metal parts: A review.* Frontiers of Mechanical Engineering, 2015. **10**(2): p. 111-125.
105. Kou, S., *Welding Metallurgy, Seconded*. 2003, John Wiley & Sons, Inc., Hoboken, New Jersey.
106. Kruth, J.-P., et al., *Consolidation phenomena in laser and powder-bed based layered manufacturing.* CIRP Annals-Manufacturing Technology, 2007. **56**(2): p. 730-759.
107. Shifeng, W., et al., *Effect of molten pool boundaries on the mechanical properties of selective laser melting parts.* Journal of Materials Processing Technology, 2014. **214**(11): p. 2660-2667.
108. Guan, K., et al., *Effects of processing parameters on tensile properties of selective laser melted 304 stainless steel.* Materials & Design, 2013. **50**: p. 581-586.
109. Chlebus, E., et al., *Microstructure and mechanical behaviour of Ti—6Al—7Nb alloy produced by selective laser melting.* Materials Characterization, 2011. **62**(5): p. 488-495.
110. Rafi, H., et al., *Microstructures and mechanical properties of Ti6Al4V parts fabricated by selective laser melting and electron beam melting.* Journal of materials engineering and performance, 2013. **22**(12): p. 3872-3883.
111. Vrancken, B., et al., *Microstructure and mechanical properties of a novel β titanium metallic composite by selective laser melting.* Acta Materialia, 2014. **68**: p. 150-158.
112. Simonelli, M., Y.Y. Tse, and C. Tuck, *The formation of α + β microstructure in as-fabricated selective laser melting of Ti–6Al–4V.* Journal of Materials Research, 2014. **29**(17): p. 2028-2035.
113. Song, B., et al., *Fabrication of NiCr alloy parts by selective laser melting: columnar microstructure and anisotropic mechanical behavior.* Materials & Design, 2014. **53**: p. 1-7.
114. Thijs, L., et al., *Fine-structured aluminium products with controllable texture by selective laser melting of pre-alloyed AlSi10Mg powder.* Acta Materialia, 2013. **61**(5): p. 1809-1819.
115. Das, S., *Physical aspects of process control in selective laser sintering of metals.* Advanced Engineering Materials, 2003. **5**(10): p. 701-711.
116. Thijs, L., et al., *Strong morphological and crystallographic texture and resulting yield strength anisotropy in selective laser melted tantalum.* Acta Materialia, 2013. **61**(12): p. 4657-4668.
117. Ng, C.C., et al., *Microstructure and mechanical properties of selective laser melted magnesium.* Applied Surface Science, 2011. **257**(17): p. 7447-7454.

118. Petch, N., *The cleavage strength of polycrystals.* J. Iron Steel Inst., 1953. **174**: p. 25-28.
119. Orgéas, L. and D. Favier, *Stress-induced martensitic transformation of a NiTi alloy in isothermal shear, tension and compression.* Acta Materialia, 1998. **46**(15): p. 5579-5591.
120. Saburi, T., *Ti-Ni shape memory alloys.* Shape memory materials, 1999: p. 49-96.
121. Eggeler, G., et al., *On the effect of aging on martensitic transformations in Ni-rich NiTi shape memory alloys.* Smart materials and structures, 2005. **14**(5): p. S186.
122. Ren, X., et al., *A comparative study of elastic constants of Ti–Ni-based alloys prior to martensitic transformation.* Materials Science and Engineering: A, 2001. **312**(1): p. 196-206.
123. Allafi, J.K., X. Ren, and G. Eggeler, *The mechanism of multistage martensitic transformations in aged Ni-rich NiTi shape memory alloys.* Acta Materialia, 2002. **50**(4): p. 793-803.
124. Bataillard, L., J.-E. Bidaux, and R. Gotthardt, *Interaction between microstructure and multiple-step transformation in binary NiTi alloys using in-situ transmission electron microscopy observations.* Philosophical magazine A, 1998. **78**(2): p. 327-344.
125. Khalil-Allafi, J., A. Dlouhy, and G. Eggeler, *Ni4Ti3-precipitation during aging of NiTi shape memory alloys and its influence on martensitic phase transformations.* Acta Materialia, 2002. **50**(17): p. 4255-4274.
126. Otsuka, K. and X. Ren, *Recent developments in the research of shape memory alloys.* Intermetallics, 1999. **7**(5): p. 511-528.
127. Liu, Y., et al., *Some aspects of the properties of NiTi shape memory alloy.* Journal of Alloys and Compounds, 1997. **247**(1): p. 115-121.
128. Khalil-Allafi, J., et al., *On the influence of heterogeneous precipitation on martensitic transformations in a Ni-rich NiTi shape memory alloy.* Materials Science and Engineering: A, 2004. **378**(1): p. 148-151.
129. Gall, K., et al., *Instrumented micro-indentation of NiTi shape-memory alloys.* Acta Materialia, 2001. **49**(16): p. 3205-3217.
130. Saedi, S., et al., *The influence of heat treatment on the thermomechanical response of Ni-rich NiTi alloys manufactured by selective laser melting.* Journal of Alloys and Compounds, 2016. **677**: p. 204-210.
131. Wang, X., Y. Bellouard, and J.J. Vlassak, *Laser annealing of amorphous NiTi shape memory alloy thin films to locally induce shape memory properties.* Acta Materialia, 2005. **53**(18): p. 4955-4961.
132. Dadbakhsh, S., et al., *Texture and anisotropy in selective laser melting of NiTi alloy.* Materials Science and Engineering: A, 2016. **650**: p. 225-232.
133. Yadroitsev, I., et al., *Energy input effect on morphology and microstructure of selective laser melting single track from metallic powder.* Journal of Materials Processing Technology, 2013. **213**(4): p. 606-613.
134. Niendorf, T., et al., *Highly Anisotropic Steel Processed by Selective Laser Melting.* Metallurgical and Materials Transactions B, 2013. **44**(4): p. 794-796.
135. Simonelli, M., Y.Y. Tse, and C. Tuck, *On the texture formation of selective laser melted Ti-6Al-4V.* Metallurgical and Materials Transactions A, 2014. **45**(6): p. 2863-2872.

136. Khalil-Allafi, J., A. Dlouhy, and G. Eggeler, *Ni 4 Ti 3-precipitation during aging of NiTi shape memory alloys and its influence on martensitic phase transformations.* Acta Materialia, 2002. **50**(17): p. 4255-4274.
137. Filip, P. and K. Mazanec, *On precipitation kinetics in TiNi shape memory alloys.* Scripta Materialia, 2001. **45**(6): p. 701-707.
138. Zheng, Y., et al., *Effect of ageing treatment on the transformation behaviour of Ti–50.9 at.% Ni alloy.* Acta Materialia, 2008. **56**(4): p. 736-745.
139. Tang, W., et al., *New modelling of the B2 phase and its associated martensitic transformation in the Ti–Ni system.* Acta Materialia, 1999. **47**(12): p. 3457-3468.
140. Karaca, H., et al., *Shape memory behavior of high strength NiTiHfPd polycrystalline alloys.* Acta Materialia, 2013. **61**(13): p. 5036-5049.
141. Karaca, H., et al., *NiTiHf-based shape memory alloys.* Materials Science and Technology, 2014. **30**(13a): p. 1530-1544.
142. Karaca, H., et al., *Effects of aging on [111] oriented NiTiHfPd single crystals under compression.* Scripta Materialia, 2012. **67**(7): p. 728-731.
143. Huang, X. and Y. Liu, *Effect of annealing on the transformation behavior and superelasticity of NiTi shape memory alloy.* Scripta Materialia, 2001. **45**(2): p. 153-160.
144. Zhou, Y., et al., *Origin of 2-stage R-phase transformation in low-temperature aged Ni-rich Ti–Ni alloys.* Acta materialia, 2005. **53**(20): p. 5365-5377.
145. Kaya, I., et al., *Shape Memory Behavior of [111]-Oriented NiTi Single Crystals After Stress-Assisted Aging.* Acta Metallurgica Sinica (English letters), 2016. **29**(3): p. 282-286.
146. Chumlyakov, Y.I., et al. *Dependence of shape memory effect and superelasticity on the number of variants of dispersed particles in titanium-nickel single crystals*. in *Doklady Physics*. 2002. Springer.
147. Nishida, M., C. Wayman, and A. Chiba, *Electron microscopy studies of the martensitic transformation in an aged Ti-51at% Ni shape memory alloy.* Metallography, 1988. **21**(3): p. 275-291.
148. Callister, W.D., *Plastic Deformation of Polycrystalline Metals* in *Fundamentals of materials science and engineering: an interactive e-text*, W. Anderson, Editor. 2001, Wiley: Hoboken, NJ. p. 204-206.
149. Kasperovich, G. and J. Hausmann, *Improvement of fatigue resistance and ductility of TiAl6V4 processed by selective laser melting.* Journal of Materials Processing Technology, 2015. **220**: p. 202-214.
150. Gall, K., et al., *Tension–compression asymmetry of the stress–strain response in aged single crystal and polycrystalline NiTi.* Acta Materialia, 1999. **47**(4): p. 1203-1217.
151. Banhart, J., *Properties and applications of cast aluminum sponges.* Advanced Engineering Materials, 2000. **2**(4): p. 188-191.
152. Soboyejo, W.O. and T. Srivatsan, *Advanced structural materials: properties, design optimization, and applications*. 2006: CRC Press.
153. Ryan, G., A. Pandit, and D.P. Apatsidis, *Fabrication methods of porous metals for use in orthopaedic applications.* Biomaterials, 2006. **27**(13): p. 2651-2670.
154. Walker, J., M. Elahinia, and C. Haberland. *An investigation of process parameters on selective laser melting of nitinol*. in *ASME 2013 Conference on Smart*

Materials, Adaptive Structures and Intelligent Systems. 2013. American Society of Mechanical Engineers.
155. Castleman, L., et al., *Biocompatibility of nitinol alloy as an implant material.* Journal of Biomedical Materials Research, 1976. **10**(5): p. 695-731.
156. Berger-Gorbet, M., et al., *Biocompatibility testing of NiTi screws using immunohistochemistry on sections containing metallic implants.* Journal of biomedical materials research, 1996. **32**(2): p. 243-248.
157. Simske, S. and R. Sachdeva, *Cranial bone apposition and ingrowth in a porous nickel–titanium implant.* Journal of biomedical materials research, 1995. **29**(4): p. 527-533.
158. Assad, M., et al. *[Assays of cytotoxicity of the Nickel-Titanium shape memory alloy]*. in *Annales de chirurgie*. 1993.
159. Ryhänen, J., et al., *Bone healing and mineralization, implant corrosion, and trace metals after nickel–titanium shape memory metal intramedullary fixation.* Journal of biomedical materials research, 1999. **47**(4): p. 472-480.
160. Ryhänen, J., et al., *Bone modeling and cell–material interface responses induced by nickel–titanium shape memory alloy after periosteal implantation.* Biomaterials, 1999. **20**(14): p. 1309-1317.
161. Elahinia, M., et al., *Fabrication of NiTi through additive manufacturing: a review.* Progress in Materials Science, 2016. **83**: p. 630-663.
162. Moghaddam, N.S., et al., *Metals for bone implants: safety, design, and efficacy.* Biomanufacturing Reviews, 2016. **1**(1): p. 1.
163. Kang, S.-B., et al., *In vivo result of porous TiNi shape memory alloy: bone response and growth.* Materials Transactions, 2002. **43**(5): p. 1045-1048.
164. Bansiddhi, A., et al., *Porous NiTi for bone implants: a review.* Acta biomaterialia, 2008. **4**(4): p. 773-782.
165. Moghaddam, N.S., et al., *Metallic Fixation of Mandibular Segmental Defects: Graft Immobilization and Orofacial Functional Maintenance.* Plastic and Reconstructive Surgery Global Open, 2016. **4**(9).
166. Moghaddam, N.S., et al., *Three dimensional printing of stiffness-tuned, nitinol skeletal fixation hardware with an example of mandibular segmental defect repair.* Procedia CIRP, 2016. **49**: p. 45-50.
167. Moghaddam, N.S., et al. *Enhancement of Bone Implants by Substituting Nitinol for Titanium (Ti-6Al-4V): A Modeling Comparison*. in *ASME 2014 Conference on Smart Materials, Adaptive Structures and Intelligent Systems*. 2014. American Society of Mechanical Engineers.
168. Greiner, C., S.M. Oppenheimer, and D.C. Dunand, *High strength, low stiffness, porous NiTi with superelastic properties.* Acta Biomaterialia, 2005. **1**(6): p. 705-716.
169. Simske, S., R. Ayers, and T. Bateman. *Porous materials for bone engineering*. in *Materials Science Forum*. 1997. Trans Tech Publ.
170. Gibson, L.J. and M.F. Ashby, *Cellular solids: structure and properties*. 1997: Cambridge university press.
171. Robertson, D.M., L. St Pierre, and R. Chahal, *Preliminary observations of bone ingrowth into porous materials.* Journal of biomedical materials research, 1976. **10**(3): p. 335-344.

172. Cameron, H., I. Macnab, and R. Pilliar, *A porous metal system for joint replacement surgery.* The International journal of artificial organs, 1978. **1**(2): p. 104-109.
173. Head, W.C., D.J. Bauk, and R.H. Emerson Jr, *Titanium as the material of choice for cementless femoral components in total hip arthroplasty.* Clinical orthopaedics and related research, 1995. **311**: p. 85-90.
174. BOBYN, J.D., et al., *Producing and Avoiding Stress Shielding: Laboratory and Clinical Observations of Noncemented Total Hip Arthroplasty.* Clinical orthopaedics and related research, 1992. **274**: p. 79-96.
175. Raad, B., N.S. Moghaddam, and M. Elahinia. *A numerical simulation of the effect of using porous superelastic Nitinol and stiff Titanium fixation hardware on the bone remodeling*. in *SPIE Smart Structures and Materials+ Nondestructive Evaluation and Health Monitoring*. 2016. International Society for Optics and Photonics.
176. Raad, B., N.S. Moghaddam, and M. Elahinia. *A comparison between porous NiTi and Ti-6Al-4V fixation hardware on bone remodeling after a reconstruction surgery*. in *ASME 2016 11th international manufacturing science and engineering conference*. 2016. American Society of Mechanical Engineers.
177. Shayesteh Moghaddam, N., *Toward Patient Specific Long Lasting Metallic Implants for Mandibular Segmental Defects*. 2015, University of Toledo.
178. Nouri, A., P.D. Hodgson, and C.e. Wen, *Biomimetic porous titanium scaffolds for orthopaedic and dental applications*. 2010: InTech.
179. Krishna, B.V., S. Bose, and A. Bandyopadhyay, *Fabrication and characterization of porous Ti6Al4V parts for biomedical applications using electron beam melting process.* J Acta Biomater, 2007. **3**: p. 997-1006.
180. Köhl, M.B., M. ; Buchkremer, H. P. ; Stöver, D. ; Habijan, T. ; Köller, M. . *Powder metallurgical production, mechanical and biomedical properties of porous NiTi shape memory alloys*. in *Materials and Processes for Medical Devices Conference*. 2007. Palm Desert, CA.
181. Graham, J., M. Ries, and L. Pruitt, *Effect of bone porosity on the mechanical integrity of the bone-cement interface.* J Bone Joint Surg Am, 2003. **85**(10): p. 1901-1908.
182. Imwinkelried, T., *Mechanical properties of open-pore titanium foam.* Journal of biomedical materials research Part A, 2007. **81**(4): p. 964-970.
183. Urban, R.M., et al., *The Bone-Implant Interface of Femoral Stems with Non-Circumferential Porous Coating. A Study of Specimens Retrieved at Autopsy*.* The Journal of Bone & Joint Surgery, 1996. **78**(7): p. 1068-81.
184. Kienapfel, H., et al., *Implant fixation by bone ingrowth.* The Journal of arthroplasty, 1999. **14**(3): p. 355-368.
185. Ravari, M.K., et al., *On the effects of geometry, defects, and material asymmetry on the mechanical response of shape memory alloy cellular lattice structures.* Smart Materials and Structures, 2016. **25**(2): p. 025008.
186. Ravari, M.K. and M. Kadkhodaei, *A computationally efficient modeling approach for predicting mechanical behavior of cellular lattice structures.* Journal of Materials Engineering and Performance, 2015. **24**(1): p. 245-252.

187. Ravari, M.K., et al., *Numerical investigation on mechanical properties of cellular lattice structures fabricated by fused deposition modeling.* International Journal of Mechanical Sciences, 2014. **88**: p. 154-161.
188. Wagner, M., J. Frenzel, and G. Eggeler. *Evolution of microstructural parameters during cycling of NiTi and their effect on mechanical and thermal memory*. in *SMST-2004: Proceedings of the International Conference on Shape Memory and Superelastic Technologies*. 2006. ASM International.
189. Rahmanian, R., et al. *Load bearing and stiffness tailored niti implants produced by additive manufacturing: a simulation study*. in *SPIE Smart Structures and Materials+ Nondestructive Evaluation and Health Monitoring*. 2014. International Society for Optics and Photonics.
190. Zhao, Y., et al., *Compression behavior of porous NiTi shape memory alloy.* Acta materialia, 2005. **53**(2): p. 337-343.
191. Zhang, L., et al., *Superelastic behaviors of biomedical porous NiTi alloy with high porosity and large pore size prepared by spark plasma sintering.* Journal of Alloys and Compounds, 2015. **644**: p. 513-522.
192. Nemat-Nasser, S., et al., *Experimental characterization and micromechanical modeling of superelastic response of a porous NiTi shape-memory alloy.* Journal of the Mechanics and Physics of Solids, 2005. **53**(10): p. 2320-2346.
193. Zhang, X., et al., *Superelasticity decay of porous NiTi shape memory alloys under cyclic strain-controlled fatigue conditions.* Materials Science and Engineering: A, 2008. **481**: p. 170-173.
194. Yuan, B., et al., *Control of porosity and superelasticity of porous NiTi shape memory alloys prepared by hot isostatic pressing.* Smart materials and structures, 2005. **14**(5): p. S201.
195. Bram, M., et al., *Mechanical properties of highly porous NiTi alloys.* Journal of materials engineering and performance, 2011. **20**(4-5): p. 522-528.
196. Hosseini, S., et al., *A comparative study on the mechanical behavior of porous titanium and NiTi produced by a space holder technique.* Journal of materials engineering and performance, 2014. **23**(3): p. 799-808.
197. Hench, L.L., *Bioceramics, a clinical success.* American Ceramic Society Bulletin, 1998. **77**(7): p. 67-74.
198. Auricchio, F. and R.L. Taylor, *Shape-memory alloys: modelling and numerical simulations of the finite-strain superelastic behavior.* Computer methods in applied mechanics and engineering, 1997. **143**(1-2): p. 175-194.

VITA

SOHEIL SAEDI

Professional Preparation

PhD, (Expected), Mechanical Engineering, University of Kentucky, School of Engineering, Lexington, KY, 2013-pres.

Master of Science, Mechatronic Engineering, Sharif University of Technology, International Campus, School of Engineering, Kish Island, Iran, 2007-2010

Bachelor of Science, Mechanical Engineering, University of Tabriz, School of Engineering, Tabriz, Iran, 2002-2007

Honors and Awards

Outstanding PhD student award of Department of Mechanical Engineering, University of Kentucky (2016)

Teaching/Research assistant scholarship award, Mechanical Engineering Department at University of Kentucky (2013-present)

Best research group of Mechanical Engineering Department of University of Kentucky award (2013)

Publications

Book Chapter

Ali S. Turabi., **Soheil Saedi**, Sayed M. Saghaian, Haluk E. Karaca and Mohammad Elahinia, "Experimental Characterization of Shape Memory Alloys", John Wiley and Sons, Inc., Hoboken, New Jersey, ISBN: 978-1-118-35944-0.

Journal Articles

Soheil Saedi, et al. "Thermomechanical characterization of Ni-rich NiTi fabricated by selective laser melting." Smart Materials and Structures, (2016).

Soheil Saedi, et al. "Texture, aging, and superelasticity of selective laser melting (SLM) fabricated Ni-rich NiTi alloys", Journal of Materials Science and Engineering:

A, (2017).

Soheil Saedi, et al. "The influence of heat treatment on the thermomechanical response of Ni-rich NiTi alloys manufactured by selective laser melting." Journal of alloys and compounds, (2016).

Soheil Saedi, et al. "Mechanical and shape memory properties of equiatomic porous NiTi manufactured by selective laser melting", Journal of mechanical behavior of biomedical materials, (2017)

Soheil Saedi, et al. "A local hybrid actuator for robotic surgery instruments." International Journal of Biomechatronics and Biomedical Robotics, (2014).

Soheil Saedi, et al. "Shape Memory Response of Porous NiTi Shape Memory Alloys Fabricated by Selective Laser Melting." Acta Materialia, (Submitted).

Soheil Saedi, et al. "Effect of Hatch Spacing in Selective Laser Melting on Microstructure and Mechanical response of NiTi." Scripta Materialia, (Submitted).